Fundamental Processes in Flavoprotein Photochemistry

Bo Zhuang

INSTITUT POLYTECHNIQUE DE PARIS

ÉCOLE POLYTECHNIQUE

IP PARIS

NNT : 2022IPPAX051

Thèse de doctorat

Fundamental Processes in Flavoprotein Photochemistry

Thèse de doctorat de l'Institut Polytechnique de Paris
préparée à École Polytechnique

École doctorale n°626
École Doctorale de l'Institut Polytechnique de Paris (ED IP Paris)
Spécialité de doctorat : Biologie

Thèse présentée et soutenue à Palaiseau, le 13 juillet 2022, par

BO ZHUANG

Composition du Jury :

Michel Sliwa Directeur de Recherche CNRS Université de Lille (LASIRE)	Président
Johanna Brazard Collaboratrice Scientifique II Université de Genève (Département de Chimie Physique)	Rapporteur
Antonio Monari Professeur des Universités Université Paris Cité (ITODYS)	Rapporteur
Pavel Müller Chargé de Recherche CNRS CEA Saclay (I2BC)	Examinateur
Marten Vos Directeur de Recherche CNRS École Polytechnique (LOB)	Directeur de thèse
Alexey Aleksandrov Chargé de Recherche CNRS École Polytechnique (LOB)	Co-Directeur de thèse

知是行之始，行是知之成。

——王守仁

Acknowledgements

“We are all in the gutter, but some of us are looking at the stars.”

Life sometimes can be challenging and full of misfortune. This is particularly true for Ph.D. students during the pandemic period. Without all those people on my side during this three-year journey, probably I would have still remained “in the gutter”, without even noticing there are stars up above in the sky.

First and foremost, I am deeply indebted to my supervisor, Marten Vos, for accepting me as a Ph.D. student, despite all the troubles in the administration process, and for his invaluable advice, continuous support, and patience during my Ph.D. study; his immense knowledge and plentiful experience have encouraged me in all the time of my scientific research and daily life. My sincere gratitude extends to Alexey Alexandrov, for co-supervising my thesis, whose guidance and instructions have significantly deepened my understanding of computer simulations on biological systems, and motivated me to further pursue this subject in my future career. I am very grateful to Ursula Liebl and Rivo Ramodiharilafy for their expert help in the preparations of protein samples and for many interesting discussions on molecular biology. Thanks should also go to the jury members of my thesis defense, Michel Sliwa, Johanna Brazard, Antonio Monari, and Pavel Müller, for spending their time reading my manuscript and for providing insightful feedback.

Our work on FNR would not have been possible without the collaboration with Daisuke Seo, who not only provided high-quality protein samples, but also introduced me to the intriguing research of FNR. I also had the pleasure of working with Pavel Müller and Poutoum-Palakiyém Samire on the FAP protein; this project, although did not end up in my thesis, still gave me precious experience. I would be remiss in not mentioning Aurélien de la Lande and Thomas Gustavsson, the committee members of my mini-defense, whose positive feedback have greatly encouraged me to continue my scientific adventure. Andras Lukacs, Mengyu Gao, Corinne Gosmini have also lent a helping hand in my experiments and deserve my sincere thanks as well.

I am truly grateful to have had the opportunity to work in LOB for three years and met a lot of amazing people here. I would like to thank François Hache, the head of the laboratory, for welcoming me as a member of LOB, and thank the secretaries Christelle Français and Laure Lachapelle, for the administration work. Thank you, Jean-Christophe Lambry, Hannu Myllykallio, Michel Négrerie, Kevin Laouer, Anastasia Croitoru, Seongbin Lim, Auriane Perrin, Anaïs Bayard and all the other members of the laboratory. Your presence has enriched my stay here and made these three years in France even more unique to me.

My biggest thanks to my family for their tremendous understanding and encouragement in the past few years. Thank you also to my friends in China and Japan, for their support from far away, especially during the lockdown periods. Lastly, I would like to acknowledge the China Scholarship Council for providing a Ph.D. scholarship that allowed me to conduct this thesis.

Abstract in English

Flavins are derivatives of vitamin B_2 that form a highly versatile group of chromophores found in a large variety of enzymes and photoreceptor proteins. They can adopt three different redox states with various protonation states, leading to at least five physiologically relevant forms, with distinct electronic absorption spectra. Despite the diverse photophysical properties of the flavin cofactors, there are only very few natural photo-responsive flavoproteins. The vast majority of flavoproteins perform non-light-driven physiological functions ("non-photoactive"), although ultrafast, reversible photoinduced redox reactions between flavins and surrounding residues still widely occur in these systems, which can be viewed as photo-protective "self-quenching".

The past few decades have seen a blooming in the study of flavoproteins for their photocatalytic and photo-biotechnological applications. Moreover, a newly emerging approach in the development of novel photocatalysts from canonical "non-photoactive" flavoenzymes is making use of the photochemistry of reduced flavins instead of the oxidized resting state. Furthermore, practical implications of photochemistry of yet different flavin species are envisaged, but a basic understanding of their mechanisms is still required. In this thesis, applying ultrafast absorption and fluorescence spectroscopy combined with molecular simulations and quantum chemistry approaches, a variety of fundamental photochemical processes in flavoproteins is investigated.

First the photoreduction of oxidized flavins was revisited in a flavoprotein, ferredoxin-$NADP^+$ oxidoreductase (FNR), with closely packed reactant configurations, allowing ultrafast formation of intermediate radical pairs. Combining experimental and modeling techniques allowed a detailed assessment of the influence of the environment on the spectral properties of both the anionic flavin and the cationic amino acid (tyrosine or tryptophan) radicals. We further investigated the photochemistry of protein-bound flavin species in different chemical states that are largely unexplored in the literature. It is demonstrated that photooxidation of anionic flavin radicals, which act as reaction intermediates in many biochemical reactions, efficiently occurs within ~100 fs in several flavoprotein oxidases. This process, effectively the reverse of

the well-known photoreduction of oxidized flavin may constitute a universal decay pathway. The excited-state properties of fully reduced flavins were studied in several FNR systems where they are involved as functional intermediates, and compared with those in solution. Valuable information concerning their electronic structures and the flavin flexibility was obtained and compared with atomic simulations, with important catalytic implications. Finally, an unprecedented photo-dissociation phenomenon was revealed for a non-covalent charge transfer complex of flavin and an inhibitor in the flavoenzyme monomeric sarcosine oxidase. This process occurs on the timescale of a few hundred femtoseconds and can be attributed to a well-defined photoinduced isomerization of the inhibitor.

Altogether, the described findings, which include the discovery of two hitherto undocumented photochemical processes in flavoproteins, expand the repertoire of photochemistry involving flavin cofactors. This work may open new avenues for the exploration of flavin photochemistry with ultimately possible practical implications as novel photocatalysts and optogenetic tools.

Abstract in French

Les flavines sont des dérivés de la vitamine B_2 (riboflavine) qui forment un groupe de chromophores très polyvalents présents dans une grande variété d'enzymes et de protéines photoréceptrices. Elles peuvent adopter trois états redox différents avec divers états de protonation, menant à au moins cinq formes physiologiquement pertinentes, avec des spectres d'absorption distincts dans les domaines proche ultraviolet et visible. Malgré les propriétés photophysiques diverses des cofacteurs flavine, il n'y a que très peu de flavoprotéines naturellement photoréactives. La grande majorité des flavoprotéines remplissent des fonctions physiologiques non générées par la lumière ("non-photoactives"), bien que des réactions d'oxydoréduction photo-induites ultra-rapides et réversibles entre les flavines et les résidus proches s'y produisent largement, ce qui peut être considéré comme "auto-quenching" photo-protectrice.

Ces dernières décennies, l'étude des flavoprotéines a connu un essor pour leurs applications photocatalytiques et photo-biotechnologiques. De plus, une approche émergeante dans le développement de nouveaux photocatalyseurs à partir de flavoenzymes canoniques "non-photoactives" utilise la photochimie de flavines réduites au lieu de l'état de repos oxydé. En outre, des implications pratiques de la photochimie d'espèces de flavine encore différentes sont envisagées, mais une compréhension fondamentale de leurs mécanismes est encore requise. Dans cette thèse, par l'application de spectroscopie d'absorption et de fluorescence ultrarapide combinée avec des simulations moléculaires et d'approches de chimie quantique, une variété de processus photochimiques fondamentaux dans les flavoprotéines est étudiée.

Tout d'abord, la photoréduction des flavines oxydées a été revisitée dans une flavoprotéine, la ferrédoxine-$NADP^+$ oxydoréductase (FNR), ayant des configurations des réactifs très compactes, permettant la formation ultrarapide (200–300 femtosecondes) de paires de radicaux intermédiaires avec des durées de vie de quelques picosecondes. La combinaison de techniques expérimentales et de modélisation a permis une évaluation détaillée de l'influence de l'environnement sur les propriétés spectrales, et sur leur évolution temporelle, des radicaux anioniques de flavine et cationiques d'acide aminé (tyrosine ou tryptophane).

Par ailleurs, motivés par des photocatalysateurs développés récemment par bio-ingénierie, nous avons étudié la photochimie de flavines liées aux protéines dans différents états chimiques largement inexplorés dans la littérature. Il est démontré par spectroscopie d'absorption transitoire que la photooxydation des radicaux anioniques de flavine, qui agissent comme des intermédiaires de réaction dans de nombreuses réactions biochimiques, se produit efficacement en ~100 fs dans plusieurs flavoprotéines oxydases, y compris dans la flavoprotéine modèle glucose oxydase. La recombinaison de charges s'effectue ensuite dans une fourchette remarquablement étroite de 10–20 ps dans l'ensemble des cinq flavoprotéines oxydases étudiés. Des résidus cationiques d'histidine et d'arginine du site actif sont proposés comme candidats accepteurs d'électrons, sur la base de calculs de dynamique moléculaire et de mécanique quantique. Ce processus, qui est effectivement l'inverse de la photoréduction bien connue de la flavine oxydée, pourrait constituer une voie de désactivation universelle.

Les propriétés de l'état excité des flavines complétement réduites ont été étudiées dans plusieurs systèmes FNR où elles sont impliquées comme intermédiaires fonctionnels, et comparées à celles dans différents états de protonation en solution. Des informations précieuses concernant leurs structures électroniques et la flexibilité des flavines ont été obtenues et comparées avec des simulations atomiques, avec des implications catalytiques importantes.

Enfin, un phénomène de photo-dissociation sans précédent a été révélé pour un complexe de transfert de charge non covalent de la flavine et du inhibiteur methyle-thioacetate dans la flavoenzyme sarcosine oxydase monomérique. Ce processus se produit sur une échelle de temps de ~300 femtosecondes, avec un rendement quantique élevé et sans barrière d'activation. Il peut être attribué à une isomérisation photoinduite bien définie de l'inhibiteur, éliminant tout interaction de type transfert de charge. Le complexe initial se reforme ensuite de manière géminée en quelques nanosecondes à température ambiante avec une énergie d'activation de 28 kJ/mol; à des températures cryogéniques, la photo-transformation est quasi-permanente.

Dans l'ensemble, les résultats décrits, qui incluent la découverte de deux processus photochimiques jusqu'alors non documentés dans les flavoprotéines, élargissent le répertoire de la photochimie impliquant des cofacteurs de flavine. Ce travail peut ouvrir de nouvelles voies pour l'exploration de la photochimie des flavines avec, à terme, des implications pratiques possibles comme nouveaux photocatalyseurs et outils optogénétiques.

Table of Contents

Chapter 1. General Introduction

Colored biomolecules are ubiquitous in natural systems. Some of them, such as chlorophyll and retinal, are exclusively employed in photobiological processes. Others, such as hemes and metal centers contained in many proteins, can perform photochemistry, although not for known photobiological functions, and their spectroscopic properties can be used to follow biochemical reactions. Flavins are arguably one of the most versatile cofactors that are found in a large variety of enzymes and photoreceptors (called flavoproteins). In most of these systems they do not perform photobiological functions, but in some cases they do. The versatility of these systems makes them interesting as starting points for novel photocatalysts and optogenetic tools. Apart from the fundamental interest, ultimately enabling rational design in flavoprotein engineering is therefore one of the motivations to investigate the mechanisms underlying known flavin photochemical processes happening in flavoproteins and to explore new ones. In this larger context, this thesis describes efforts to understand a variety of fundamental photochemical reactions in flavoproteins.

Scheme 1.1 Chemical structure of biologically important flavins.

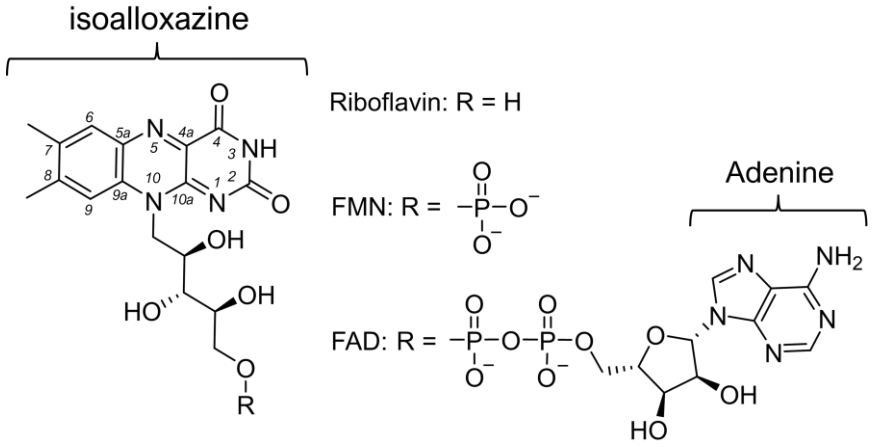

Flavins (Scheme 1.1) are derivatives of vitamin B_2 (riboflavin) and are accommodated in proteins essentially in the form of flavin adenine dinucleotide (FAD) or flavin mononucleotide (FMN). The isoalloxazine ring system is at the heart of the reactivity of flavins and of their spectroscopic properties. Flavins can adopt three different redox forms with various

protonation states, leading to at least five physiologically relevant states (Scheme 1.2).[1,2] Interacting with a manifold of substrates, as well as with other proteins, these properties allow flavoproteins to partake in a large variety of biochemical electron (one- and two-electron) and proton transfer reactions, including those that couple one- and two-electron reactions and bifurcation reactions.[3,4] Flavins in different the redox states exhibit distinct absorption spectra (Figure 1.1) and therefore different colors.[5,6] The changes of flavin absorptions are widely used to monitor its redox states during biochemical reactions, for instance in rapid mixing experiments with external reactants.

Scheme 1.2 Five redox and protonation states of flavins involved in the functional processes of flavoproteins. Flavin is represented by the isoalloxazine moiety.

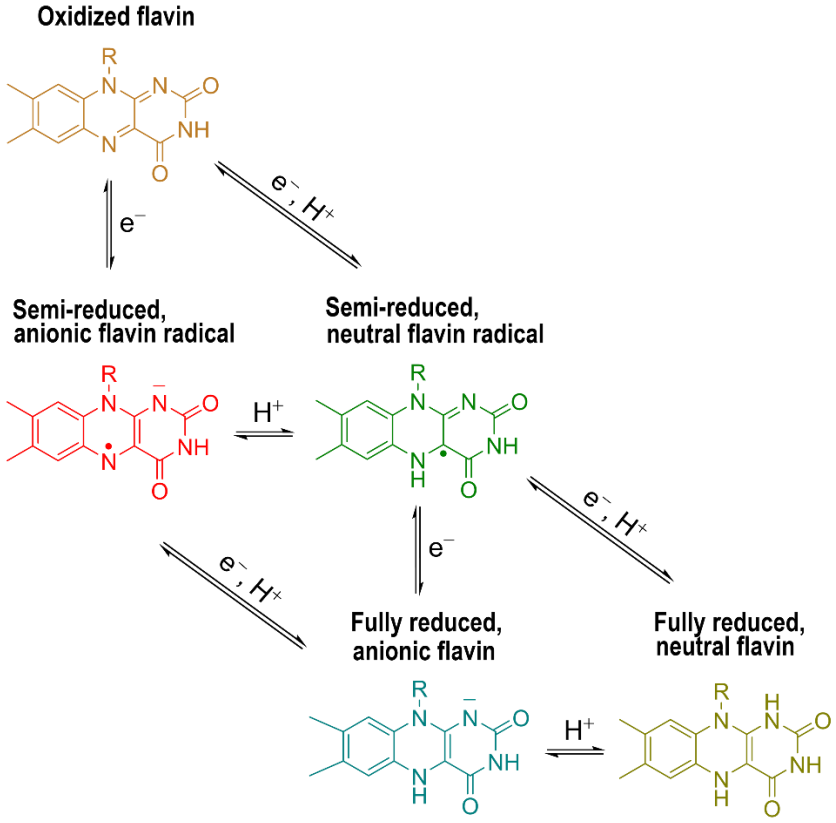

Formation of flavin excited state by photon absorption can lead to fluorescence, and indeed fluorescence has been reported for most redox states, with the possible exception of anionic flavin radicals.[7] Oxidized flavin, the resting state of the flavin cofactor in most flavoproteins, is strongly fluorescent in solution, but when bound to proteins its fluorescence is often quenched as it may act as electron acceptor and participate in photoinduced electron transfer (ET) reactions.[8–13] For a fraction of oxidized FAD (FAD_{ox}) in solution, such quenching also occurs, ascribed to the adenine moiety being in a stacking interaction with the isoalloxazine ring system.[14,15] Fully reduced (neutral, or anionic) flavins emit virtually no

fluorescence in solution, but in a confined protein environment, or at low temperature, their fluorescence is greatly enhanced, a phenomenon ascribed to hindering of deactivation by bending motions of the isoalloxazine ring.[6,14,16–18] Semi-reduced (neutral, or anionic) flavin radicals are usually short-lived species formed in the catalytic cycles of flavoproteins, and in solution cannot be obtained as free radicals in the steady state. In some flavoproteins where neutral flavin radicals can be stabilized, excitation has been reported to extract an electron from nearby aromatic residues, leading to the formation of fully reduced flavins.[16,19–22] On the other hand, how anionic flavin radicals behave upon excitation has remained essentially unknown thus far, although there are a few studies reporting their fluorescence[16,23,24] that may have been complicated by the presence of other fluorescent species.[7]

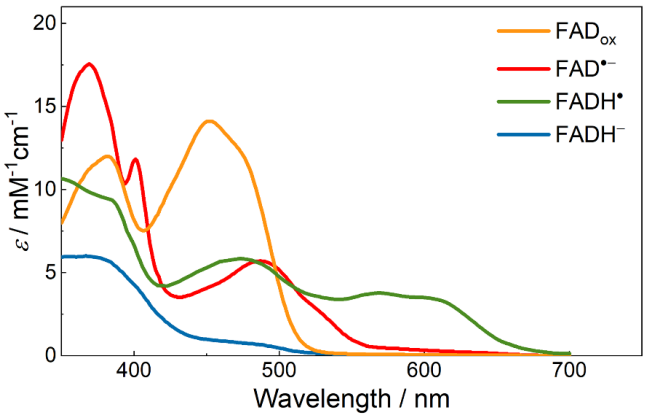

Figure 1.1 Steady-state absorption spectra of flavins in different redox and protonation states in GOX. The spectrum of FADH• is reproduced from ref. 5. The color coding corresponds to that in Scheme 1.2.

Despite the diverse photophysical properties of the flavin cofactors, the vast majority of flavoproteins perform non-light-driven physiological catalytic and/or charge transport functions ("non-photoactive"). The few exceptions include the flavin-dependent photoenzymes, DNA photolyase and fatty acid photodecarboxylase (FAP), as well as the blue-light photoreceptors cryptochrome (CRY), BLUF (blue light sensing using flavin) domains and LOV (light-oxygen-voltage) domains. The past few decades have seen a blooming in the study and engineering of these light-responsive flavoproteins for their photocatalytic and biotechnological applications. For instance, variants of BLUF and LOV domains have been developed as new contributors to the optogenetic toolkit, as they have a compact size and can respond to near-UV/blue-light (300–500 nm).[25–27] Since its discovery in 2017, FAP, which is found in microalgae and able to produce hydrocarbons from fatty acids using solar energy, has attracted worldwide attention for its potential application in biofuel production and green chemistry.[28–30]

Scheme 1.3 Simplified scheme of photochemical reactions involving (singlet) oxidized flavins (^{1}Fl).

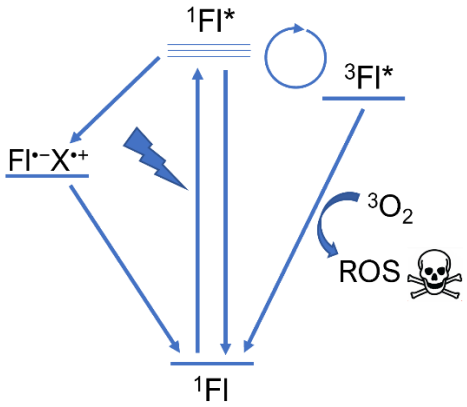

In "non-photoactive" flavoproteins, upon excitation the excited state of oxidized flavin is often rapidly quenched, usually in the hundreds of femtoseconds to several picosecond range, by photoinduced electron transfer (ET) from nearby electron-donating residues (tyrosine [indicated as TyrOH or YH] and tryptophan [indicated as TrpH or WH]), and the resulting radical pair decays by charge recombination, either directly or after further charge transfer reactions among nearby residues, usually in the picosecond time range.[12,31–34] These quenching processes thus efficiently compete with the natural fluorescence decay of flavins, in the range of a few nanoseconds. The driving force for tryptophan and tyrosine photooxidation is estimated at ~1.2 eV[35] and 0.7–1.0 eV,[31,36] respectively, and the reaction is thought, at least for tyrosine donors, to be near-barrierless.[31,37] According to classical Marcus theory, the rate of such a reaction depends on the configuration of the donor-acceptor pair, which determines the electronic coupling and the energetics involved.[38] Using a rough estimate based on distance and average protein density only,[39] direct electron donors located up to at most ~1 nm can efficiently compete, in the case of barrierless ET, with the nanosecond decay times of intrinsic excited-state decay to the singlet or triplet ground state. In many proteins (for instance glucose oxidase [GOX] in Figure. 1.2) tyrosines and/or tryptophanes are located much closer, up to near-van der Waals interaction with the flavin, and hence ET reactions can be much faster. These processes do not accumulate any photoproducts but rather avoid them, thermally dissipating the photon energy on an ultrafast timescale. This can be viewed as photoprotective self-quenching to prevent the formation of triplets and therewith, in the presence of molecular oxygen, harmful radical oxygen species (ROS) due to a long-lived excited state of the cofactor (Scheme 1.3).[40] It has been proposed that the photoprotective effect of the presence of ET-quenchers in the close vicinity of the flavin cofactor yields a strong selection pressure in the evolution of flavoenzymes that do not perform photobiological functions.[41,42]

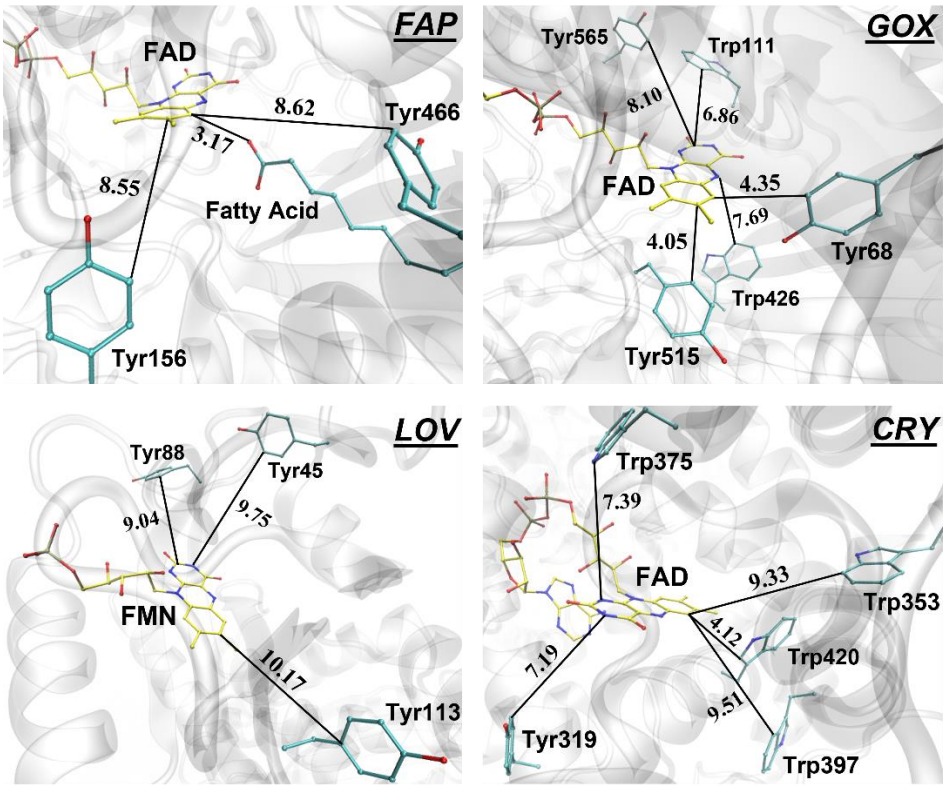

Figure 1.2 Active sites in the crystal structures of FAP from *Chlorella variabilis* (PDB entry: 6ZH7), GOX from *Aspergillus niger* (PDB entry: 1CF3), LOV from *Rhodobacter Sphaeroides* (PDB entry: 4HJ3), and CRY from *Drosophila melanogaster* (PDB entry: 4JZY), featuring tryptophan or tyrosine residues in the flavin environments. The carbon atoms of the flavin cofactors are shown in yellow, whereas those of selected active-site residues, and of the fatty acid substrate for FAP, are displayed in cyan; nitrogen, oxygen and phosphorus atoms are colored in blue and red, and brown, respectively. The closest distances between flavin rings and nonhydrogen atoms of side chains are shown in Å. For CRY, Trp420 and Trp397 are the first two constituents of the tryptophan triad ET chain.

On the other hand, in light-responsive flavoproteins, that use the photon energy to initiate chemical and/or structural transformations that cannot be achieved in the ground state,[25,29,43] an excited state with a sufficient lifetime is of functional importance. In such systems, quenching processes by residues of the protein itself, insofar as they are not part of the functional reaction scheme, could be competitive and detrimental.

For instance in FAP, one of the two native flavin-dependent photoenzymes that have been discovered so far, a cascade of reactions is initiated by photoinduced ET, in ~300 ps, from the fatty acid substrate to the oxidized flavin cofactor (FAD_{ox}).[29] ET from close-by tyrosine or tryptophan residues to the flavin would compete with this functional reaction and consequently lower the yield of the photocatalytic decarboxylation reactions. Inspection of the crystal structure of FAP (Figure 1.3) reveals that indeed the nearest electron-donating residues are located over 8 Å (minimal ring-to-ring distance), much further than the carboxyl group of the

substrate electron donor, and much further than the closest aromatic residues found typically in "non-photoactive" proteins, such as GOX, from the same glucose–methanol–choline (GMC) oxidase family of flavoenzymes as FAP, where the excited FAD_{ox} cofactor (FAD_{ox}^{*}) is effectively quenched by photoinduced ET from close-by tyrosines to FAD_{ox}^{*} in a few picoseconds;[12,32,44] the resulting $FAD^{\bullet-}$/$TyrOH^{\bullet+}$ radical pairs subsequently recombine, either directly or following further ET and proton transfer processes (Scheme 1.4).[12]

Scheme 1.4 Minimal kinetic model describing the photoinduced ET reactions in GOX. k_i are forward reaction rates and k_i' are recombination rates. The yield for each step is indicated by φ. K_i represent pseudo-equilibrium constants. Reprinted from ref. 12.

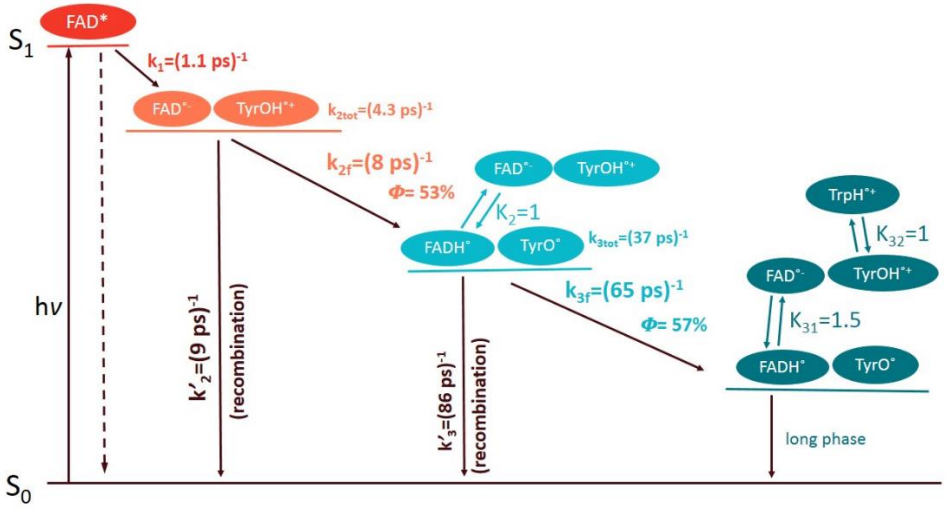

As shown in Figure 1.2, the LOV domain from plant phototropin photosensors, which contains an FMN cofactor, also is devoid of electron-donating residues surrounding the flavin cofactor. Here, upon formation of the triplet excited state ^{3}FMN* with high yield by intersystem crossing from the photo-generated singlet excited state ^{1}FMN* in a few nanoseconds, a flavin-cysteine adduct is formed on the microsecond timescale that is a precursor of more remote structural changes.[45–47] Therefore, in this system the triplet state is part of the signaling pathway, and quenching of ^{1}FMN* by ET reactions competing with decay to the triplet state would be unfavorable.

By contrast, in CRY the signal-transmission chains are thought to rely on successive ET reactions along a conserved tryptophan triad after the initial sub-picosecond photoinduced ET between the oxidized flavin cofactor and the nearby tryptophan ~4 Å away.[10] This allows efficient charge separation and stabilization of the $FAD^{\bullet-}$/$TrpH^{\bullet+}$, and ultimately $FAD^{\bullet-}$/$Trp^{\bullet}$, radical pair that plays an important role in blue-light adaptation in different organisms in a wide variety of ways, although the precise nature of the more down-stream events still remain

uncertain in many cases. Moreover, in some CRY, a distal tyrosine residue can also be involved as the fourth member to extend the classical ET chain. The resulting $FAD^{\bullet-}$/$TyrO^{\bullet}$ radical pair has a lifetime of tens of milliseconds, facilitating further flavin protonation that accumulates neutral flavin radical $FADH^{\bullet}$ that has been suggested to be involved in red-light sensing (Scheme 1.5).[13] There are also increasingly strong indications that CRY in the retina of migratory birds are involved in their orientation sensing through an (earth) magnetic field effect on the spin conversion yields based on photoinduced radical pair formation.[48]

Scheme 1.5 The proposed mechanism of FAD_{ox} photoreduction in CRY from *Chlamydomonas reinhardtii* reprinted from ref. 13. PT: proton transfer; F: forward; B: backward; PCET: proton coupled ET.

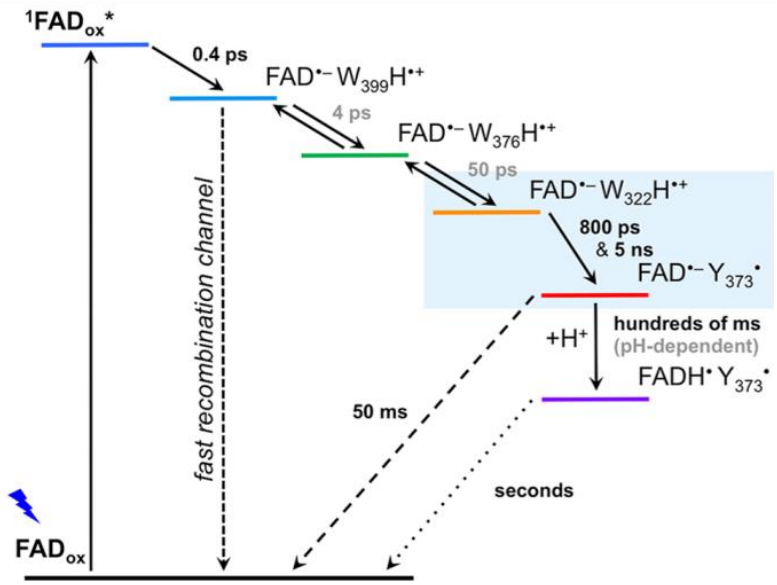

Intriguingly, the photochemistry of the one other (than FAP) native flavin-dependent photoenzyme, DNA photolyase, which is homologous to CRY photoreceptor, involves the excited state of a fully reduced flavin cofactor $FADH^{-}$. In the photo-repair process, the repair of UV-induced DNA lesions is initiated by photoinduced ET from $FADH^{-}$ to the DNA substrate, yielding $FADH^{\bullet}$.[43,49] This mechanism has inspired a recently emerging approach in the development of non-native flavin-dependent photocatalysts by employing flavins in the fully reduced form instead of the oxidized form. This circumvents the self-quenching mechanisms and enables functional photochemical transformations in "non-photoactive" flavoproteins, as the excited state of fully reduced flavins energetically cannot be quenched by nearby redox-active residues, as demonstrated by DNA photolyase.[50,51] In particular, ene-reductases such as old yellow enzyme that harbor a versatile substrate-binding site have recently been explored following this principle. In those systems, photoreduction of alternative

substrates by ET from excited fully reduced flavin has been shown to initiate a variety of reactions, including stereoselective cyclization and reductive breaking of double bonds.[50]

Primary photochemical reactions in flavoproteins have been experimentally studied using in particular ultrafast spectroscopic techniques. In some cases, these are complemented by computational studies especially focusing on molecular dynamics (MD) simulations in combination with ET theory and quantum chemical approaches.[34,52–54] Recently, the development of a high-quality force field for flavins has facilitated MD simulations.[55] The work presented in this thesis builds on and extends these approaches, by exploiting results of ultrafast spectroscopy experiments of flavoproteins and redox conditions selected for their potential novel insight, and in many cases combining them with computational approaches.

Given the vast chemical versatility of the flavin ring, we envisage that new photochemistry of different flavin species with practical implications awaits the field. Thus far in the literature, the experimental and computational studies of flavoprotein photochemistry have been mostly centered on the ET kinetics of photoreduction of oxidized flavins. Understanding of fundamental photochemical processes that involve the excitation of flavins in other redox states or chemical forms are still very limited and insight obtained from direct comparison of experimentally obtained and theoretically predicted spectral properties of intermediates, including for photoreduction of oxidized flavins, is quasi-absent. In this work, combining ultrafast spectroscopic measurements and computer simulations, we have investigated in-depth the photochemical processes of protein-bound flavin species in different redox states or chemical forms. In particular, we have focused on the spectral properties of flavins as well as other reaction intermediates in the photochemical transformations, which can provide useful insights into the ground- and excited-state electronic structures of those species, as well as the interactions between flavins and protein environments.

The rest of this thesis is organized as follows:

The details of experimental and computational approaches used in this work are described in **Chapter 2**. Time-resolved fluorescence spectroscopy employing a Kerr gate was used to follow the excited-state dynamics of flavin species, and multicolor time-resolved absorption spectroscopy based on the pump-probe technique was used to characterize the nature of photoproducts. For simulations, classic molecular dynamics (MD) simulations were applied to study the structural dynamics of proteins. A hybrid quantum mechanics/molecular mechanics (QM/MM) approach and density functional theory (DFT), as well as time-

dependent DFT (TDDFT), were used to calculate the properties of the excited-state and of reaction intermediates.

Chapter 3 presents the results that we have obtained on the spectral properties of the short-lived radicals of flavin, tyrosine and tryptophan in ferredoxin-$NADP^+$ oxidoreductase from *Bacillus subtilis* (*Bs*FNR) upon excitation of the FAD_{ox} cofactor. In this system, a tyrosine or a tryptophan residue is located at near van der Waals distances to the flavin, allowing extremely fast formation of a photoinduced flavin–residue radical pair, facilitating the characterization of the reaction intermediates in the charge-separated state with respect to other recently studied systems.[12] This system is also well suited for exploring, both experimentally and theoretically, the effect of the close interaction of the redox partners on the spectral properties.

To explore potential photochemical reactions that may be useful in application of flavoproteins as photocatalysts or optogenetics tools, we have further focused on the photochemistry of flavin forms other than the oxidized resting state. Anionic flavin radicals can be stabilized in flavoprotein oxidases that harbor functional positively charged residues in the active site. **Chapter 4** describes the discovery of the ultrafast photooxidation of protein-bound anionic flavin radicals and the exploration of the possible role of positively charged residues.

As photochemical processes of fully reduced flavins play a role in bio-engineered photocatalysts,[50,51] a basic understanding of the competing excited-state deactivation processes is warranted. **Chapter 5** contains a study on excited-state decays of fully reduced flavins in protein systems where they are involved as functional intermediates, and compare them with aqueous solution. In specific FNR systems, the excited state of the fully reduced flavins decay with unprecedentedly fast rates, and the molecular origin of this finding was investigated.

The photochemistry of yet other forms of the versatile flavin rings, including charge-transfer (CT) complexes, may also await practical applications, but is largely unexplored. In **Chapter 6**, we present the first full-spectral investigation on the photochemical processes that follow the excitation of a flavin–inhibitor CT complex in a flavoenzyme, i.e., the CT complex of FAD_{ox} and methylthioacetate (MTA) in a physiologically non-photocatalytic flavoenzyme, monomeric sarcosine oxidase (MSOX). This system appears to act as an ultrafast photo-switch of the non-covalently bound inhibitor.

This thesis is in part based on articles that are published: the present chapter is partly adapted from ref. 42, and **Chapter 3**, **4** and **6** are largely adapted from ref. 56, 57 and 58, respectively. Finally, the overall conclusions and perspectives of this work are given in **Chapter 7**.

Chapter 2. Methods

2.1 Protein preparation

Many of the proteins used in this study were commercially available products from Sigma-Aldrich, including GOX, MSOX, choline oxidase (COX), and D-amino acid oxidase (DAAO). All proteins were used without further purification, except for DAAO, where excess free flavin content was removed before use by washing with excess buffer followed by concentrating with a 30-kDa cutoff Amicon Ultra 4 filter (Millipore). The other protein samples were prepared by external or internal collaborators, and protocols for the expression and purification can be found in the literature, including wild-type (WT) and variants of FNRs[59–61] (by Dr. Daisuke Seo, Kanazawa University), as well as nitronate monooxygenase[57] (NMO, by Mr. Rivo Ramodiharilafy, LOB, Ecole Polytechnique).

2.2 Production of semi-reduced and fully reduced flavins

Chapter 4 and **5** focus on the study of reduced flavin species, which were produced by chemical reduction or photo-reduction under anaerobic conditions at room temperature following reported methods.[5,7,24,60,62] Briefly, $FAD^{\bullet-}$ in GOX, COX and MSOX, as well as free $FADH^-$ and $FADH_2$ were prepared by reducing FAD_{ox} in the proteins and in aqueous solution with an excess amount of sodium dithionite (2–4 fold excess to maintain the anaerobic conditions during the ultrafast spectroscopic measurements). Fully reduced flavins in FNRs were prepared with a similar method but a trace amount of methyl viologen was also added as a mediator. $FMN^{\bullet-}$ in NMO was obtained by reduction of FMN_{ox} with propionate 3-nitronate, and $FADH^-$ in GOX by reduction of FAD_{ox} with D(+)-glucose. $FAD^{\bullet-}$ in DAAO was produced by photoreduction in the presence of 2-mercaptoethanol under blue-light irradiation (at 450 nm from a LED lamp) in an ice bath.

2.3 Pump–probe spectroscopy

Pump–probe spectroscopy is a popular class of spectroscopies for studying ultrafast phenomena. In these techniques, the pump and the probe are generally derived from a single source by splitting an ultrashort laser pulse into two portions. A delay line is used to create a time difference in arrival of the probe beam with respect to the pump at the interaction volume,

typically a sample cell but there can exceptions (see Section 2.4). The time resolution is created by moving the mechanical delay line (Figure . 2.1), where a change in the delay line position of 150 µm corresponds to a pathlength difference of 300 µm and hence a time delay of 1 ps. The experiment is repeated at different set delay times to construct the kinetics point by point as a function of time delay. The following two sections describe the two different pump–probe spectroscopies that we used in our study for investigating the excited-state and photoproduct properties of flavins.

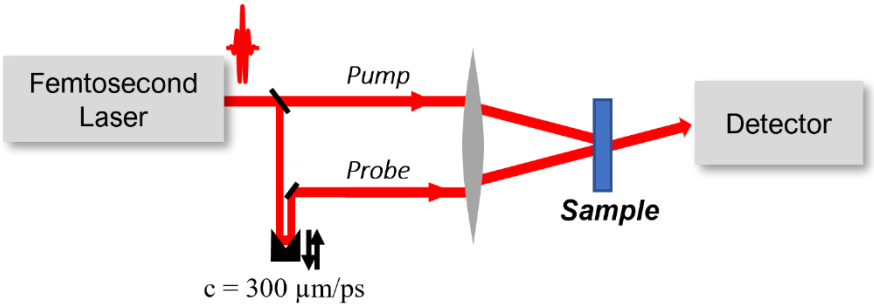

Figure 2.1 Schematic of the principle of pump–probe spectroscopy.

2.4 Femtosecond time-resolved fluorescence spectroscopy

Time-resolved fluorescence spectroscopy represents a direct measurement of the decay of an emissive excited state. The fluorescence spectra can alter during the decay due to spectral relaxations and to contributions of different species. Therefore, we use a method that has both high temporal resolution and the ability to measure full spectra, by employing a Kerr gate. Compared with other experimental methods that provide combined time and spectral resolution in time-resolved fluorescence measurements, such as streak cameras and broadband upconversion, Kerr gate setups have a relatively better time resolution than streak cameras and are more straightforward in operating than broadband upconversion.

When interacting with a suitably polarized intense gated pulse, the Kerr medium changes its refractive index and becomes temporarily birefringent. The polarization of the sample fluorescence induced by the excitation beam that passes the Kerr medium while the induced birefringence persists will be changed. Therefore, when the Kerr medium is placed between two crossed polarizers, part of this fluorescence passes through the second polarizer and can be detected. This allows the measurement of fluorescence intensity as a function of the time delay between the arrival of excitation and gated pulses, therefore, based on the principle of pump–probe spectroscopy but here the pump beam excites the sample, and the "probe" beam gates the fluorescence through the Kerr medium. Depending on the time-resolution required,

different Kerr media (with distinct response times and response amplitudes) have been used for obtaining the time-resolved fluorescence data in these experiments: suprasil (~200 fs, electronic response, in principle determined by the cross-correlation of the excitation and gate pulse), benzene (~300 fs) and CS_2 (~1 ps); in the latter two cases determined by the molecular response of the Kerr medium. The response amplitudes of these Kerr media are in inverted order. Depending on properties of the sample and the requirement of the experiment, a compromise between time resolution and signal to noise ratio can be chosen.

In our setup, part of the 780 nm output from the Ti:sapphire laser/amplifier system (Quantronix Integra-C) operating at 0.5 kHz was passed through a β-Barium Borate (BBO) crystal, yielding an excitation pulse centered at 390 nm. The remaining 780 nm beam was directed through a motorized delay line and focused into the Kerr medium where it spatially overlapped the fluorescence from the sample. The sample is contained in a quartz cell with an optical path of 1 mm. To avoid photobleaching and sample degradation, the cell is rotated continuously during the experiment so that a new volume of the sample is excited every shot.

2.5 Femtosecond time-resolved absorption spectroscopy

Time-resolved fluorescence spectroscopy is useful for obtaining information exclusively on the lifetimes of the excited state. To visualize the formation of photoproducts following flavin excitation, femtosecond time-resolved absorption spectroscopy was performed. The pump beam is used to excite the sample, and the probe beam is used to monitor the pump-induced changes in the absorption spectra of the sample.

The laser source for the setup used for time-resolved absorption experiments is the same as the one for fluorescence experiments. It is split into two portions. One part is passed through a BBO crystal to generate a 390 nm beam. This beam is either directly used as a pump beam or used to pump a non-collinear optical parametric amplifier to generate beams centered at either 520 or 560 nm. The spectra of the latter beams are tailored with sharp-edge interference filters. The pump beam is passed through the delay line to create a temporal delay with respect to the probe pulse. The latter is obtained by focusing the second part of the 780-nm beam on a continuously translated CaF_2 plate for continuum generation. The resultant white pulse is then compressed using two prisms and passed through another beam splitter to have separate test and reference beams to correct for shot-to-shot variations of the probe beam.

Conventionally, the polarization is kept at magic angle (54.7°) to avoid anisotropy effects. During this work, additional photo-selection experiments have also been performed.

Here, parallel and perpendicular pump–probe configurations have been used for recording the transient anisotropy data, where the polarization of the probe beam remains unchanged, and the pump beam polarization is rotated using a λ/2 plate. For pumping and probing single transitions, the anisotropy *r* is defined as:

$$r = \frac{\Delta A_{\parallel} - \Delta A_{\perp}}{\Delta A_{\parallel} + 2\Delta A_{\perp}} \qquad (2.1)$$

where $\Delta A_{\parallel}$ and $\Delta A_{\perp}$ are the transient absorption spectra measured with the pump and probe pulses polarized parallel and perpendicular, respectively. *r* is related to the angle ϕ between the pumped and probed transition as:

$$r = \frac{3cos^2\phi - 1}{5} \qquad (2.2)$$

The value of *r* can vary between 0.4 (for ϕ = 0°) and −0.2 (for ϕ = 90°).

Using $[Ru(bpy)_3]Cl_2$ as a reference, we can determine the initial concentrations of excited molecules in the protein sample (c_S^*) in transient absorption measurements. Under the same excitation conditions, we have:

$$c_S^* = \frac{c_{Ru}^* \left(1 - 10^{-A_S^{gs}}\right)}{1 - 10^{-A_{Ru}^{gs}}} \qquad (2.3)$$

where c_{Ru}^* is the concentration of the excited Ru complex, A_S^{gs} and A_{Ru}^{gs} are the ground-state absorbance of the protein sample, and the $[Ru(bpy)_3]^{2+}$ sample at the excitation wavelength, respectively.

Upon excitation, $[Ru(bpy)_3]^{2+}$ undergoes a charge transfer reaction resulting in a long-lived metal-to-ligand charge transfer state. The reaction has a 100% quantum yield and the difference of molar extinction coefficient of $[Ru(bpy)_3]^{2+}$ at 450 nm following this reaction has been reported to be -1.1×10^4 $M^{-1}cm^{-1}$,[63] which can be used to calculate c_{Ru}^* in the transient absorption measurement.[64]

2.6 Global analysis of the time-resolved data

The data from the time-resolved experiments were analyzed in terms of multi-exponential functions using the open-source software Glotaran for global analysis.[65]

Time-resolved spectroscopy data are measured as a function of the spectral variable wavelength λ and the independent variable time delay *t* relative to the instant of excitation. The

model underlying the data matrix Ψ (measured as fluorescence intensity in time-resolved fluorescence or difference in absorption in time-resolved absorption measurements) is a superposition of n_{comp} components given by equation 2.4:

$$\Psi(\lambda, t) = \sum_{l=1}^{n_{comp}} c_l(t)\epsilon_l(\lambda) \qquad (2.4)$$

where c_l and ϵ_l are the unknown concentration profile and spectrum of component l respectively. In an actual time-resolved measurement, c_l and ϵ_l are determined by the rate constants of the exponential functions and their associated wavelength–dependent pre-factors that the experiments aim to uncover, but also the instrument response function (IRF, described by a Gaussian temporal function and the zero-of-time), wavelength-dependence of the zero-of-time (described by a polynomial function) due to dispersion in the absorption probe or fluorescence beam, and possibly (cross-phase modulation) artifacts during the pump-probe temporal overlap in transient absorption experiments. After defining a model for the concentration of each component l, equation 2.4 can be represented mathematically as:

$$\Psi(\lambda, t) = \sum_{l=1}^{n_{comp}} c_{l,\lambda}(t, \theta)\epsilon_l(\lambda) \qquad (2.5)$$

where θ represents all the parameters on which the concentration profile depends. Θ and $\epsilon_l(\lambda)$ are now obtained by fitting.[66]

After obtaining a reasonable fit $\Psi'(\lambda, t)$ by judging from the progression of the sum of squares of errors during the iterations and singular value decomposition of the residual matrix, the results can be depicted in terms of decay associated spectra (DAS), so that

$$\Psi(\lambda, t) = \sum_{l=1}^{n_{comp}} c_l^{DAS}(t, \theta)DAS_l(\lambda) \qquad (2.6)$$

where $c_l^{DAS}(t, \theta)$ is an exponentially decay function with time constant θ convoluted with the IRF. In a kinetic scheme where n_{comp} components decay independently and mono-exponentially in parallel, the $DAS_l(\lambda)$ correspond to the spectra of these components. Furthermore, assuming a sequential model where the components decay sequentially in an unbranched, unidirectional manner with increasing lifetimes (A → B → ... → n), evolution associated spectra (EAS) can be obtained by linear combinations of $DAS_l(\lambda)$. These EAS represent the spectra of the intermediate states in the framework of this model.

2.7 Classical MD simulation

MD simulation is a computational method that numerically solves Newton's equation of motion to study the time evolution of interacting atoms or molecules. It allows investigating events with a time scale and spatial resolution that are difficult to directly describe by experimental methods. Though *ab initio* method can be used with MD simulations, most often classical molecular mechanics (MM) based on an empirical energy function called a force field is used to model inter-atom interactions within the systems. In MM, atoms in molecules are represented by particles of a given mass and interactions between atoms have two contributions:

$$V_{total} = V_{bonded} + V_{non-bonded} \qquad (2.7)$$

where V_{bonded} describes the interactions between bonded atoms through the covalent structure and $V_{non\text{-}bonded}$ results from interactions between atoms which are separated by more than two bonds in the same molecule, or between atoms of different molecules. In class I force fields, V_{bonded} includes terms due to bond stretching (V_l), valence angle bending (V_θ) and torsional angle (V_ϕ) motions, which are given by the following functions:

$$V_l = k_l(l - l_0)^2 \qquad (2.8)$$

$$V_\theta = k_\theta(\theta - \theta_0)^2 \qquad (2.9)$$

$$V_\phi = \sum_n \frac{V_n}{2}[1 + \cos(n\phi - \gamma)] \qquad (2.10)$$

In Eqs. 2.8 and 2.9, l and θ are the bond length and the bond angle, l_0 and θ_0 are the corresponding equilibrium values, and k_l and k_θ are the corresponding force constants. In Eq 2.10, ϕ is the dihedral angle, n and γ are the periodicity and phase angle of the cosine function, and V_n is the amplitude of the energy barrier. In addition, the bonded part may include additional terms, such as improper angle terms, mainly used to preserve planarity of molecules (as in the CHARMM C36 force field) and cross terms, Urey-Bradley (UB), which is a bond-angle cross term, and CMAP cross term used only for peptide backbone dihedral angles.

The interaction potential $V_{non\text{-}bonded}$ is composed by a van der Waals term (V_{vdW}) and an electrostatic term (V_e). In class I force fields (such as Amber, CHARMM and OPLS) commonly a Lennard–Jones (LJ) potential is used to describe the former and the latter is given by a Coulomb law acting between point changes located at atomic centers:

$$V_{LJ}(r_{ij}) = 4\varepsilon_{ij}[\left(\frac{\sigma}{r_{ij}}\right)^{12} - \left(\frac{\sigma}{r_{ij}}\right)^{6}] \qquad (2.11)$$

$$V_e(r_{ij}) = \frac{q_i q_j}{r_{ij}} \qquad (2.12)$$

where ε_{ij} is the dispersion energy and σ is the size of the atom; q_i and q_j are the charges on atoms *i* and *j* respectively. In both Eq 2.11 and 2.12, r_{ij} refers to the distance between atomic centers *i* and *j*.

Altogether, a typical class I MM potential can be represented by Eq 2.13:

$$V_{total} = \sum_{bonds} k_l(l - l_0)^2 + \sum_{bonds} k_\theta(\theta - \theta_0)^2 + \sum_{dihedral} \sum_{n} \frac{V_n}{2}[1 + \cos(n\phi - \gamma)] + \sum_{i} \sum_{j>i} 4\varepsilon_{ij}\left[\left(\frac{\sigma}{r_{ij}}\right)^{12} - \left(\frac{\sigma}{r_{ij}}\right)^{6}\right] + \sum_{i} \sum_{j>i} \frac{q_i q_j}{r_{ij}} \qquad (2.13)$$

As stated above the term force field refers to a specific mathematical form of V_{total} , as well as to the set of empirical parameters. A large number of force fields have been developed so far, including CHARMM, OPLS, AMBER and GROMOS.[67]

With the force field model for calculating the potential energy defined, MD simulations can be performed by solving the differential equations of the motion described by the Newton's second law, starting from given initial configurations which frequently correspond to experimentally determined structures obtained from databased such as the Protein Data Bank (PDB). The protein is usually placed in a simulation box (which can be cubic or orthorhombic) filled with water molecules. Ions (Na^+, K^+ and Cl^-) can also be added to simulate the physiological conditions, as well as to neutralize the total charge of the system. Periodic boundary conditions (PBC) are assumed to avoid the artefacts of the finiteness of the simulation box and limit the number of atoms to be followed in time, where Ewald summation is usually applied to compute the long-range electrostatic interactions.[68]

In my studies, the CHARMM program (version 45b2)[69] was used to set up the systems for simulations, and MD simulations with classical force fields were carried out using the NAMD program (version 2.13).[70] The protein models were prepared based on experimental protein structures taken from the PDB. The CHARMM36 force field[71] was used for the protein residues and the TIP3P model for water;[72] a recently developed force field for flavins was used for the FAD cofactor in different redox states.[55] The protonation states of all titratable residues

were assigned based on a PROPKA 3.1 analysis[73] and verified by ideal stereochemistry. PROPKA predicts pK_a values based on protein 3D structures and on empirical physical descriptors, including residue desolvation and protein dielectric response. Proteins were centered in cubic water boxes, at least 12 Å away from each of the box edges. PBC were assumed, and an appropriate amount of K^+ was included to neutralize the net charge of the system. The integration time step was set at 2 fs. During the simulations, macroscopic parameters are kept constant, as experiments are usually performed at constant temperature and pressure. After energy minimization, the system was equilibrated first in an NVT ensemble for 50 ps, followed by a 500 ps simulation in the NPT ensemble, at 295 K and 1.0 atm pressure before the production runs. The Berendsen thermostat and barostat were employed, with a relaxation time of 500 fs and 4 timesteps between position rescalings.[74] The analyses of the MD trajectories were performed either directly by CHARMM, or via the molecular visualization program VMD (version 1.9.3).[75]

Based on MD simulations, it is also possible to further calculate the free energy changes of ET or PT reactions involving amino acids or cofactors in proteins by solving the Poisson–Boltzmann (PB) equation (semi-empirical macroscopic model with the protein dielectric constant being an adjustable parameter), or through rigorous MD free energy (MDFE) calculations, which represent two different approaches for evaluating the electrostatic effects of the protein environments compared with a reference system (usually those isolated in solution). The former treats all atoms of a biomolecule as particles with low electrostatic potential and partial point charge at atomic positions to calculate the electrostatic potential throughout the space.[76,77] The latter explicitly calculates the free energy changes of the reaction by performing thermodynamic integration on a given energy function that changes from the initial state to the final state stepwise,[78–80] which is therefore more extensive and computationally more expensive.

2.8 DFT calculation

DFT is a popular modelling method based on quantum mechanics (QM) to investigate the electronic structure of many-body systems, including atoms, molecules, and crystalline solids. In many-body electronic structure calculations, solving the many-body Schrödinger equation can be highly sophisticated, and DFT provides an appealing alternative to approach the problem. DFT usually can provide much higher accuracy than Hartree−Fock (HF) calculations at a lower computational cost than Møller−Plesset (MP) perturbation theory. In contemporary DFT techniques, the electronic structure is evaluated using a potential acting on

the electrons of the system. This systematically maps the many-body (*N*-electron) problem onto a single-body problem, expressed in terms of the one electron density $n(\boldsymbol{r})$ defined as:

$$n(\boldsymbol{r}) = N \int \cdots \int |\Psi(\boldsymbol{r}, \boldsymbol{r}_2, \cdots, \boldsymbol{r}_N)|^2 \mathrm{d}^3\boldsymbol{r}_2 \cdots \boldsymbol{r}_N \qquad (2.14)$$

It can be demonstrated that for a given ground-state density $n_0(r)$, it is possible to calculate the ground-state wave function Ψ_0. In other words, Ψ_0 is a unique functional of n_0, and all other properties as well. The Hohenberg–Kohn (HK) theorems[81] state that the external potential (and hence the total energy) of a given system is a unique functional of the electron density, and the ground-state energy can be obtained by minimizing the energy functional. Furthermore, the Kohn–Sham (KS) method[82] provides a way to approximate the energy functional, which leads to the KS equation:

$$\left(-\frac{\hbar^2}{2m}\nabla^2 + v_{\text{eff}}(\boldsymbol{r})\right)\varphi_i(\boldsymbol{r}) = \varepsilon_i \varphi_i(\boldsymbol{r}) \qquad (2.15)$$

where v_{eff} is the KS potential defined by a local effective (fictitious) external potential in which the non-interacting particles move, ε_i is the orbital energy of the corresponding KS orbital φ_i, and the electron density for *N*-electron system is:

$$n(\boldsymbol{r}) = \sum_i^N |\varphi_i(\boldsymbol{r})|^2 \qquad (2.16)$$

The KS equation is solved in a self-consistent (i.e., iterative) way, starting with an initial guess for $n(\boldsymbol{r})$ and the true ground-state density can be obtained upon convergence. The functional for calculating the energy can be constructed in different ways, and different forms of mathematical functions (basis sets) can be used to build the molecular orbitals. The B3LYP (Becke, 3-parameter, Lee–Yang–Parr) exchange-correlation functional[83,84] and the Pople basis sets[85,86] are arguably the most popular combinations in the practice of DFT for biological systems, and they were extensively used in my studies.

TDDFT is an extension to conventional DFT, which conceptual and computational foundations are analogous to those of DFT. In the framework of TDDFT, for a given initial wavefunction, there is a unique mapping between the time-dependent external potential of a system and its time-dependent density (Runge–Gross theorem, the time-dependent analogue of the HK theorem).[87] TDDFT allows the calculation of excited-state properties, which essentially can be used to derive the electronic absorption spectrum.

There are many quantum-chemistry packages that support DFT and TDDFT calculations. In the study, the ORCA program (version: 4.2)[88] was used to perform these calculations. The B3LYP functional was used in most cases, and the Pople basis sets, or Ahlrichs def2 basis sets[89] were used depending on the investigated systems. Further analysis and visualization of the results were carried out with the help of the Multiwfn program (version 3.8).[90]

2.9 QM/MM calculation

In the present thesis, we are interested in the electronic transitions of a molecule, which only can be investigated by considering the electronic structure. However, in the case of biological systems, applying QM methods to whole systems is highly impracticable due to the size of the systems. The hybrid QM/MM approach provides an alternative multiscale strategy,[91,92] which divides the system into a MM region where the atomic interactions are described by classical MM, and a QM region on which we can apply high-level QM methods.

In an additive QM/MM coupling scheme, the potential energy for the whole system is a sum of MM terms, QM terms and QM/MM coupling terms:

$$E_{QM/MM} = E_{QM}(\boldsymbol{QM}) + E_{MM}(\boldsymbol{MM}) + E^{int.}_{QM/MM}(\boldsymbol{QM} + \boldsymbol{MM}) \qquad (2.17)$$

The QM/MM coupling generally includes bonded, van der Waals (vdW) and electrostatic interactions between QM and MM atoms:

$$E^{int.}_{QM/MM}(\boldsymbol{QM} + \boldsymbol{MM}) = E^{B}_{QM/MM} + E^{vdW}_{QM/MM} + E^{E}_{QM/MM} \qquad (2.18)$$

$E^{B}_{QM/MM}$ is present when the QM and the MM regions are covalently linked. Here usually a link-atom method is used to deal with the QM/MM boundary. The boundary "atom" has two components: the MM atom, with its associated classical force field parameters, which represents the boundary atom in the MM calculation, and a hydrogen link-atom, which is included in the QM calculation. The gradients of the energy with respect to the link-atom coordinates can be partitioned between the parent MM and QM atoms by application of the chain rule. The second term of Eq 2.18, $E^{vdW}_{QM/MM}$ is related to the vdW interactions between MM and QM atoms, and in the most common formulations of QM/MM methods, these interactions are treated at the force field level, through a LJ potential (See Eq 2.11). The third term of Eq 2.18, $E^{E}_{QM/MM}$ usually plays the most important role in the correct description of the effects of the MM region on the QM region. The different methods for obtaining $E^{E}_{QM/MM}$ are

commonly referred to as *embedding*. Widely used formulations include mechanical embedding and electrostatic embedding. The former treats the QM subsystem as a set of point atomic charges that interact with MM region through the standard Coulomb interactions; the latter is more accurate where the influence of partial charges from the MM region is introduced in the quantum Hamiltonian for the QM region and also the choice for my studies.

In this study, we used the pDynamo program (version 1.9.0)[93] to perform the QM/MM calculations. The MM region is treated with the CHARMM force field while the QM region is described by DFT (levels of theory depend on the investigated systems). The ensemble of protein structures is prepared by taking equally spaced snapshots along the stabilized trajectories of MD simulations (usually, 100 snapshots from 100-ns MD trajectories to have converged statistics) which are subsequently used for QM/MM calculations. All QM calculations for the QM/MM method are performed with the ORCA package, including TDDFT. In the geometry optimization of the QM region, usually the atoms in the MM region were kept fixed, and the L-BFGS optimization method was used during the energy minimization, with a RMS gradient tolerance of 0.2 kcal/(mol·Å) as the convergence criterion.

Chapter 3. Photoreduction of Oxidized Flavins and Characterization of Short-Lived Intermediates

3.1 Background: *Bs*FNR as a model system

Photoreduction of oxidized flavins is a pivotal step in the functional processes of the flavin-dependent photoenzyme FAP and photoreceptor CRY. In many "non-photoactive" flavoproteins with oxidized flavin as the resting states, the photoreduction of the oxidized cofactors through ultrafast, reversible photoinduced ET from close-by redox-active residues (usually tyrosine and tryptophan) also widely occurs, which has been proposed to play a photoprotective role in increasing the photostability of the cofactors.[41,42] In these proteins, the photochemical properties can also be exploited, for instance as a tool to explore the conformational dynamics of the active site, as ET reactions are highly sensitive to the relative positions and conformations of donors and acceptors.[34,36,37] Moreover, the involvement of the tyrosine and tryptophan in these photoinduced processes also makes "non-photoactive" flavoproteins promising model systems to investigate the properties of tyrosyl or tryptophanyl radical intermediates and their interactions with corresponding flavin radicals when they coexist as radical pairs. These radical pairs are usually difficult to characterize during biochemical reactions limited by reactant binding dynamics. A schematic representation of possible photoinduced reactions involving an oxidized flavin and redox-active amino acids is given in Figure 3.1.

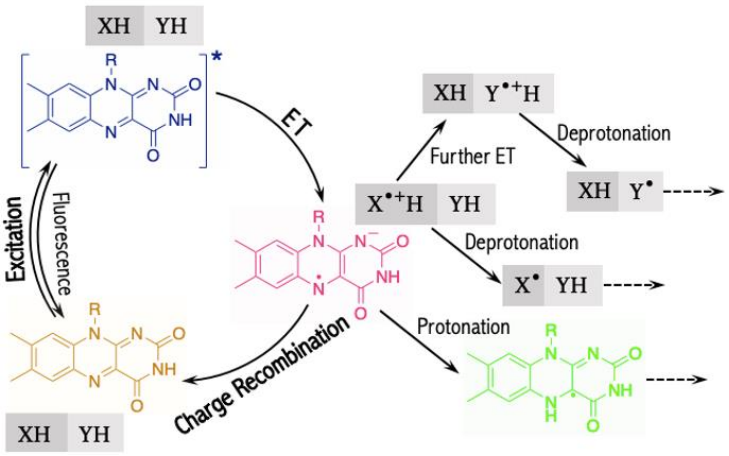

Figure 3.1 General reaction pathways follow the photoreduction of an oxidized flavin in flavoproteins. Flavin is represented by the isoalloxazine moiety. XH and YH stand for aromatic residues (tryptophan or tyrosine), for simplicity limited to two. Anion protonation and cation deprotonation may be coupled to ET, corresponding to proton transfer from a residue to flavin (not explicitly depicted). For simplicity, back reactions beyond the primary radical pair are not shown.

It has been shown that upon the excitation of semi-reduced CPD photolyase, the photoreduction reaction proceeds by successive ET steps along a chain of three conserved tryptophan residues, whereby both the protonated ($TrpH^{\bullet+}$) and the deprotonated ($Trp^{\bullet}$) tryptophanyl radicals (pK_a ~4) can be generated sequentially on the picosecond-nanosecond timescale;[19] in some cases, deprotonated tyrosyl radicals can be observed in such proteins as well.[94] Similar reaction products have later also been observed upon excitation of oxidized flavin in the related cryptochrome blue-light sensors.[10,13,95] More recently, the flavin excited state quenching by tryptophan has been examined in detail in artificial protein maquettes.[35,96] In contrast to tryptophan, for a long time it had been assumed that the oxidation of tyrosine is necessarily accompanied by a concerted deprotonation due to its extremely low pK_a (~−2). However, recent studies of modified bacterial tRNA methyltransferase, TrmFO[97,98], have spectroscopically identified a transiently formed protonated tyrosyl radical ($TyrOH^{\bullet+}$). Subsequently, this form was also assigned to transient features in the popular model flavoprotein glucose oxidase.[12] Nevertheless, in the latter reports, the formation and decay rates of the initial product states are very close, complicating the spectral disentanglement of this state, and also did not compare tyrosine and tryptophan in the same protein site. This chapter presents our study undertaken on a flavoprotein, *Bs*FNR, that has not been investigated by ultrafast spectroscopies before. *Bs*FNR harbors extremely close-lying redox partners involved in quenching, allowing better kinetic separation and spectral disentanglement between the

initial excited state and the radical pair product state. We further investigated the influence of this proximity on the spectral properties of flavin, tyrosine and tryptophan radical intermediates.

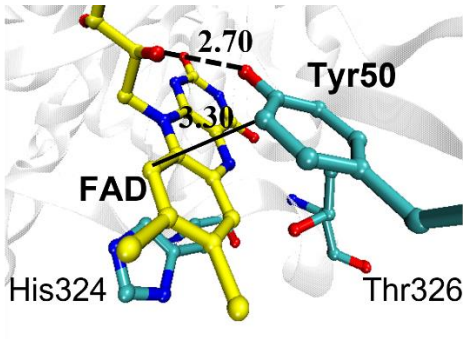

Figure 3.2 The active site of WT *Bs*FNR in the crystal structure (PDB entry: 3LZW). The distances are shown in Å.

*Bs*FNR is a homo-dimeric flavoprotein homologous to bacterial NADPH-thioredoxin reductase.[99] It catalyzes the redox reaction between the electron carrier nucleotide $NADP^+$/H and ferredoxin, a small iron-sulfur protein that also mediates ET.[61,100] A high-resolution structure of wild-type (WT) *Bs*FNR is available.[32] A tyrosine residue (Tyr50) was found to locate extremely close (shortest distance between ring atoms: 3.3 Å) to the FAD cofactor, forming an unusual π–π stacking interaction with the isoalloxazine ring assisted by a hydrogen bond interaction between its OH group and the O2´ hydroxyl group of the ribityl moiety of FAD (Figure 3.2). Previous studies have found that Tyr50 plays an important role in the functioning of the protein by stabilizing the FAD cofactor in different redox states.[59] Whereas the protein does not form known functional photoproducts, Tyr50 has been shown to strongly quench FAD_{ox} fluorescence as shown in Figure 3.3. Variants where this residue is replaced by tryptophan (Y50W) and glycine (Y50G) are also available and tryptophan can act as a quencher as well.[33] By contrast, FAD_{ox} fluorescence in the Y50G is strongly enhanced. These properties make *Bs*FNR an interesting model system to characterize the short-lived intermediates during the light-induced processes using ultrafast spectroscopy.

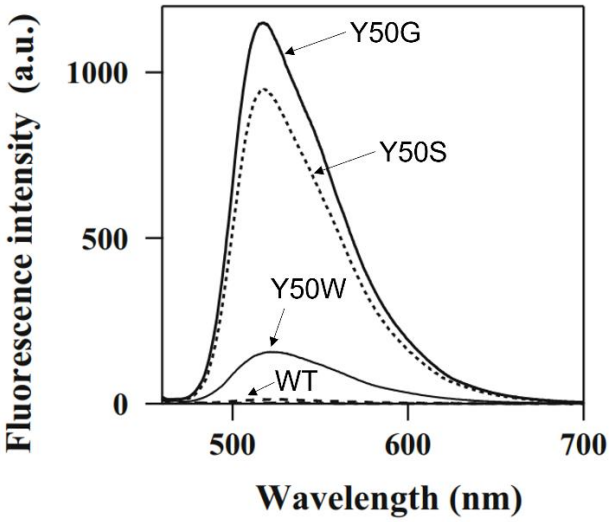

Figure 3.3 Steady-state fluorescence emission spectra of WT and mutated *Bs*FNR measured with excitation at 450 nm: free FAD (thin solid line), WT (dot-dash line), Y50G (thick solid line), Y50S (dotted line), Y50W (dashed line). Reprinted form ref. 59.

3.2 Structural dynamics of WT and Y50W BsFNR

As the configurations of electron donor and acceptor are essential in determining the ET dynamics, we first employed MD simulations to investigate the structural dynamics of the protein active sites where the ET reactions occur. Throughout the 120 ns MD simulation of WT *Bs*FNR, the stacking conformation of Tyr50 with the isoalloxazine ring moiety of FAD_{ox} was well-preserved, with fluctuations in minimal ring-to-ring distances limited to a range between 3.0 and 3.8 Å (Figure 3.4). The average distance of 3.4 Å in MD simulations between FAD and Tyr50 rings compares well with the distance in the crystal structure of 3.3 Å. Here the minimal ring-to-ring distance is defined as the shortest distance between any non-hydrogen atoms from two rings, which is thought to be relevant to the electronic coupling determining the ET rate. This particular stability of the interaction between Tyr50 and FAD will be later discussed in the context of ET. Other aromatic residues that could potentially act as the electron donors, e.g., Tyr25, Tyr56, and Trp169, are highly unlikely to compete with Tyr50 during the photoreduction of FAD_{ox} on the sub-picosecond timescale due to much longer donor–acceptor distances and unfavorable conformations.

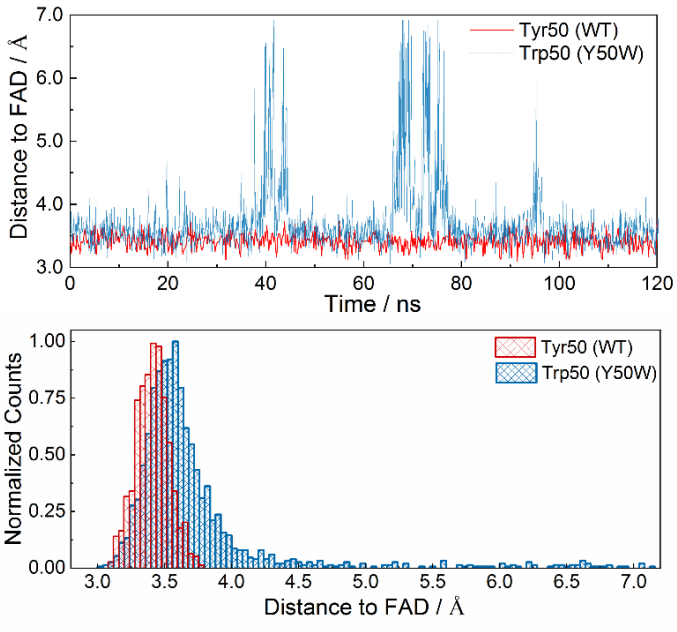

Figure 3.4 The minimal ring-to-ring distance (*top*) and distribution (*bottom*) between FAD_{ox} and Tyr50 or Trp50 in MD simulations of WT and Y50W *Bs*FNR, respectively.

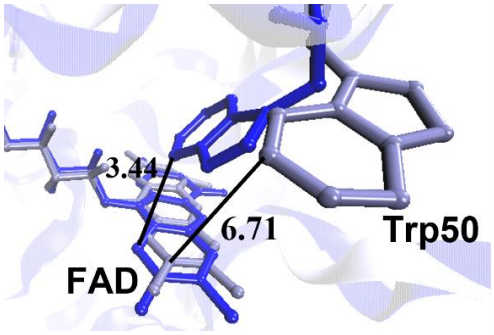

Figure 3.5 Superimposed structures with two conformations in the active site of Y50W *Bs*FNR from MD simulations. The distances are shown in Å.

Because no crystal structure of the Y50W mutant is available, it was modeled by replacing Tyr50 in the crystal structure of WT *Bs*FNR by a tryptophan (Trp50). In our simulations, the ring-to-ring distance between Trp50 and FAD_{ox} demonstrates large fluctuations on the multi-nanosecond timescale with a distribution extending to much further than that between Tyr50 and FAD_{ox} in WT *Bs*FNR (Figure 3), indicating that in the Y50W mutant the tryptophan is not well stabilized in the position corresponding to Tyr50. This can be rationalized by the absence of proper hydrogen bond and stacking interactions between FAD and the tryptophan. Although most of the time (~90%) throughout the MD simulation Trp50 and FAD remain at less than 4 Å away, there were short periods where Trp50 moved outwards and located relatively distant from FAD (> 5 Å; Figure 3.5, blue *versus* purple).

3.3 Fluorescence decays of FADox in BsFNR variants

As reported in the previous work, the steady-state fluorescence intensity of the protein-bound FAD_{ox} in Y50G *Bs*FNR is six to seven times as high as that of free FAD_{ox}, while in WT and Y50W *Bs*FNR mutant fluorescence intensities decrease to <3% and 9%, respectively, of that of free FAD_{ox} (Figure 3.3).[33] These observations are fully consistent with the results of time-resolved fluorescence in our study (Figure 3.6). The fluorescence decay of excited FAD_{ox} (FAD_{ox}^{*}) in WT and Y50W *Bs*FNR is dominated (>80%) by very fast phases, fitted with time constants of 260 fs and 210 fs respectively. For WT a minor phase with a time constant of 2.6 ps is also observed. In Y50W *Bs*FNR, the fluorescence decay is more multiphasic, with additional time constants of 5.2 ps, and 1.2 ns. On the other hand, in Y50G *Bs*FNR where a close-lying redox-active aromatic residue is absent, an overall much slower bi-exponential decay was detected, with time constants of 300 ps and 4.4 ns (dominant phase). These findings clearly show that Tyr50 and Trp50 in WT *Bs*FNR and the Y50W mutant are the main electron donors to FAD_{ox}^{*} and lead to efficient fluorescence quenching. The observed multiphasic fluorescence decay with a long-lived component in Y50W *Bs*FNR is generally consistent with our MD simulations, where we observed substantial conformational heterogeneity of the Trp50–FAD_{ox} pair. As is the general case in flavoenzymes, the coexistence of multiple configurations of flavin-electron donor pairs results in a multiphasic fluorescence decay. In particular, in those Y50W *Bs*FNR proteins where the Trp50 is distant from FAD, the fluorescence quenching is expected to be much less efficient.

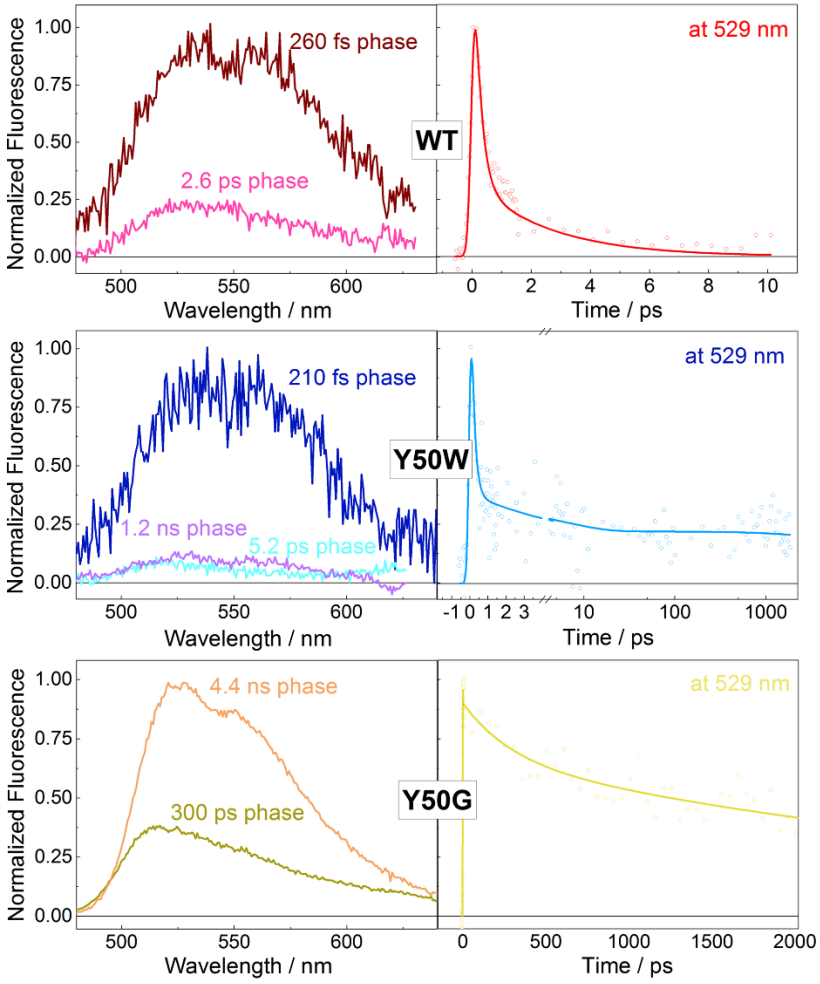

Figure 3.6 Decay associated spectra (DAS) from the global analysis of fluorescence decays (*left*) and kinetic traces at 529 nm (*right*) of WT, Y50W (on linear-logarithmic timescale) and Y50G *Bs*FNR.

Furthermore, in the case of Y50G *Bs*FNR, the 300 ps phase that accounts for ~30% of the fluorescence decay is still faster than expected for nonquenched unstacked FAD_{ox} (a few nanoseconds, as observed in the dominant longer phase), suggesting the existence of less efficient yet active electron donors located further away (candidates include Tyr25 and Tyr56).

3.4 Transient absorption measurements and analysis of photoproducts

As fluorescence decays only provide information on excited state kinetics, to characterize the transient species during the photoinduced process of FAD_{ox} in *Bs*FNR, we performed transient absorption spectroscopic measurements. Figure 3.7 shows the isotropic transient absorption spectra of *Bs*FNR in WT, Y50W and Y50G variants recorded 3 ps after excitation, and Figure 3.8 shows the kinetic traces at selected wavelengths. In the transient spectra, the negative bands around 450 nm are dominated by ground state bleaching (GSB, cf. Figure. 3.10 below). The spectrum of Y50G *Bs*FNR contains an additional negative band

around 560 nm that is assigned to the stimulated emission (SE), as well as induced absorption features below 420 nm, around 525 nm and beyond 625 nm that are assigned to the absorption of FAD_{ox}^{*}. The shape of these features remains fairly unchanged up to the nanosecond timescales, indicating the persistence of a long-lived FAD_{ox}^{*} population, in agreement with the time-resolved fluorescence experiments (Figure 3.6).

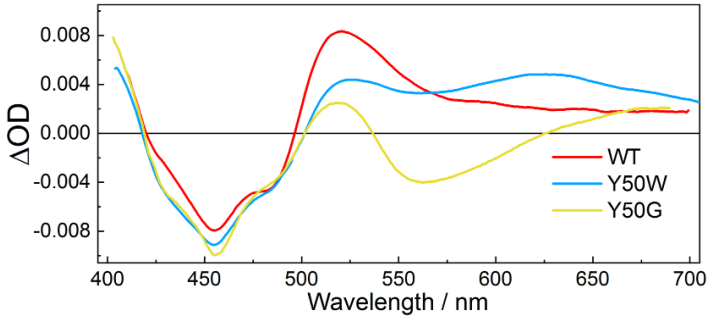

Figure 3.7 Isotropic transient absorption spectra of *Bs*FNR variants measured at 3 ps after excitation.

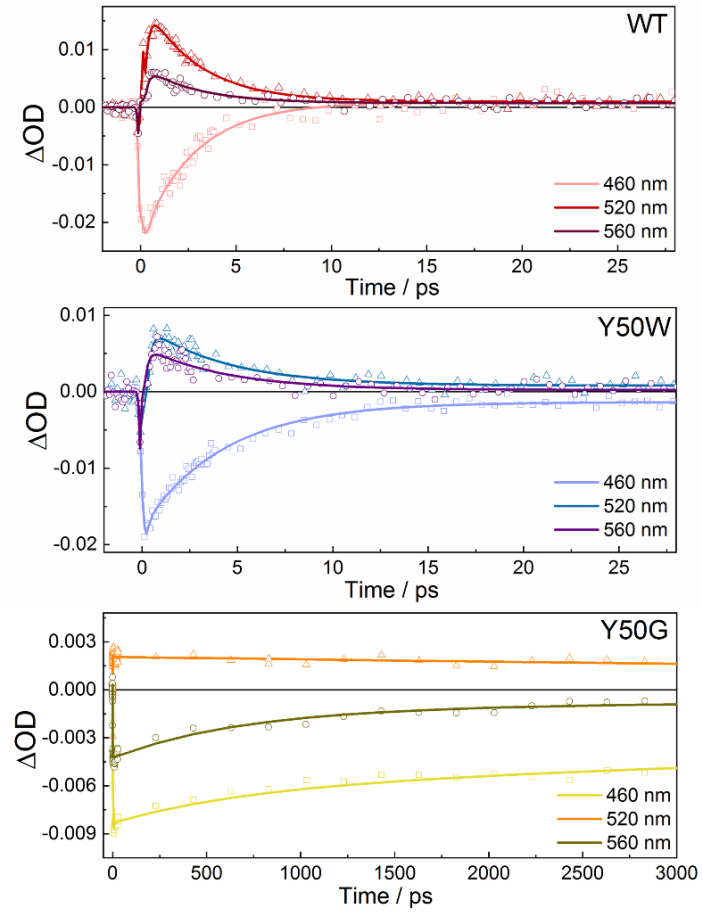

Figure 3.8 Kinetic traces in the transient absorption measurements of WT, Y50W and Y50G *Bs*FNR at selected wavelengths.

In contrast to Y50G *Bs*FNR, in the 3 ps spectra of WT and Y50W *Bs*FNR the SE signal does not clearly appear, whereas distinct positive signals beyond 500 nm are observed. This indicates that in these systems the dominant FAD_{ox}^{*} decay on the femtosecond timescale leads to new photoproducts, which can be attributed to ET from different nearby electron donors.

Multi-exponential global analysis of these transient absorption data was performed. The resulting EAS are given in Figure 3.9. Reference spectra of intermediate species that are generally involved in the photochemistry of flavoproteins are summarized in Figure 3.10.

The transient absorption data of WT *Bs*FNR were fitted by two kinetic phases, with time constants of 240 fs and 2.9 ps, and a long-lived phase. The 240-fs phase, required to obtain a satisfactory fit, has a similar time constant as the dominant fluorescence decay phase (260 fs) and can be assigned to FAD_{ox}^{*} decay. The time constant is close to the instrument response function; therefore, the corresponding EAS shows strong modulations due to cross-phase modulation artefacts during pump-probe temporal overlap. As mentioned above the 2.9-ps phase EAS (Figure 3.9, *top* panel) predominately reflects decay of a product state, with only a modest contribution expected from the excited state (~14%, estimated from the fluorescence decays). As Tyr50 is the electron donor responsible for quenching FAD_{ox}^{*}, the product state should be the $FAD^{\bullet-}$/$TyrOH^{\bullet+}$ ion pair or derivatives thereof. $TyrOH^{\bullet+}$ may in principle become deprotonated concertedly with its formation to yield $TyrO^{\bullet}$. The only nearby candidate proton acceptor is the flavin with which Tyr50 closely interacts; it is H-bonded to the O2´ hydroxyl group of the ribityl moiety of FAD. Yet, the EAS does not show the characteristic absorption band of $FADH^{\bullet}$ between 600 and 700 nm. We infer that the photoproducts in the 2.9-ps phase EAS are $FAD^{\bullet-}$ and the tyrosyl cation radical $TyrOH^{\bullet+}$. We note that the induced absorption band centered at ~520 nm that may include contributions from both species, extends more to the longer wavelengths than the spectral features of $FAD^{\bullet-}$ in GOX Figure 3.10. It is also qualitatively similar, but more red-extended in the induced absorption part, to the transient spectrum assigned to the $FAD^{\bullet-}$/$TyrOH^{\bullet+}$ ion pair in a TrmFO variant.[98] This issue will be addressed in the following section. Finally, the remaining long-lived phase is too small (<1% of the initial signal in the bleaching area) to be reliably analyzed.

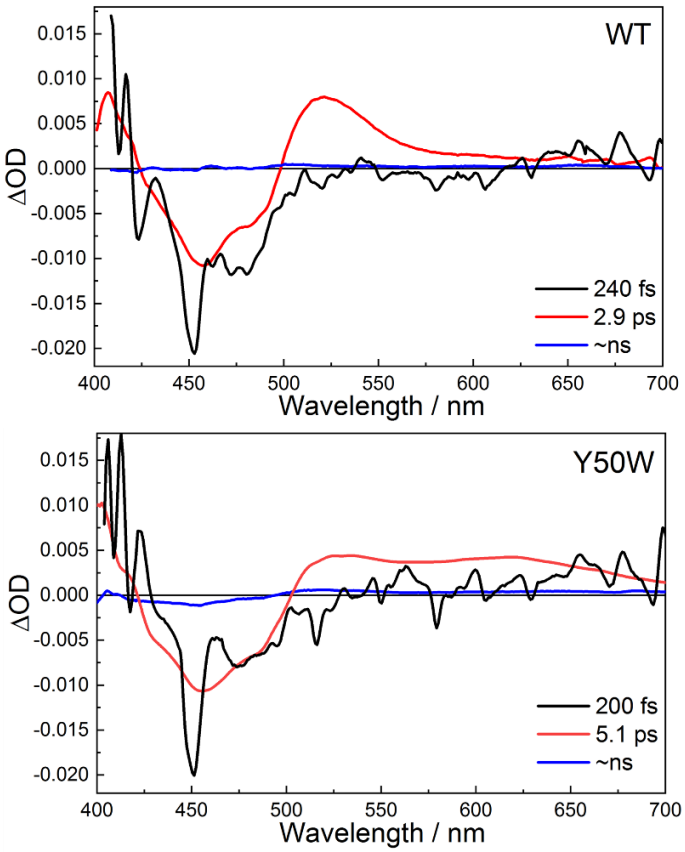

Figure 3.9 EAS of the intermediates obtained from global analysis of transient absorption data of WT (*top*) and Y50W (*bottom*) *Bs*FNR. The modulations in the femtosecond phases are due to cross phase modulation artifacts during pump-probe overlap.

For Y50W *Bs*FNR, two kinetic phases with time constants of 200 fs, 5.1 ps, and a long-lived phase are required to fit the transient absorption data. The 200-fs phase, similar to WT *Bs*FNR, despite the cross-phase modulation artefacts, represents the dominant initial excited state decay due to ultrafast ET, consistent with the fluorescence decay. Similar to the 2.9-ps phase of WT *Bs*FNR, the 5.1-ps phase in the Y50W mutant is clearly dominated by product state contributions. The broad induced absorption in the red part of the spectrum (Figure 3.9, *bottom* panel) is in general agreement with $TrpH^{\bullet+}$ formation, but also may reflect $FADH^{\bullet}$ formation (Figure 3.10). Thus, at first view, both ET (with product state of $FAD^{\bullet-}/TrpH^{\bullet+}$ ion pair) and concerted proton-electron transfer (CPET, with product state $FADH^{\bullet}/Trp^{\bullet}$ radical pair) are possible. Yet, given the higher pK_a of $TrpH^{\bullet+}$ than $TyrOH^{\bullet+}$ and the modeled more distant interaction of Trp50 than Tyr50 with the flavin ring (Figure 3.5), CPET appears (even) less likely to occur on the sub-picosecond timescale than $FADH^{\bullet}/TyrO^{\bullet}$ formation in WT *Bs*FNR.

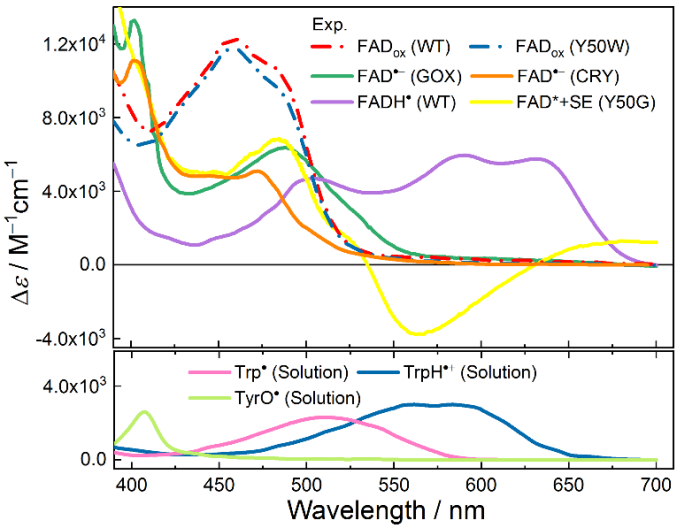

Figure 3.10 Reference absorption spectra of flavin (*top*) and aromatic amino acid (*bottom*) intermediate species usually involved in the photoinduced processes of protein-bound oxidized flavins. Steady-state spectra of $FAD^{\bullet-}$ in GOX,[5] $TyrO^{\bullet}$, $Trp^{\bullet}$, $TrpH^{\bullet+}$ in solution,[101–103] as well as $FADH^{\bullet}$ in WT *Bs*FNR,[104] are taken or derived from published data. The spectrum of FAD_{ox}^{*} absorption and the corresponding SE band are extracted from the transient absorption spectrum of Y50G *Bs*FNR. The $S_0 \rightarrow S_1$ transition bands of ground-state FAD_{ox} in WT *Bs*FNR and the Y50W mutant are also shown for comparison.

We further investigated this issue by a detailed spectral analysis (Figure 3.11). By assuming an ET reaction and taking into account partial contributions from FAD_{ox}^{*} absorption and SE, the 5.1-phase EAS can be represented according to Eq 3.1:

$$EAS_{5.1ps}^{(ET,Y50W)} = [\Phi_1(\varepsilon_{FAD^{\bullet-}} + \varepsilon_{TrpH^{\bullet+}}) + \Phi_2 \Delta\varepsilon_{FAD^*/SE} - (\Phi_1 + \Phi_2)\varepsilon_{FAD_{ox}^{Y50W}}]c_0 L \qquad (3.1)$$

Likewise, by assuming a CPET reaction, the EAS can be represented as:

$$EAS_{5.1ps}^{(CPET,Y50W)} = [\Phi_1(\varepsilon_{FADH^{\bullet}} + \varepsilon_{Trp^{\bullet+}}) + \Phi_2\varepsilon_{FAD^*/SE} - (\Phi_1 + \Phi_2)\varepsilon_{FAD_{ox}^{Y50W}}]c_0 L \qquad (3.2)$$

where c_0 is the initial concentration of FAD_{ox}^{*} after the excitation at 390 nm, ε_i are the molar extinction coefficient of species i, Φ_1 is the quantum yield of the initial ET or CPET reaction, Φ_2 is the molar ratio of FAD_{ox}^{*} that decays with a lifetime similar to the charge recombination (*vide supra*), L is the optical path, and $\Delta\varepsilon_{FAD*/SE}$ gives the differential molar extinction coefficient with both the contributions from the FAD_{ox}^{*} and SE. Here, c_0 is determined using an actinometric reference $[Ru(bpy)_3]Cl_2$, and Φ_1, Φ_2 are inferred from the time-resolved fluorescence analysis (determined form the relative amplitudes of the DAS in Figure 3.6) to be 0.80 and 0.09, respectively. $\Delta\varepsilon_{FAD*/SE}$ is extracted from the transient absorption spectrum of

Y50G *Bs*FNR, published results of molar extinction coefficients of $TrpH^{\bullet+}$ and $Trp^{\bullet}$ in solution, as well as $FAD^{\bullet-}$ in GOX were used to represent corresponding species (Figure 3.10). With all parameters and spectra on the right-hand side of the equations determined, we are able to construct quantitative model spectra.

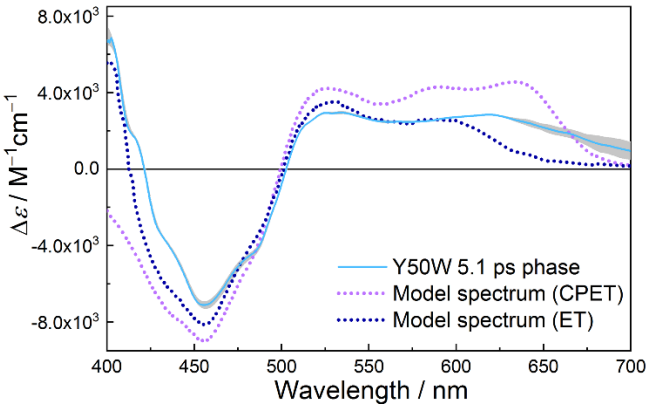

Figure 3.11 Spectral analysis of the 5.1-ps phase EAS of Y50W *Bs*FNR. Model spectra with ET and CPET pathways were constructed according to Eq 3.1 and Eq 3.2. The estimated confidence interval is shaded in grey.

Scheme 3.1 Proposed simplified reaction scheme of the photoreduction processes of FADox in WT BsFNR (red) and the Y50W variant (blue, in parentheses).

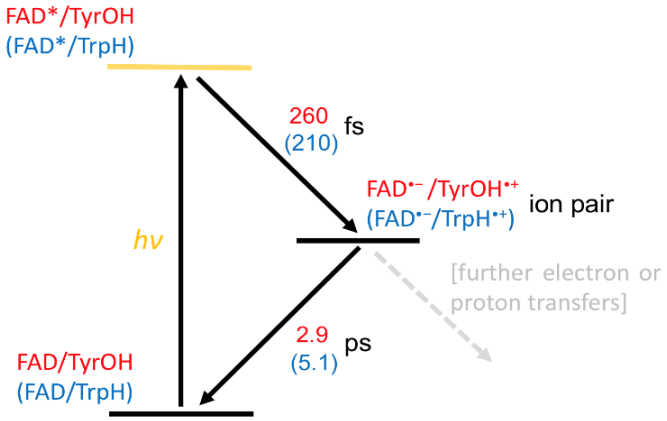

As illustrated in Figure 3.11, modeling the 5.1-ps phase EAS with contributions from $Trp^{\bullet}$ and $FADH^{\bullet}$ cannot explain the strong positive absorption around 410 nm, and the experimental feature around 625 nm does not match that in the model. In contrast, assuming that only ET occurs in this ultrafast timescale, the model spectrum with photoproducts of $TrpH^{\bullet+}$ and $FAD^{\bullet-}$ reproduces the GSB, and induced absorptions at around 410 nm and up to 600 nm in the EAS, rather satisfactorily. However, a bathochromic shift (red-shift) or spectral broadening to longer wavelength is required to account for the absorption band that extend beyond 650 nm. As indicated in the Discussion section below, such shifts in the $TrpH^{\bullet+}$

absorption spectrum have been invoked before in other systems. Therefore, the photoproducts that appear in the 5.1 phase can be reasonably assigned to recombination of a $FAD^{\bullet-}$/$TrpH^{\bullet+}$ ion pair. The origin of the $TrpH^{\bullet+}$ shift will be further addressed below. Finally, a small but significant long-lived phase is observed. This phase likely contains contributions from the fraction of the protein with long-lived fluorescence, where Trp50 lies relatively far away from FAD and cannot donate electrons efficiently. although more long-lived product states clearly also contribute to this phase. No attempt was made to further model this small phase.

3.5 QM/MM spectral calculations

The reaction scheme of the light-induced processes of WT and Y50W *Bs*FNR is summarized in Scheme 3.1. As indicated above, the products of the initial ET step can be unambiguously identified as charged radical pairs. However, the spectral properties have altered line shapes with respect to the reference spectra from other proteins or from solution. Moreover, even between WT and Y50W *Bs*FNR, $FAD^{\bullet-}$ appears to have different spectral features (Figure 3.9, around absorption bands at ~400 and 520 nm), although this observation is complicated by different contributions from the amino acid radicals. In order to provide an interpretation framework of their spectral properties and explore the major effects that may lead to the spectral changes, we employed a QM/MM protocol to calculate the absorption spectra of $FAD^{\bullet-}$, $TyrOH^{\bullet+}$ and $TrpH^{\bullet+}$ in WT and Y50W *Bs*FNR (Figure 3.12). Despite some overestimations of the transition energies and oscillator strengths, the calculated spectra of $TrpH^{\bullet+}$ and $FAD^{\bullet-}$ qualitatively agree well with our experimental observations, and also provide a prediction of the $TyrOH^{\bullet+}$ absorption band. The discrepancies between the experimental and predicted spectra probably arise from the limitation of TDDFT when it is applied to open-shell systems.[105] The above-mentioned apparent differences in $FAD^{\bullet-}$ absorption bands between WT and Y50W *Bs*FNR (namely the relative amplitudes of the two absorption maxima) appear reproduced in the simulations; in addition, substantial extension of the $FAD^{\bullet-}$ absorption in the red tail is predicted for both variants; these findings are subject to further assessments (*vide infra*).

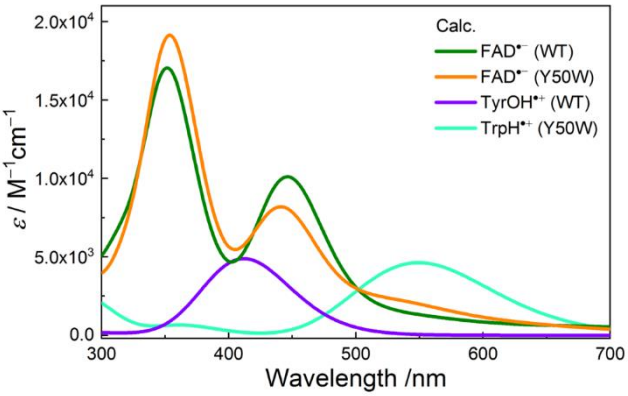

Figure 3.12 Calculated absorption spectra of individual radical intermediates involved in the photoreduction processes of FAD_{ox} in WT *Bs*FNR and the Y50W mutant.

We used the simulated spectra shown in Figure 3.12 to construct the absorption spectra of the radical product states by superimposing individual spectra of corresponding components. These spectra are compared in Figure 3.13 with those deduced from the experimental EAS phases after removing the contributions from GSB, induced absorption of FAD_{ox}^{*} and SE. Taking into account the abovementioned general limitation of TDDFT, our simulations faithfully reproduce the shape of the spectral features of $FAD^{\bullet-}$/$TyrOH^{\bullet+}$ and $FAD^{\bullet-}$/$TrpH^{\bullet+}$ ion pairs, thus supporting our interpretations of the respective recombination phases in WT and Y50W *Bs*FNR.

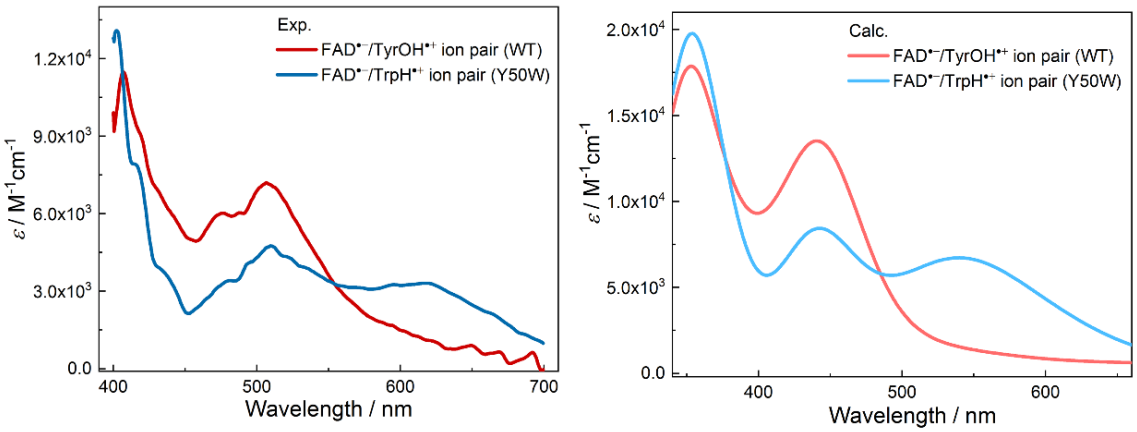

Figure 3.13 Experimentally determined absorption spectra (*left*) and calculated absorption spectra (*right*) of the $FAD^{\bullet-}$/$TyrOH^{\bullet+}$ and $FAD^{\bullet-}$/$TrpH^{\bullet+}$ ion pairs in *Bs*FNR.

The substantial variation in $FAD^{\bullet-}$ spectra (Figure 3.10 and 3.12) and shifts observed in the $TrpH^{\bullet+}$ spectrum with respect to the solution spectrum (Figure 3.11), imply that the local environment can have a significant impact on the spectral properties of the radical intermediates. In WT and Y50W *Bs*FNR, the active-site structures are presumably very much alike except for the presence of different counter-ions; the interactions between $FAD^{\bullet-}$ and

$TyrOH^{\bullet+}$ or $TrpH^{\bullet+}$ thus should be of importance. As molecular absorption in the visible and near-infrared ranges are usually associated with electrons that occupy the frontier molecular orbitals (FMO), we visualized the FMO of $FAD^{\bullet-}$ in vacuum and in *Bs*FNR protein environments. As illustrated in Figure 3.14, in the protein environments, the LUMO(α) of $FAD^{\bullet-}$ are significantly deformed compared with that in vacuum, which are mostly located beyond the molecular plane of the isoalloxazine ring and extend toward the counter-ions. This result implies that electronic transitions of $FAD^{\bullet-}$ that involve this molecular orbital will exhibit strong charge-transfer characteristics. It also worth noting that they are shaped differently in WT *Bs*FNR and the Y50W mutant, which can reasonably explain the differences in $FAD^{\bullet-}$ spectra between these two variants.

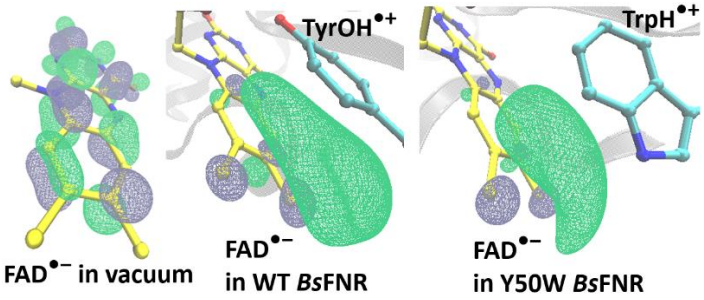

Figure 3.14 Calculated LUMO(α) (isovalue: 0.036) of FAD•− in vacuum, in WT BsFNR and in the Y50W mutant in the presence of the corresponding counter-ions. The geometry of FAD•− was energetically optimized at the QM level of theory (UB3LYP/6-311G*). Hydrogens are not shown for clarity.

To explicitly address the influence of the counter-ions, we calculated spectra of FAD, tyrosine, and tryptophan in the radical anionic or cationic state with a unit probe point charge (e^+ for $FAD^{\bullet-}$, e^- for $TyrOH^{\bullet+}$ and $TrpH^{\bullet+}$) placed near the aromatic rings. An implicit solvent model with a dielectric constant ε = 20 was used to simulate the screening effect of the protein/solvent environment. This approach significantly reduces the complexity of the systems, but is representative enough to simulate the presence of counter-ions in a well-defined environment. As illustrated in Figure 3.15, the absorption spectra of $FAD^{\bullet-}$ are highly sensitive to the presence of the external positive point charge: when the distance between $FAD^{\bullet-}$ and the point charge reaches 5 Å, the absorption bands of $FAD^{\bullet-}$ start to change; with the decrease of the distance, the low-energy band increases its amplitude and red-shifts, while the high-energy band originally goes through a more complicated deformation, exhibiting an overall decrease of amplitude. These effects are in agreement with the main results of the spectral calculations in the complex explicit protein/solvent environment shown in Figure 3.12. They are

approximately as expected from the spectral differences of $FAD^{\bullet-}$ between WT and Y50W *Bs*FNR, as in WT *Bs*FNR Tyr50 is located closer to FAD than Trp50 in the Y50W mutant.

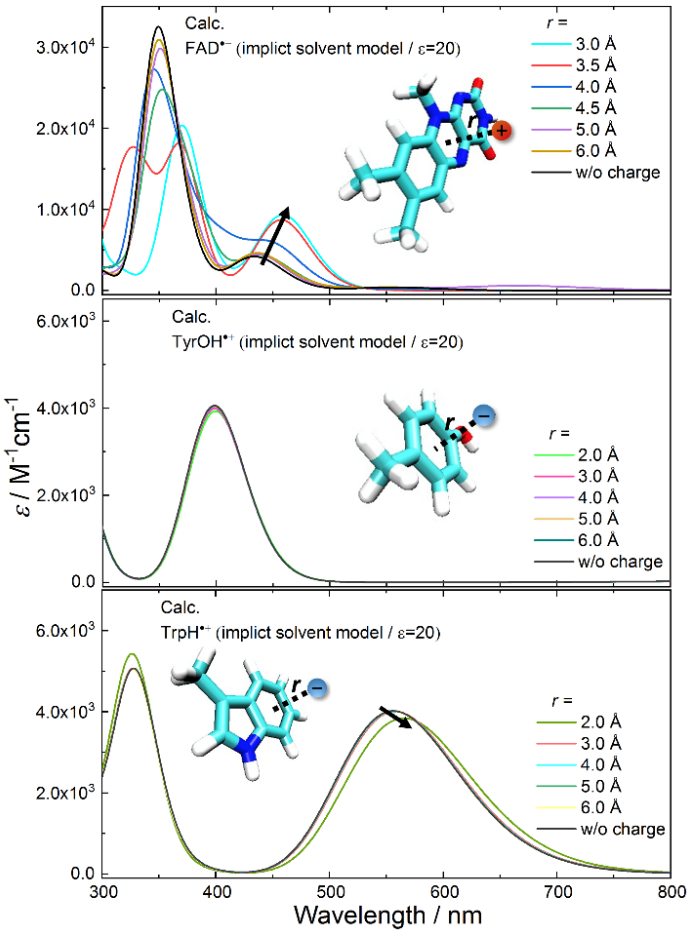

Figure 3.15 Distance-dependent effects of a unit point charge on the absorption spectra of $FAD^{\bullet-}$, $TyrOH^{\bullet+}$ and $TrpH^{\bullet+}$. Structures of model compounds and the position of the probe charge (red: e^+, blue: e^-; above the geometric ring centers) are indicated in the insets.

On the other hand, noticeable changes in the calculated $TyrOH^{\bullet+}$ and $TrpH^{\bullet+}$ absorption spectra are only obtained when the negative point charge is placed as close as 2 Å. The contrasting behavior in $FAD^{\bullet-}$ *versus* $TyrOH^{\bullet+}$ and $TrpH^{\bullet+}$ could have two causes. First, a positive charge is likely to act as a virtual nucleus to attract electrons, strengthening the charge-transfer characteristics of the electronic transitions, and consequently leading to spectral deformations. Second, flavin has a larger and more complex π-conjugated system than tyrosine and tryptophan; in the radical anionic state, the unpaired electron tends to occupy molecular orbitals with higher energy than the unpaired electron in radical cationic molecules, and thus more inclined to be affected by the surrounding environment. Indeed, our DFT calculations confirm that $FAD^{\bullet-}$ has a much higher HOMO(α) (which corresponds to singly unoccupied molecular orbitals) energy than $TyrOH^{\bullet+}$ and $TrpH^{\bullet+}$ (–5.59, –12.49 and –11.21 eV in vacuum

for $FAD^{\bullet-}$, $TyrOH^{\bullet+}$ and $TrpH^{\bullet+}$ respectively); the trend is also in agreement with the observation that the spectrum of $TyrOH^{\bullet+}$ is even more "inert" to the approach of the external charge than that of $TrpH^{\bullet+}$.

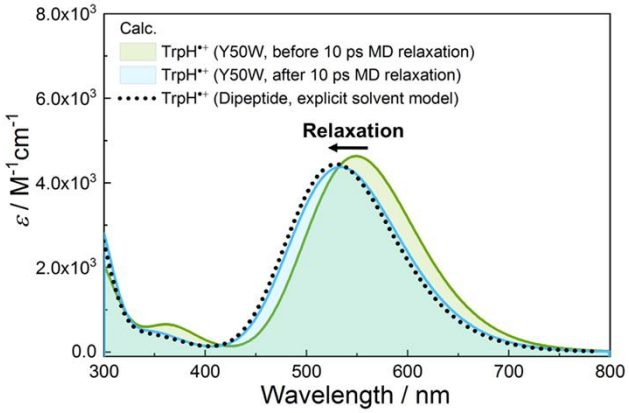

Figure 3.16 Calculated spectral charges of $TrpH^{\bullet+}$ following the relaxation process after the initial ET (averaged over 50 snapshots). As a reference, the calculated $TrpH^{\bullet+}$ absorption spectrum in solution (explicit solvent model, structures of dipeptide for spectral calculations were taken from MD simulations with radical cationic geometry; the calculated spectrum corresponds to the average over 100 snapshots) is shown as the dotted line.

In WT *Bs*FNR the contributions of both constituents of the $FAD^{\bullet-}$/$TyrOH^{\bullet+}$ product states appear to overlap. For the Y50W mutant, the $TrpH^{\bullet+}$ product absorbs more to longer wavelengths, which allows us to individually analyze its spectral properties by further comparing experimental and simulation results. The spectrum calculated for $TrpH^{\bullet+}$ in Y50W *Bs*FNR (Figure 3.12) at first glance appears similar to that of $TrpH^{\bullet+}$ in solution (Figure 3.15). This could arise from the fact that in Y50W *Bs*FNR, Trp50 is located on the surface of the protein and exposed to the solvent. As demonstrated above charged species nearby have a moderate influence on the spectrum of $TrpH^{\bullet+}$ in a solvent-exposed protein environment. In Y50W *Bs*FNR the ring-to-ring distance is always larger than 3 Å (Figure 3.4), the influence of $FAD^{\bullet-}$ and surrounding residues on the absorption spectrum of $TrpH^{\bullet+}$ should be rather small. This suggestion seems to be at odds with the comparison of the transient experimental spectrum with the quasi-continuous reference spectrum of $TrpH^{\bullet+}$ in aqueous solution, obtained by pulse radiolysis, that are substantially shifted. We note that in our transient absorption measurement $TrpH^{\bullet+}$ decays in a few picoseconds upon formation, whereas the literature reference corresponds to equilibrated configurations. Experimentally, flavin spectral relaxations following photoexcitation on the picosecond timescale have been reported.[34,106] We therefore investigated whether configurational relaxations in the protein active site may influence the spectral properties of $TrpH^{\bullet+}$. To this end, we performed 10 ps MD simulations in the charge-

separated state of Y50W *Bs*FNR starting from a neutral state molecular geometry. TDDFT calculations were carried out for $TrpH^{\bullet+}$ with the structures before and after the structural relaxation. Figure 3.16 clearly demonstrates that in Y50W *Bs*FNR, after the relaxation, the $D_0 \rightarrow D_2$ transition band of $TrpH^{\bullet+}$ shifts to shorter wavelengths, accompanied by a slight decrease in amplitude. Hence, during relaxation the positive charge of $TrpH^{\bullet+}$ induces polarization in the surrounding protein/solvent environment that stabilizes its positive charge. This induced polarization also destabilizes the LUMO, where the electron is closer to the negative charge induced in the environment, relative to the HOMO, and thus shifts the $D_0 \rightarrow D_2$ transition band to shorter wavelengths. Furthermore, as expected, the spectrum obtained after relaxation is similar to that calculated for the free radical ion in solution. These results qualitatively agree with our experimental observations. Within this interpretation, the apparent red-shift and line shape broadening of the $D_0 \rightarrow D_2$ transition band of $TrpH^{\bullet+}$ are most likely due to a combined effect of unrelaxed geometry (major) and the presence of the counter-ion $FAD^{\bullet-}$ (minor).

3.6 Concluding remarks

Using ultrafast spectroscopies to study the photoproducts of WT and Y50W *Bs*FNR and comparison with that of the Y50G variant has enabled us to unambiguously identify the involved electron-donating residues in the former two cases. In both WT and Y50W *Bs*FNR, the significant separation of timescales of the dominant excited state decay and product decay allowed to determine and characterize the transient spectrum of the initial photoproduct. In WT, It is similar to that reported for TrmFO,[97,98] with $TyrOH^{\bullet+}$ absorption strongly contributing to the observed EAS of the product state, confirming that in a confined protein environment without suitable proton acceptors and on an ultrafast timescale, despite its extremely high acidity, $TyrOH^{\bullet+}$ can be formed as a distinct species without concomitant deprotonation. In WT and Y50W *Bs*FNR, the charge-separated product states both decay mainly by charge recombination in a few picoseconds (WT: 0.3 ps^{-1}; Y50W: 0.2 ps^{-1}), similarly as in other flavoproteins with nearby aromatic residues.[8,12,13,98] Qualitatively, the somewhat higher rate of the back ET in WT *Bs*FNR may be related to the shorter average donor-acceptor distance (Figure 3.4), and the larger driving force due to the higher redox potential of tyrosine in proteins.[31]

The spectral properties of radical intermediates that deviate from model spectra were further investigated from a theoretical standpoint. We demonstrate that the spectral properties of $FAD^{\bullet-}$ are highly sensitive to protein environments. Therefore, applying model spectra of

$FAD^{\bullet-}$ from different flavoproteins (or even different variants of the same protein) for spectral analysis should be handled with caution. For the Y50W mutant, the $TrpH^{\bullet+}$ spectrum was found to extend more to longer wavelengths than the model spectrum obtained on the microsecond timescale in aqueous solution that is extensively used in the literature. Nevertheless, our simulations based on relaxed geometries suggest that, with Trp50 being exposed to the solvent in Y50W *Bs*FNR, the $TrpH^{\bullet+}$ spectrum should be quasi-indistinguishable from the solution spectrum. Our further simulations suggest that this discrepancy may be related to the fact that the structure is not fully relaxed on the timescale of the lifetime of the charge-separated state of a few picoseconds. This assessment is in general agreement with experimental evidence that charge relaxations influencing electronic spectra occur on this timescale, including in flavoproteins.[34,106] Altogether, our results may help to understand similar features in a range of flavoprotein systems.

Chapter 4. Ultrafast Photooxidation of Protein-Bound Anionic Flavin Radicals

4.1 Stabilization of anionic flavin radicals in flavoprotein oxidases

In contrast to oxidized flavin, how the anionic semi-reduced flavin radical behaves upon excitation remains essentially unknown despite their relevance as functional intermediates in many flavoproteins. For instance, in blue-light receptor proteins such as cryptochromes and BLUF domain proteins, the photoreduction of oxidized flavin to the anionic radical form represents the first essential step in their response to light.[107,108] In FAP, the photoinduced ET between FAD_{ox} and the fatty acid substrate leads to $FAD^{\bullet-}$ as an intermediate.[29] Light-independent processes can also occur through pathways involving anionic flavin radical formation. This is for instance the case for the oxidative catalysis of organic molecules by nitronate monooxygenase (NMO)[109] and by GOX, which is widely used in biotechnology applications.[110,111] Yet, despite decennia of in-depth flavoprotein research, so far only a few flavoproteins have been reported to be able to stabilize the anionic flavin radical in the steady state.[5,7,23,24,107,112,113] Due to their intrinsically unstable nature, understanding of photophysical properties of anionic flavin radicals is very limited.

The majority of flavoproteins that can stabilize anionic flavin radicals are oxidases. This may be corelated with their physiological functions that involve the stabilization of electron-rich intermediates in the active sites. This chapter describes an investigation of the excited-state deactivation pathway of protein-bound anionic flavin radicals. In particular, using ultrafast spectroscopy with full-spectral resolutions, we studied a set of flavoprotein oxidases, where the anionic flavin radicals can be stabilized and that have well-characterized crystal structures available, i.e., $FAD^{\bullet-}$ in GOX, COX, MSOX and DAAO, as well as $FMN^{\bullet-}$ in NMO. In all these systems, the active site contains positively charged residues that are thought to be required for stabilizing the superoxide $O_2^{\bullet-}$ functional reaction intermediate ("oxygen activation"),[114,115] and these residues are also close to van der Waals contact with the isoalloxazine ring system (Figure 4.1).

Anionic flavin radicals are usually short-lived reaction intermediates, and in aqueous solution their formation and detection requires pulse radiolysis methods.[116] In some flavoproteins anionic flavin radicals can be stably produced under anaerobic conditions by blue-light illumination in the presence of a hole scavenger or chemical reduction.

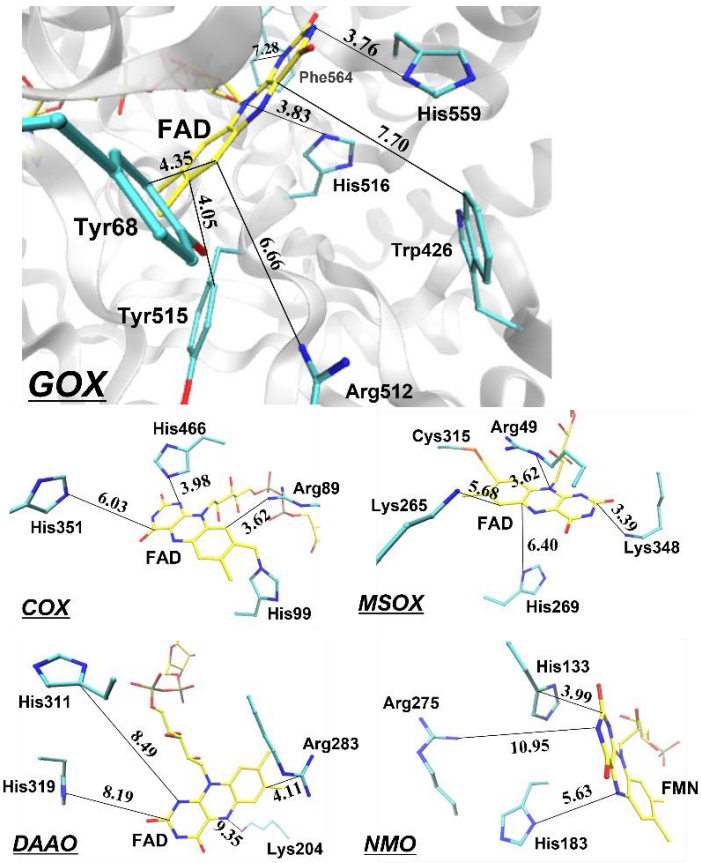

Figure 4.1 Active sites in the crystal structures of GOX from *Aspergillus niger* (PDB entry: 1CF3), COX from *Arthrobacter globiformis* (S101A variant; PDB entry: 3NNE), MSOX from *Bacillus sp.* (PDB entry: 2GB0), DAAO from porcine kidney (PDB entry: 1VE9; in complex with benzoate [not shown]), and NMO from *P. aeruginosa* PAO1 (PDB entry: 4Q4K). The carbon atoms of the flavin cofactors are shown in yellow, whereas those of selected active-site residues are displayed in cyan; nitrogen, oxygen and sulfur atoms are colored in blue, red and orange, respectively. The closest distances between flavin rings and non-hydrogen atoms of side chains are shown in Å.

Figure 4.2 shows the absorption spectra of protein-bound anionic flavin radicals produced and stabilized in GOX, COX, MSOX, DAAO and NMO. In the visible range, anionic flavin radicals exhibit two distinct transition bands. Those obtained in proteins differ significantly from those produced in solution by pulse radiolysis and from each other. This can be explained by the interactions between the anionic flavin radicals and the local protein environments, and might be an indication of positive charges close-by, as has been demonstrated in **Chapter 3**. Furthermore, we note that the presence of small amounts of

oxidized or fully reduced flavin in the equilibrated samples cannot be fully excluded, as an exchange mechanism between fully reduced free flavins and protein-bound oxidized flavins has been proposed to explain the production of anionic flavin radicals in flavoproteins via photoreduction.[117]

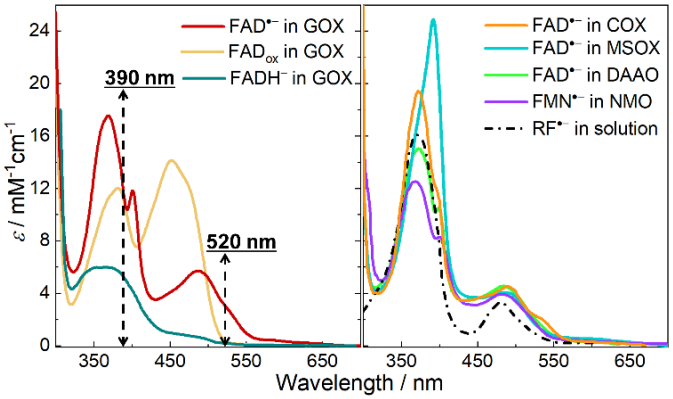

Figure 4.2 Steady-state absorption spectra of flavin species in GOX (*left*) and anionic flavin radicals in different systems (*right*). $FAD^{\bullet-}$ in GOX was generated by photoreduction in the presence of EDTA at pH 10.1, and the spectrum of FAD_{ox} in GOX was measured at pH 10.1. Spectra of $FAD^{\bullet-}$ in DAAO and semi-reduced riboflavin ($RF^{\bullet-}$) in aqueous solution were reproduced from published data.[5,116] The other spectra were measured as described in **Chapter 2**. For all the spectra, the reported values of extinction coefficients were used.[5,7,24,113,116] Dashed lines indicate the maxima of excitation pulses in the time-resolved spectroscopic measurements.

4.2 Emission from excited anionic flavin radicals

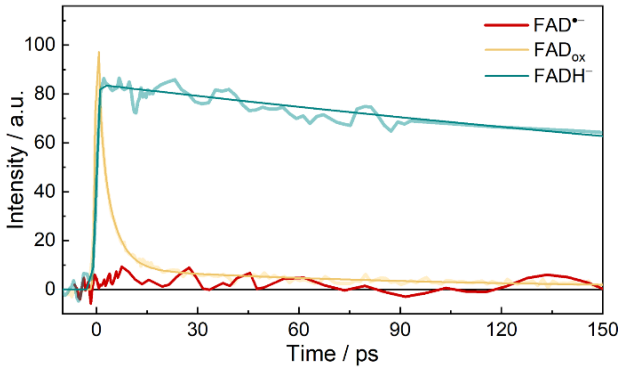

Figure 4.3 Fluorescence decays of $FAD^{\bullet-}$, FAD_{ox}, and $FADH^{-}$ in GOX monitored at 537 nm under the same excitation conditions with CS_2 as the Kerr medium. Intensities were normalized based on the absorption of the samples at the excitation wavelength (390 nm). Exponential fits are shown as smooth curves.

To elucidate excited-state dynamics, first we investigated the excited state dynamics of $FAD^{\bullet-}$ using time-resolved fluorescence measurements. As shown in Figure 4.3, we did not detect any perceptible emission signal upon excitation at 390 nm for $FAD^{\bullet-}$ in GOX with our setup that has femtosecond time-resolution (for samples both obtained by photo- and chemical reductions). The fluorescence decays of FAD_{ox} and $FADH^{-}$ in GOX measured under the same

experimental conditions are presented in the same figure for comparison. The fluorescence of FAD_{ox} in GOX mainly decays with time-constants of 1.1 ps and 4.3 ps.[12,32] The time-resolved fluorescence of $FADH^-$ in GOX exhibits a monophasic decay with a time constant of 800 ps. The absence of an emission signal for $FAD^{\bullet-}$ in GOX indicates that there are nonradiative processes taking place much faster than the system response (~ 200 fs with suprasil as a Kerr medium).

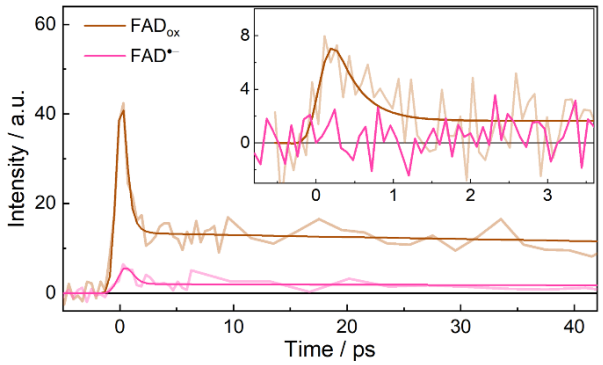

Figure 4.4 Fluorescence decays of the as-prepared aerobic (FAD_{ox}) and reduced ($FAD^{\bullet-}$) samples of COX monitored at 532 nm, with benzene or suprasil (inset) as the Kerr medium. Measurements were conducted with the same sample before and after the chemical reduction (see text). Exponential fits are shown as smooth curves.

$FAD^{\bullet-}$ in COX is stable even in the presence of O_2,[24] allowing long-duration signal accumulation for detecting small signals. As a reference, the time-resolved fluorescence of the non-reduced, FAD_{ox}-containing sample in COX was first measured (Figure 4.4). Upon excitation at 390 nm, it exhibits a biphasic decay with a dominant ~300-fs ultrafast phase and a long-lived phase (Figure 4.5). The 300-fs phase was assigned to FAD_{ox} fluorescence, quenched by flavin photoreduction processes. The sample was then incubated with $Na_2S_2O_4$ until the reaction reached maximal $FAD^{\bullet-}$ formation (corresponding to the absorption spectrum shown in Figure 4.2), and further time-resolved fluorescence measurements were performed. With benzene as the Kerr medium (relatively high sensitivity but low time-resolution), a small signal less than 10% of that of FAD_{ox} was detected, which has similar kinetic and spectral (maximum at ~520 nm) features (Figure 4.3 and 4.4) as those of FAD_{ox} and was therefore assigned to a remaining fraction of FAD_{ox}. On the other hand, when suprasil was used as the Kerr medium (low sensitivity but high time-resolution), no perceptible emission signal was detected for the reduced sample, whereas the ~300 fs phase of FAD_{ox} is clearly resolved in the non-reduced sample (inset, Figure 4.3). From the comparison of the signals of the reduced and non-reduced samples we estimate that any $FAD^{\bullet-}$ fluorescence decays in < 30 fs. Altogether,

we conclude that as in GOX, in COX ultrafast nonradiative deactivation of excited-state $FAD^{\bullet-}$ occurs.

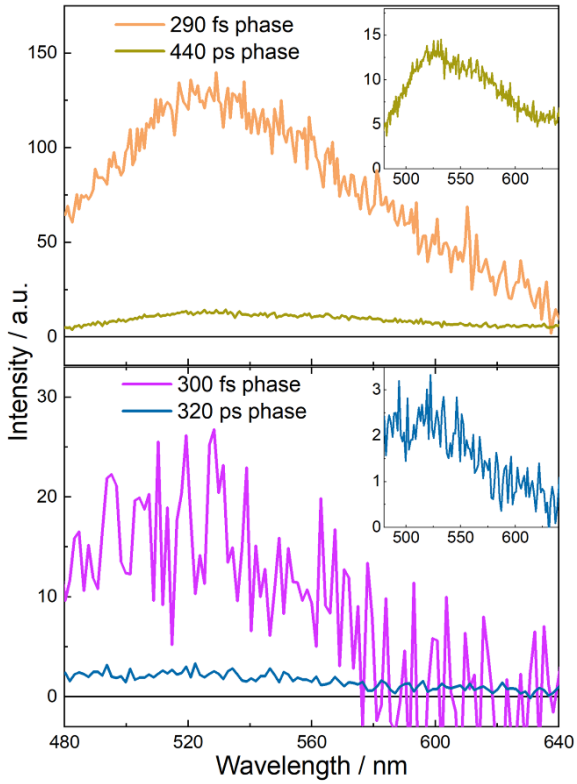

Figure 4.5 DAS from the global analysis of fluorescence decays of COX under oxidizing (*top*) and reducing (*bottom*) conditions with benzene as Kerr medium. inset panel: magnified long-lived phase.

Our assessment of lack of time-resolved $FAD^{\bullet-}$ fluorescence in COX contrasts with the report of $FAD^{\bullet-}$-assigned steady-state fluorescence peaking around 450 nm (at the blue of the 500 nm $FAD^{\bullet-}$ absorption maximum, i.e., violating the Kasha–Vavilov rule) in *A. globiformis* COX.[24] We note that C4a-flavin adducts, which can form in COX,[118] strongly fluoresce in this region.[119,120] Moreover, the only time-resolved fluorescence assigned to the anionic flavin radical remains that from insect cryptochrome,[16,23] although the spectral characteristics are very close to those of oxidized flavin, as also discussed in ref. 7.

4.3 Transient formation of oxidized flavins upon the excitation of anionic flavin radicals

The lack of emission in radical ions is usually explained by efficient internal conversion between D_1 and D_0 states, involvement of D_2/D_1 and D_1/D_0 conical intersections, or photoinduced ET when there is an electron donor or acceptor close-by.[121–124] To investigate the actual excited-state deactivation pathways of protein-bound anionic flavin radicals, we

performed transient absorption measurements. Pump pulses centered at 390 and 520 nm were used to excite the two distinct transition bands.

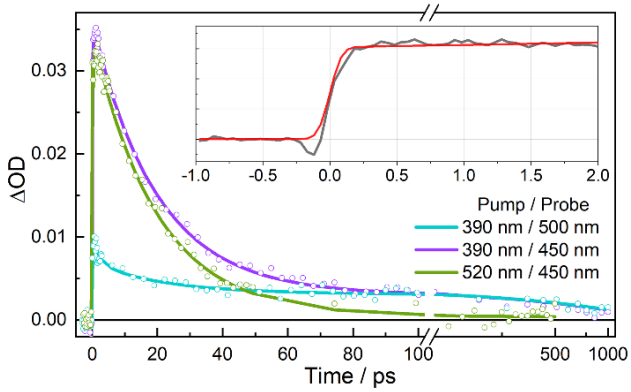

Figure 4.6 Isotropic transient absorption kinetics of $FAD^{\bullet-}$ in GOX at selected wavelengths upon excitation at 390 nm or 520 nm. Inset panel: the rise of induced absorption signal (grey) at 433 nm (at the minimum of the probe dispersion curve) under 390 nm excitation. The red curve represents an instrument-response limited rise.

The transient absorption kinetics of $FAD^{\bullet-}$ in GOX are shown in Figure 4.6, and the DAS extracted from the global analysis are given in Figure 4.7 and 4.8. Here the DAS was used to avoid the influence of potential parallel photochemical schemes arising from other excitable flavin forms that may be present in the samples. Upon excitation, we observed a marked induced absorption band formed within ~100 fs. This band is very similar to the $S_0 \rightarrow S_1$ transition band of ground-state FAD_{ox}. Under 520-nm excitation the decay of this band (time constant 19 ps) constitutes the only spectral evolution. Under 390 nm excitation this band has virtually identical shape (Figure. 4.8) and it decays with a very similar time constant. Along with the fact that we did not observe any emission with a similar lifetime in the time-resolved fluorescence measurements (*vide supra*), we conclude that this ~20 ps phase must arise from a non-emissive product state. Notably, the 390-nm excitation data also require two additional small kinetic phases with time constants of 1.8 and 900 ps to obtain a satisfactory global fit (Fig. 4.6 and 4.7). These time constants are similar to those of the excited-state lifetime of FAD_{ox} and $FADH^-$ (1.1/4.3 ps and 800 ps, respectively) in GOX;[12,18,32] the corresponding DAS, although too small to be reliably analyzed, also show resemblance to those obtained for FAD_{ox}[12] and $FADH^-$.[18]

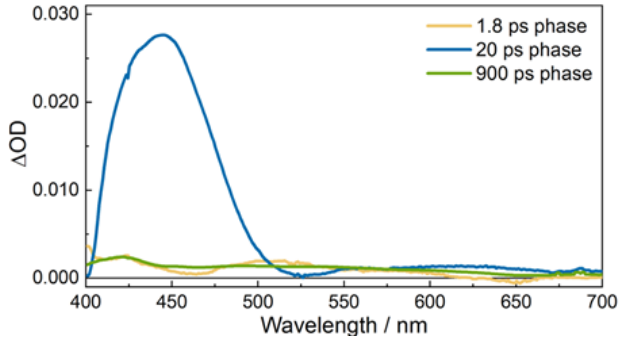

Figure 4.7 DAS of isotropic transient absorption data of $FAD^{\bullet-}$ in GOX under excitation at 390 nm.

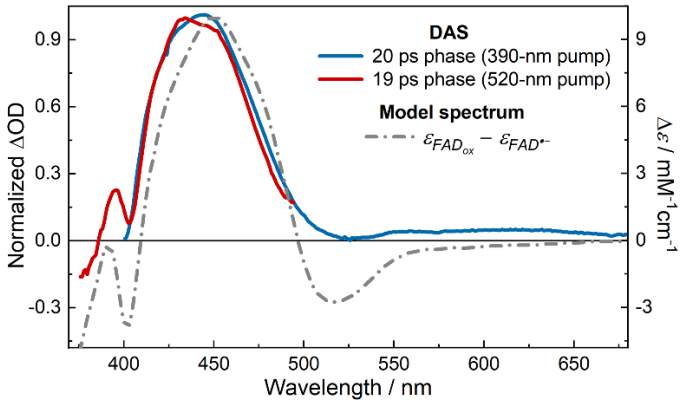

Figure 4.8 Comparison of the experimental DAS of $FAD^{\bullet-}$ in GOX under two excitation conditions and model spectrum constructed from steady-state spectra by assuming complete $FAD^{\bullet-}$ to FAD_{ox} conversion.

We observed similar transient absorption spectra for the anionic flavin radicals in the other flavoprotein oxidases. Upon excitation of $FAD^{\bullet-}$ or $FMN^{\bullet-}$ in COX, MSOX, DAAO and NMO, strong induced absorption bands centered at ~450 nm appeared in less than ~100 fs. They highly resemble the $S_0 \rightarrow S_1$ transition bands of ground-state FAD_{ox} or FMN_{ox} (Figure 4.9), and upon 520-nm excitation decay in a single-exponential manner in a narrow range of 10–20 ps (Figure 4.10).

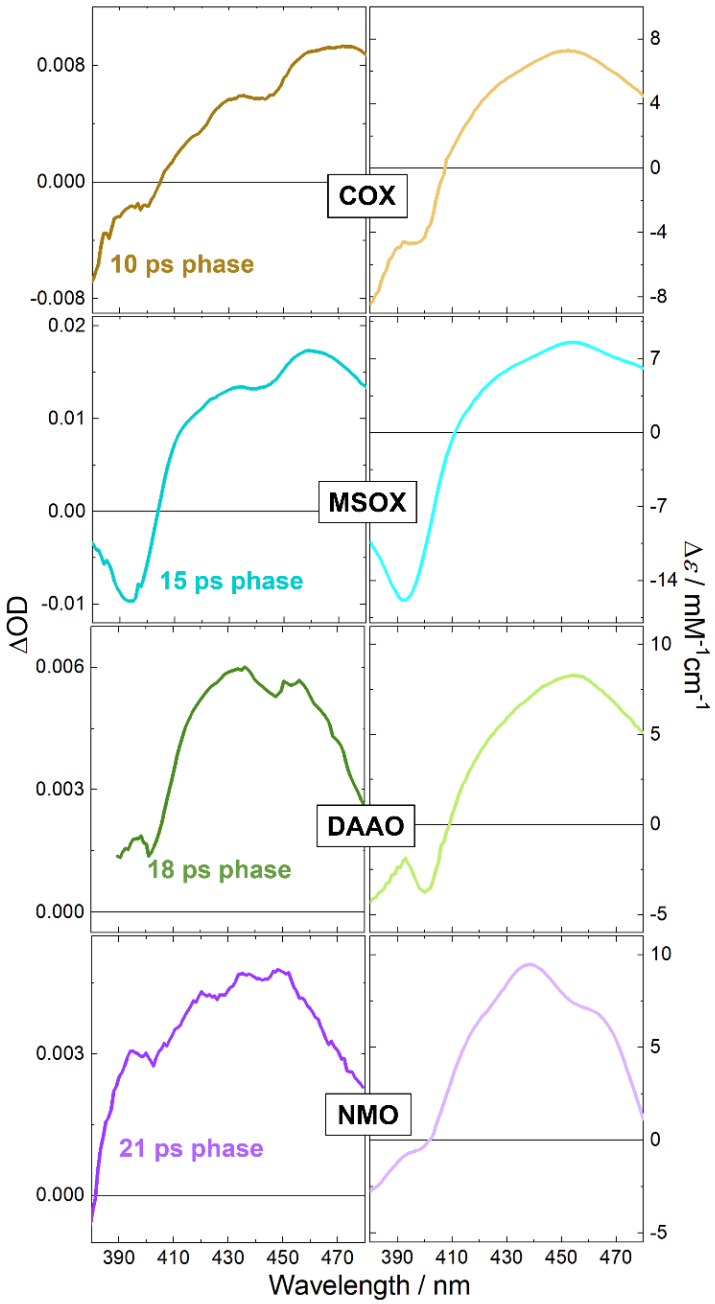

Figure 4.9 DAS of anionic flavin radicals in COX, MSOX, DAAO and NMO under excitation at 520 nm (*left*), as well as the corresponding steady-state difference spectra assuming complete $FAD^{\bullet-}$ to FAD_{ox} conversion (*right*).

In Figure. 4.8 and 4.9, spectral analysis is performed by comparing the DAS of the product states with steady-state difference spectra of the oxidized flavin and the anionic flavin radical. The overall features of the DAS, including the ground state bleaching and induced absorption, correspond well with the model spectra. Furthermore, taking into account the excitation density using $[Ru(bpy)_3]Cl_2$ as a reference, the amplitude of the signals indicates near-unity oxidized flavin formation per absorbed photon.

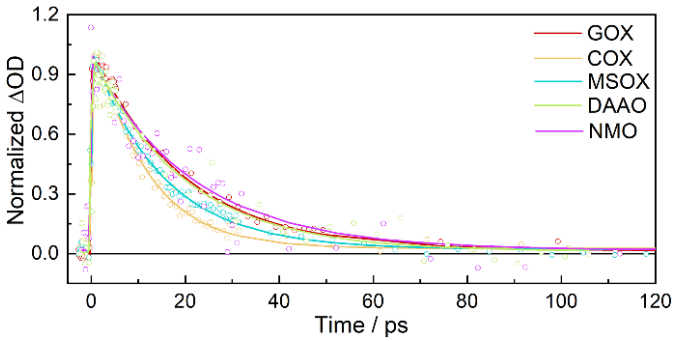

Figure 4.10 Isotropic transient absorption kinetics in different flavoprotein oxidases after excitation at 520 nm and monitored at 455 nm.

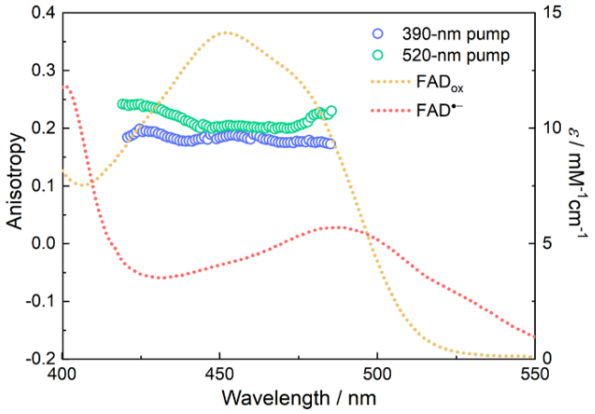

Figure 4.11 Transient anisotropy in the induced absorption regions calculated based on polarized DAS of the ~20 ps phase under two excitation conditions in GOX (colored circles). The steady-state absorption spectra of FAD_{ox} and $FAD^{\bullet-}$ in GOX are also shown as references (dashed lines).

Yet, the DAS are not strictly identical to the model spectra. This may be due to two reasons. First, given the ultrafast time scale, the transiently formed oxidized flavins are presumably in an unrelaxed protein environment resulting in a shifted absorption spectrum and altered vibrational progression. Second, during the photooxidation process, a radical intermediate formed from a yet unknown electron acceptor may also absorb in the visible region and contribute to the observed DAS. The second assumption is supported by the analysis of the transient anisotropy absorption spectra (Figure 4.11), which provides detailed insight in the orientation of the involved transition dipole moments.[125] In the 440–470 nm spectral range where the transient absorption is maximal, the anisotropies (r) are almost constant and very similar for 390-nm (r = 0.18–0.19) and 520-nm (r = 0.20–0.22) excitation. As in both cases mainly the $S_0 \rightarrow S_1$ transition band of FAD_{ox} was probed, this result indicates that the $D_0 \rightarrow D_4$ and $D_0 \rightarrow D_6$ transition dipole moments of $FAD^{\bullet-}$ in GOX are near-parallel. However, our previous study has shown that the $S_0 \rightarrow S_1$ transition dipole moment of FAD_{ox} should also be near-parallel to the $D_0 \rightarrow D_4$ transition of $FAD^{\bullet-}$, which corresponds to a r value close to 0.4,[98]

whereas smaller values were observed in the present case. This may be explained by broad contributions from transition dipole moments of a third species in the probed region.

4.4 Identity of the electron acceptor

Taken together, our time-resolved fluorescence and transient absorption measurements provide a consistent picture that ultrafast photooxidation of anionic flavin radicals occurs in GOX, COX, MSOX, DAAO and NMO, followed by the back transfer of the ejected electron (or, strictly, charge "re-separation") on the picosecond timescale, as evidenced from the monophasic decay of the induced absorption band (Figure 4.10) and the absence of $FAD^{\bullet-}$ bleaching signals on longer timescales (Figure 4.6). The possibility of a photoionization reaction that leads to the formation of the oxidized flavin/hydrate electron pair can also be excluded as the extinction coefficients of a hydrated electron in the > 600 nm spectral range are > ~15 $mM^{-1}cm^{-1}$,[126] if it is formed at a similar concentration to that of the oxidized flavin, we should be able to observe considerable contribution from its absorption in the transient spectrum.

With regard to the possible candidates of the corresponding electron acceptors, we rule out the involvement of by-products produced upon preparing the anionic flavin radicals in the steady state, as similar results were obtained with different reduction methods, including photoreduction. The ultrafast formation of the transient oxidized flavins and the monophasic decays suggested a close interaction and a well-defined conformation between the electron donor and acceptor, which makes active-site residues appropriate candidates. Using multiple computational approaches, we further investigated the identity of the electron acceptor from a theoretical perspective, which are detailed in the following subsections.

4.4.1 DFT calculations

In DFT, the ionization potential (IP) and the electron affinity (EA) of a molecule can be approximated by the negative of the HOMO (which to be more precise refers to the highest occupied Kohn–Sham levels here) of the N and $N + 1$ electron systems, respectively.[127–129] For those active-site residues in the investigated flavoprotein oxidases, DFT calculations were thus carried out to evaluate their EA by optimizing their geometries in the one-electron-reduced forms ($N + 1$). The result shows that in vacuum only the neutral radicals of fully protonated histidine and arginine have reasonable negative HOMO energies (−5.24 and −5.92 eV, respectively), indicating the relatively high (and close) EA, whereas for the other residues, including the singly protonated forms of histidine, the acceptance of an additional electron

leads to relatively unstable species (Table 4.1). Indeed, among the one-electron-reduced forms of common amino acids, so far only the neutral radical of isolated protonated histidine and arginine (or analogues) have been experimentally produced and spectrally characterized.[130,131] Together, this suggests that fully protonated histidine and arginine are the most likely candidates for the electron acceptors among those residues. Notably, the neutral lysine radical appears to have a moderately negative HOMO energy (−3.77 eV); the backbone amide group, which has been reported to quench *Trp fluorescence[132] and is present in proximity of the flavins, is determined to have a HOMO energy of −0.60 eV. Therefore, protonated lysine and backbone amide are energetically less favorable to act as electron acceptor compared with $HisH_2^+$ and $ArgH^+$.

Table 4.1. Molecular orbital energies of selected residue side chains in the one-electron reduced form. Energies were obtained on the geometry optimized at the ωB97X-D3/ma-def2-TZVP level in vacuum.

Residue	ϵ_{HOMO} (eV)
Arginine	−5.92
Asparagine	−0.14
Histidine (doubly protonated)	−5.24
Histidine (N_ε protonated)	−0.77
Histidine (N_δ protonated)	−0.42
Lysine	−3.77
Methionine	−0.28
Phenylalanine	−0.17
Tyrosine	−0.28
Tryptophan	−0.08
Backbone amide group*	−0.60

**N*-methylacetamide was used as an analog.

As illustrated in Figure 4.1, in the five flavoprotein oxidases investigated in this study (and possibly in all other functional flavoprotein oxidases), there is always a positively charged residue, including either histidine or arginine, present in the active site. Based on the crystal structures only it is difficult to identify the electron acceptors more clearly; the structures are thought to correspond to the oxidized flavin, and structural rearrangement may take place upon flavin reduction (*vide infra*). Yet, we note that in COX the covalently linked and functionally relevant histidine, His99,[133] is most probably neutral, since in the crystal structure its N_δ atom

does not appear to have any proton donor partners, and the pK_a of 8α-*N*-imidazole-substituted flavins is determined to be ~6 (N of the imidazole moiety) in solution;[134] therefore it is not a likely electron acceptor, making His466 a more likely candidate.

The lifetimes of the formed photoproducts in the five investigated systems span a remarkably narrow range of ~10–20 ps, with three of the lifetimes being at 20 ps within experimental error, indicating that the back reactions involve similar distances and electronic properties. This finding may be linked to the very similar and close distances between the flavins and nearby histidine or arginine residues in the five flavoprotein oxidases (Figure. 4.1), as well as the similar EA of histidine and arginine residues (Table 4.1). Such properties may be a prerequisite for the formation and stabilization of anionic flavin radicals in proteins.[135] Qualitatively, this finding may also be related to the common requirements of the oxidases to stabilize the highly reactive reaction intermediate such as $O_2^{\bullet-}$ in the active site by a positive charge in close proximity to the flavin.[136]

4.4.2 MD simulations

Among the five flavoprotein oxidases, the structural properties of GOX are the most extensively studied and relatively well-understood, making it an appropriate system for further theoretical investigation of the electron donor. In GOX, there are two histidines located very close to the flavin in the active site (Figure 5.1), i.e., His516 and His559 (3.83 Å and 3.76 Å minimal ring-ring distance to FAD in the crystal structure, respectively). In accord with the DFT calculations above, a doubly protonated histidine is more likely to act as electron acceptor, we examined the protonation state of these two histidines. His559 forms strong hydrogen bonds to Glu412 and is expected to be double protonated over a broad pH range.[137,138] On the other hand, the protonation state of His516 in the presence of $FAD^{\bullet-}$ is less clear. We performed MDFE simulations to estimate its pK_a value in the presence of $FAD^{\bullet-}$, which calculates double free energy difference ($\Delta\Delta G$) of the corresponding protonation/deprotonation process comparing with a reference model in the solution. The pK_a of the titratable group in the protein environment can then be calculated by:

$$\mathrm{p}K_{\mathrm{a,prot}} = \mathrm{p}K_{\mathrm{a,ref}} + \frac{\Delta\Delta G}{2.303RT} \qquad (4.1)$$

Calculations were also performed in the presence of $FADH^-$, since the experimental pK_a value of His516 was measured previously with this state of flavin, with a value of 8.1 determined by the reaction rates of the reduced enzyme toward O_2.[138] The results (Table 4.2)

show that, in the presence of $FADH^-$, the pK_a of His516 is calculated to be 9.6 (SD: 0.4), which is reasonably close to the experimental value. The calculation further shows that, in the presence of $FAD^{\bullet-}$, His516 also has a very high pK_a of 13.5 (SD: 0.7), due to interactions with the negatively charged $FAD^{\bullet-}$ and nearby Asp328. Therefore, in GOX these two histidines, His516 and His559, both are likely to be doubly protonated in the presence of $FAD^{\bullet-}$. The active site of GOX appears to be arranged in a way that in the reduced form the pK_a of the flavin cofactor is downshifted,[139] while those of the two histidines are upshifted.

Table 4.2. Results of pK_a calculations for His516 in GOX based on MDFE simulations. Statistical uncertainty in parentheses estimated as twice the standard deviation of block averages, with each data set being divided into five blocks. N/A, not applicable. N/D, not determined.

	With $FAD^{\bullet-}$ (His516, GOX)	With $FADH^-$ (His516, GOX)	Explicit solvent (dipeptide)
$\Delta\Delta G_{calc}$ (kcal/mol)	8.8 (0.9)	3.5 (0.5)	N/A
pK_a (calc.)	13.5 (0.7)	9.6 (0.4)	N/A
pK_a, (exper.)	N/D	8.1*	7.0

*The experimental value is from ref. 138.

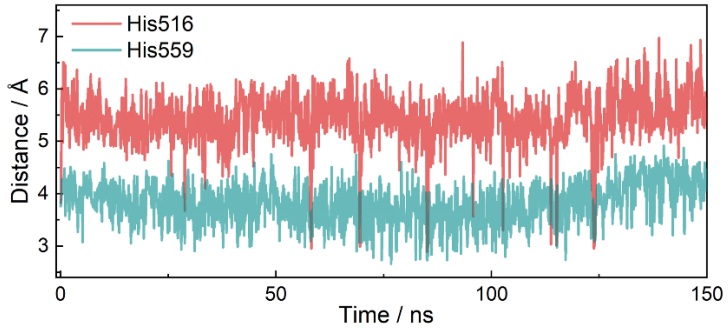

Figure 4.12 The minimal ring-to-ring distance between $FAD^{\bullet-}$ and His516 or His559 in the MD simulation of GOX.

All-atom MD simulations were then performed for GOX with the flavin in the anionic radical state and both His516 and His559 doubly protonated. As shown in Figure 4.12, throughout the 150-ns MD simulation, His559 remains very close to $FAD^{\bullet-}$ with an average minimal ring-to-ring distance of 3.81 Å. On the other hand, His516 rotates around $\chi 2$ to a noncatalytic orientation, as was shown previously,[140] and stays relatively far away from $FAD^{\bullet-}$ (~5.5 Å), and only transiently approaches the cofactor. The shorter distance of 3.83 Å between flavin and His516 observed in the crystal structure is explained by the fact that His516 is singly protonated with FAD_{ox} in the crystal structure. This accords with previous studies showing that His516 is a flexible, functionally important residue that can flip between catalytic and

noncatalytic conformations.[137,140] Given the closer interactions of His559 with $FAD^{\bullet-}$, it appears to be a suitable candidate for accepting an electron from excited $FAD^{\bullet-}$.

4.4.3 QM/MM spectral calculations

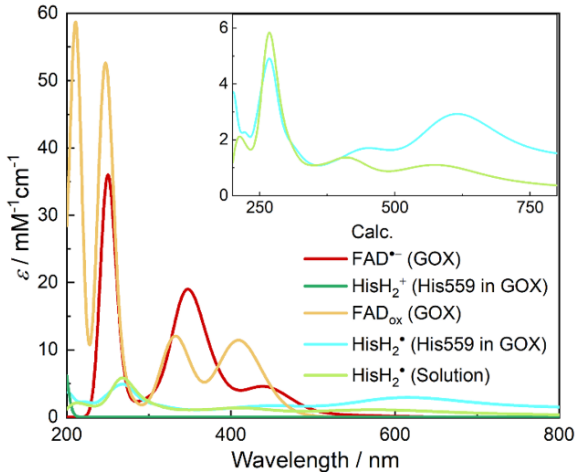

Figure 4.13 Calculated absorption spectra of individual species involved in the photooxidation process of $FAD^{\bullet-}$ in GOX.

Assuming His559 as the electron acceptor, we employed a QM/MM protocol to calculate the transient absorption spectra of $FAD^{\bullet-}$ photooxidation in GOX, including the induced absorption of FAD_{ox} and $HisH_2^{\bullet}$, as well as the ground-state bleaching of $FAD^{\bullet-}$ (~500–550 nm; $HisH_2^+$ only absorbs in the ultraviolet range). The calculated spectra of individual species are shown in Figure 4.13 and the comparison with the experimental DAS is shown in Figure 4.14.

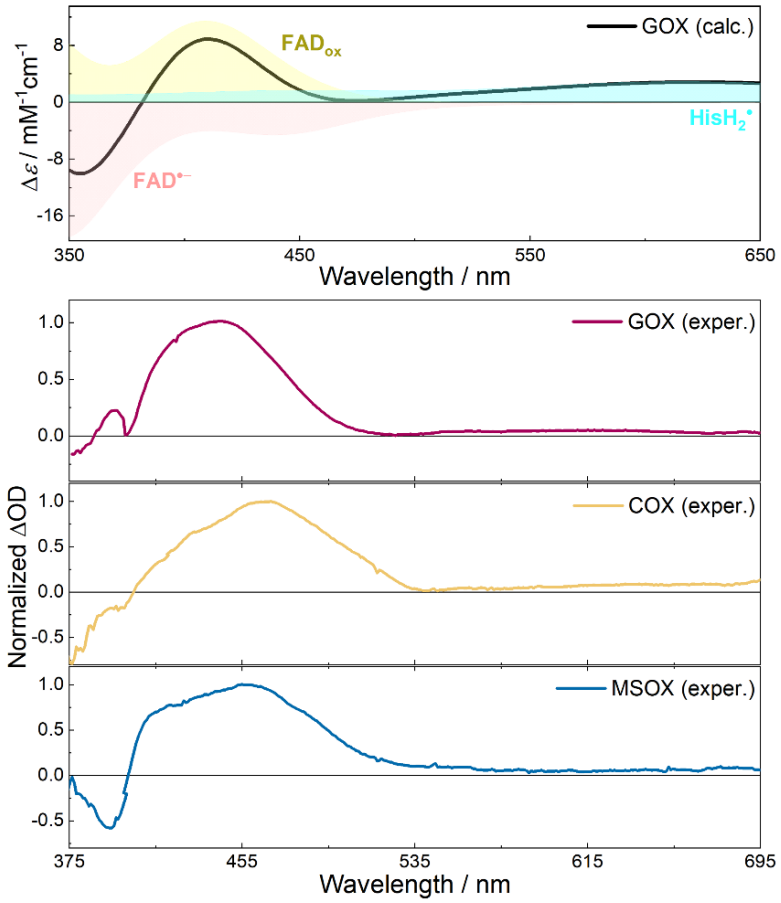

Figure 4.14 Calculated transient spectrum of $FAD^{\bullet-}$ photooxidation in GOX by superimposing individual spectra of corresponding components in Figure 4.13. Wavelength ranges of calculated and experimental spectra are different to account for a rigid shift arising from the limitation of calculations.[56,105]

Despite some overestimations of the transition energies, the calculated spectra of FAD_{ox} and $FAD^{\bullet-}$ (Figure 4. 13) agree well with the experimental spectra (Figure. 4.2). In the near ultraviolet range, the calculated spectrum of $HisH_2^{\bullet}$ in aqueous solution agrees well with the experimental spectrum obtained by pulse radiolysis.[130,141] Notably, in GOX, $HisH_2^{\bullet}$ formed from His559 displays more intense absorption in the visible/near-infrared range compared with its state in solution (inset of Figure. 4.13), presumably due to effects of the complex protein environment around His559, in particular the hydrogen-bonded Glu412. This partially compensates the bleaching of $FAD^{\bullet-}$ and leads to a red-extending tail in the overall difference spectrum, which reproduces the experimental DAS reasonably well (Figure. 4.14).

4.4.4 Free energy changes of redox processes based on the PB method

The free energy change associated with the $FAD^{\bullet-}/HisH_2^{+} \rightarrow FAD_{ox}/HisH_2^{\bullet}$ ET reaction in GOX was estimated as follows. In the protein system, the free energy change of the

investigated ET process ($\Delta G_{ET,prot}$) can be calculated by evaluating the electrostatic free energy difference of the two states relative to a reference system in the aqueous solvent:

$$\Delta G_{ET,prot} = \Delta G_{ET,solv} + \Delta\Delta G_{ES} \qquad (4.2)$$

where $\Delta G_{ET,solv}$ is the free energy change of the investigated ET process in the aqueous solution obtained by high-level QM calculations;[142,143] $\Delta\Delta G_{ES}$ is the double difference of electrostatic free energies of the systems before ($FAD^{\bullet-}/HisH_2^+$) and after ($FAD_{ox}/HisH_2^{\bullet}$) the ET reaction, respectively, evaluated using the PB method[77,144] in the protein (based on the geometries sampled from MD simulations) relative to the aqueous solvent. The results were averaged over 100 snapshots taken each 1.5 ns from the 150-ns MD trajectories. The partial charges in the MM region of the model were set accordingly to represent the system before and after the ET reaction. Based on this approach, we obtained a $\Delta G_{ET,prot}$ value of 2.19 (SD: 0.05) eV, which is less than the energy of a 520-nm photon (2.38 eV, corresponding to the red edge of the $FAD^{\bullet-}$ absorption), confirming that such a *photoinduced* ET reaction is energetically feasible. It is also worth noting that the protein environment is found to energetically disfavor the formation of $FAD_{ox}/HisH_2^{\bullet}$ pair with $\Delta\Delta G_{ES}$ = +0.23 (SD: 0.05) eV, hinting at the stabilization of the charges of $FAD^{\bullet-}$ and $His559^+$ by surrounding residues in the active site of GOX.

4.5 Concluding remarks

In this work we have demonstrated a novel photochemical reaction occurring in the anionic radical state of flavoprotein oxidases. We studied the photoproducts of these intrinsically unstable radical state in five different flavoprotein oxidases where they can be stabilized. Using ultrafast absorption and fluorescence spectroscopy, we unexpectedly found that photoexcitation systematically results in the oxidation of protein-bound anionic flavin radicals on a time scale less than ~100 fs. The thus generated photoproducts decay back in the remarkably narrow 10–20 ps time range. Based on molecular dynamics and quantum mechanics computations, positively charged active-site histidine and arginine residues are proposed to be the electron acceptor candidates. Altogether we established that, in addition to the commonly known and extensively studied photoreduction of oxidized flavins in flavoproteins, the reverse process, i.e., the photooxidation of anionic flavin radicals, can also occur. We propose that this process may constitute an excited-state deactivation pathway for protein-bound anionic flavin radicals in general, which therefore further extends the family of flavin photocycles (Figure 4.15). In view of the ephemeral nature of anionic flavin radicals in most biochemical and photobiochemical reactions where it could act as an intermediate,

whether the here-characterized photoreaction could play a physiological or photoprotective role in native proteins remains to be established.

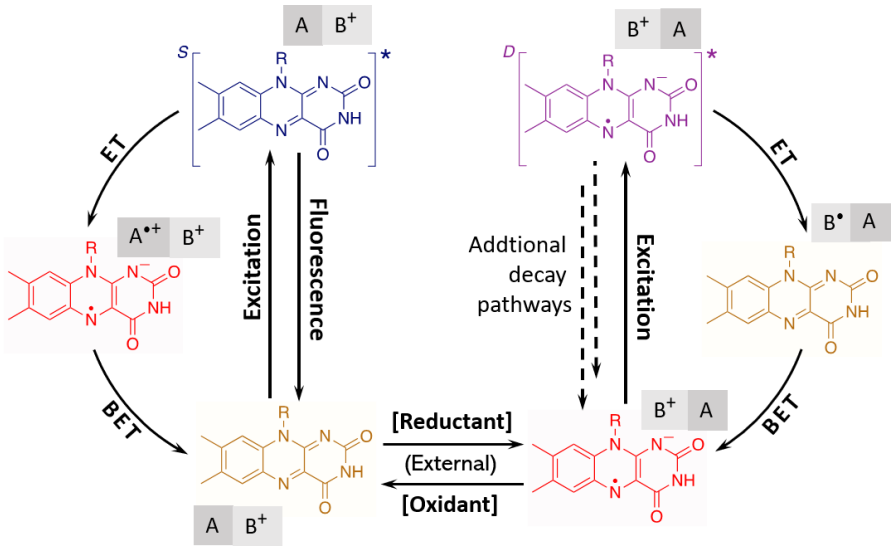

Figure 4.15 General reaction pathways for light-induced processes in flavoproteins that include the proposed cycle of the photooxidation of anionic flavin radicals. Formation of the doublet excited state and potential additional decay pathways (dashed lines) were not directly observed in this study. Flavin is represented by the isoalloxazine moiety. A stands for the electron-donating residue (tryptophan or tyrosine) and B^+ represents the electron-accepting residue (presumably histidine or arginine) in the protein active site.

Finally, we emphasize that we did not directly observe the formation of the excited state of anionic flavin radicals (Figure 4.6), leaving room for the discussion of the involved ET mechanism. Although our present simulations demonstrate that such a reaction should be energetically feasible, given the estimated weak driving force (~0.2 eV) it would be incompatible with a standard Marcus theory description using a reorganization energy in the 0.7–1 eV range.[38,39] However, on this timescale and with strong ionic interactions between the reactants, the underlying assumptions of thermalized reaction-coordinate motions and weak coupling are likely not fulfilled. Furthermore, we cannot completely rule out a CT excitation that leads to direct formation of a $FAD_{ox}/HisH_2^{\bullet}$ CT state, nor non-adiabatic transition from the locally excited state to a CT state. Nevertheless, a direct CT transition, which may overlap with the local excitation transition (cf. ref. 145), in principle requires very strong interactions between the donor–acceptor pair in the ground state to provide reasonable oscillator strength, which is difficult to evaluate using the present level of simulations. It is of note that the crystal structures of the proteins studied *a priori* correspond to those with oxidized flavins, and additionally for COX to a protein variant and for DAAO to a protein–inhibitor complex. When the flavins are reduced, the active-site conformations are likely to contain rearrangements. This

makes quantitative evaluation of ET dynamics and a definitive determination of the electron acceptor(s) challenging at this point. Moreover, variants of the close-lying positively charged residues are likely to influence the formation and stabilization of anionic flavin radicals, as well as affect the binding affinity for flavins.[135,138,146,147] Future studies combining more extensive theoretical investigations and spectroscopic experiments on genetically modified proteins will allow determining the exact nature of the electron acceptors and ultimately establish the precise molecular origin of the common dynamic features of ET in flavoprotein oxidases.

Chapter 5. Excited-State Properties of Fully Reduced Flavins

5.0 Introduction

In this chapter studies will be presented that concern the photophysical properties of fully reduced flavins, which have been subject to a very limited number of studies thus far. We focus on a number of FNR proteins, which, although homologous, display a variety of properties of the fully reduced forms, which may be related to their function. These FNRs and the steady-state properties of their fully reduced forms are first briefly introduced, and more general background on the photophysics of fully reduced flavins is then given before describing our results.

5.1 Fully reduced flavins in TrxR-type FNRs

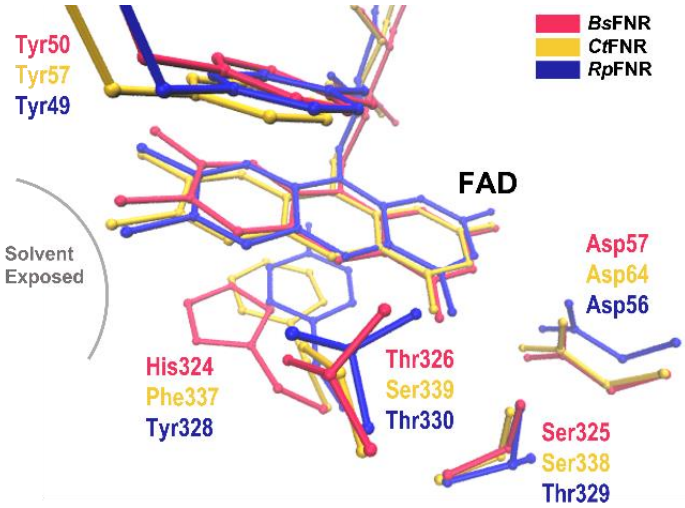

Figure 5.1 Active sites of *Bs*FNR, *Ct*FNR and *Rp*FNR (PDB entry: 3LZW, 3AB1 and 5YGQ, respectively) in the oxidized state. The crystal structures are aligned on the FAD cofactors.

FNR are flavoenzymes that can be classified into two major categories, plant-type and glutathione reductase (GR)-type based on amino acid sequence and structure analyses.[148] The NADPH-thioredoxin reductase (TrxR)-type FNR is a subgroup of the GR-type FNR found in green sulfur bacteria, firmicutes and several alpha-proteobacteria.[61] This group is distinct from other types of FNR as it is a homodimer in solution, with a highly conserved structural topology

with bacterial TrxR.[149] This chapter describes our study on the excited-state properties of the fully reduced FAD cofactors (FAD_{red}) in three TrxR-type FNRs at a physiological pH condition (pH 7.0), i.e., FNRs from the heterotrophic soil bacterium *Bacillus subtilis* (*Bs*FNR),[99] and the photosynthetic bacteria *Chlorobaculum tepidum* (*Ct*FNR),[150] which is photoautotrophic, and *Rhodopseudomonas palustris* (*Rp*FNR)[60] which can grow both photoautotrophically and heterotrophically.

FNRs catalyze redox reaction between the iron-sulfur protein ferredoxin (Fd) and $NAD(P)^+/H$, in either direction. Depending on their physiological role, i.e., catalyzing ferredoxin (Fd) reduction with NAD(P)H (in a variety of metabolic reaction chains), or $NAD(P)^+$ reduction with reduced Fd (in photosynthesis), FNRs from different organisms usually exhibits differences in their reactivity toward oxidized/reduced Fd and $NAD(P)^+/H$. Such reaction directionality is largely determined by the protein structures in different redox states, which influence the electronic properties of the flavin cofactors, as well as give rise to redox-dependent interactions between the cofactors and substrates.[151,152]

Generally, redox reactions between FNR and $NAD(P)^+/H$ proceed via the formation of flavin−$NAD(P)^+/H$ charge-transfer (CT) complexes, followed by hydride transfer reactions.[153] Whereas in the oxidized state, *Bs*FNR, *Ct*FNR and *Rp*FNR exhibit relatively similar reaction kinetics in the reactions with NADPH, with the rate constant of the rate-limiting hydride transfer step estimated to be ~500 s^{-1}, the fully reduced enzymes display distinct behavior when reacting with $NADP^+$.[60,61,104] Based on stopped-flow experiments, it has been demonstrated that for fully reduced *Rp*FNR the rate of this reaction has been found to occur very fast, with a rate constant for the hydride transfer step determined to be ~450 s^{-1}.[60] For *Bs*FNR, the rate of this reaction is unable to estimate due to the redox equilibrium, although the rapid formation of the FAD_{red}−$NADP^+$ CT complex after mixing has been observed.[104] The reaction between fully reduced *Ct*FNR and $NADP^+$ has been shown to be very slow, with an overall rate constant of ~5 s^{-1}, but unlike *Rp*FNR and *Bs*FNR, the absorption band due to the CT intermediates has not been observed during the reaction, indicating that the rate-determining step here is unlikely to be the hydride transfer but rather the accommodation of $NADP^+$.[61] Yet, the molecular basis that gives rise to these differences remains largely enigmatic.

The main differences in the structures of the three FNRs lie in the C-terminal region which forms part of the active sites. In the experimental crystal structures of the oxidized state (Figure 5.1), histidine (His324), phenylalanine (Phe337), and tyrosine (Tyr328) stack on the

re-face of the isoalloxazine ring moiety of the flavins in *Bs*FNR, *Ct*FNR, and *Rp*FNR, respectively.[60] Threonine residues are located close to the N5 atom of the flavins in the active site of *Bs*FNR and *Rp*FNR (Thr326 and Thr330, respectively), while a serine residue is located at a similar position in *Ct*FNR (Ser339). These residues potentially form hydrogen bonds with the N5 atoms of the flavins, which may contribute to maintaining the position of the C-terminal extension region in contact with the FAD-binding domain. However, no structure of fully reduced TrxR-type FNR has been determined thus far, which prohibits detailed an understanding of the structural level of the mechanisms involved in the redox reaction between FAD_{red} and $NADP^+$ in those enzymes. A crystal structure of the fully reduced form of spinach FNR has been reported, which is almost identical to that of the oxidized form,[154] although it has also been commented that the protein in the crystal seemed to be only partially reduced.[152] By contrast, the crystal structure of a different GR-type FNR (adrenodoxin reductase/putidaredoxin reductase homologue),[151] as well as TrxR from *Escherichia coli*[155] in the fully reduced form, reveals drastic local conformational changes in the active sites upon the two-electron reduction, including substantial butterfly bending of the flavin.

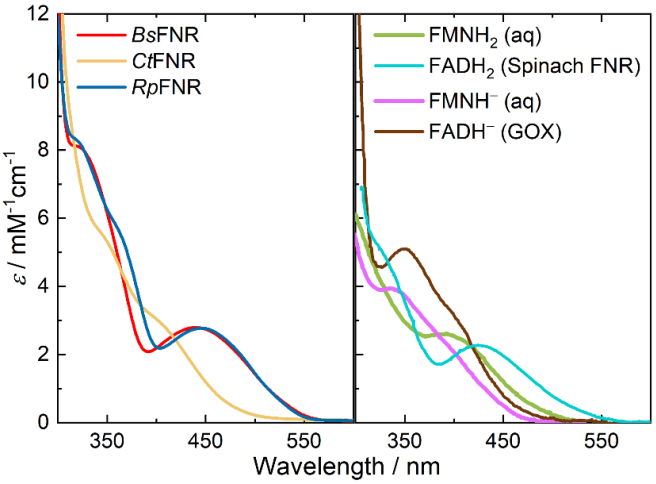

Figure 5.2 Steady-state absorption spectra of fully reduced flavins in *Bs*FNR, *Ct*FNR and *Rp*FNR, prepared by chemical reduction using dithionite at pH 7.0 (*left*), as well as those in aqueous solution (aq), GOX and spinach FNR reproduced from ref. 6, 5 and 156, respectively (*right*). The known protonation states of the species are indicated in parentheses.

As shown in Figure 5.2, the steady-state absorption spectra of FAD_{red} in *Bs*FNR and *Rp*FNR were found to be similar to each other, whereas that of *Ct*FNR is distinctly different. Compared with the spectra of fully reduced flavins obtained in aqueous solution, the spectral features of FAD_{red} in *Ct*FNR resemble those of the anionic form in solution, as well as FAD_{red} in GOX, which has been determined to be the anionic form $FADH^-$ based on a NMR study.[139] By contrast, in *Bs*FNR and *Rp*FNR they resemble those of $FADH_2$ in spinach FNR (at pH 6.0).

In spinach FNR, the FAD_{red} cofactor is titratable in the pH range where the protein can remain stable, and as the pH increases, the spectrum of FAD_{red} in this protein becomes more similar to that of *Ct*FNR.[156]

Although steady-state absorption spectra are available, the protonation states of FAD_{red} in *Bs*FNR, *Ct*FNR and *Rp*FNR have not been explicitly assigned in the literature. Yet, judging from the steady-state absorption spectra, it is very likely that at pH 7.0, FAD_{red} in *Ct*FNR exists in the form of $FADH^-$ and those of *Bs*FNR and *Rp*FNR exist in in the form of $FADH_2$.

5.2 Time-resolved spectral characterization of excited FAD_{red}

5.2.1 Overview

Photochemistry of fully reduced flavins is interesting from a fundamental point of view, as well as for developing potential applications in using flavoprotein variants as photocatalysts. It is commonly assumed that fully reduced (neutral or anionic) flavins are virtually nonfluorescent in solution, but they can have long-lived emissive excited states when their conformational dynamics are restricted by the protein environment or low temperatures.[6,17,18] This feature has been interpreted as a result of excited-state deactivation via a conical intersection (CI) with the ground state that can be reached through butterfly bending motions of the isoalloxazine ring system.[16,157] In confined environments, such motions are hindered, leading to long-lived (up to nanoseconds) excited states.

The excited state of $FADH^-$ is known to have a functional role in the photoenzyme DNA photolyase.[43] In recent years, employing the fully reduced flavins as the functional state (inspired by DNA photolyase) has become a promising approach in the development of bioengineered flavin-dependent photocatalysts.[50] Therefore, a basic understanding of the competing excited-state deactivation processes of fully reduced flavins is warranted. Moreover, time-resolved characterization of fully reduced flavins can also provide useful insights into the electronic properties of the flavin cofactors and their interactions with the hosting proteins. For instance, the excited-state decay of $FADH^-$ in the methyltransferase flavoenzyme ThyX has been interpreted in terms of the rigidity of the active site.[157]

In this work, we applied transient absorption and time-resolved fluorescence spectroscopies to investigate the excited-state properties of FAD_{red} in *Bs*FNR, *Ct*FNR and *Rp*FNR, which are involved as important intermediates in the functional processes of these proteins whereas no experimental crystal structure corresponding to this redox state is available (see above). Additionally, although time-resolved investigations on the excited FAD_{red} in

aqueous solution and in GOX have been previously reported in the literature,[14,16,18,157] for comparison, we also present here their time-resolved spectra under the same experimental conditions as those of the FNRs and analyze using the same methods. As has been demonstrated by a detailed analysis of high-quality data by Plaza's group,[14,157,158] the transient absorption spectra of $FADH^-$ can undergo subtle spectral changes on the timescale of a few picoseconds, which are usually interpreted in terms of vibrational relaxation ("cooling") of the excited state, and possibly also involve the response of the environment.[106,157,159] For oxidized flavins, such processes sometimes can also be observed in time-resolved fluorescence emission spectra as a slight red-shift of the emission spectrum in a few picoseconds.[29,34] Nevertheless, interpreting the precise origin of such spectral changes or shifts based on only UV-vis absorption or emission spectra is presently difficult. Our time-resolved measurements of $FADH^-$ (either free or protein-bound) also confirmed the presence of small kinetic phases that are assignable to vibrational relaxation, whereas those of $FADH_2$ do not display such features as has also been pointed out in ref. 157 and 158. In the present work, we did not attempt to fully describe the minor kinetic phases that presumably correspond to vibrational relaxations[157], but focus on the overall decay of the excited state.

5.2.2 Fluorescence decays

Time-resolved fluorescence measurements and the corresponding global analysis (Figure 5.3) revealed that in aqueous solution, the major component of the fluorescence of free $FADH^-$ decays in 16 ps and that of free $FADH_2$ decays in 4 ps, with negligible long-lived phases. The obtained DAS of the emission spectra show that in solution, excited-state $FADH^-$ emits with a maximum at ~575 nm, whereas that of $FADH_2$ is significantly shifted to longer wavelengths with a maximum at ~620 nm.

The fluorescence of FAD_{red} in *Ct*FNR can be reasonably fitted with a monophasic decay with a time constant of 400 ps, and the responding DAS has an emission maximum at ~550 nm, which is very similar to the DAS of the $FADH^-$ fluorescence in GOX that decays in 800 ps (see also Section 4.2 of **Chapter 4**). These findings confirm the above assessment from the steady-state absorption spectrum that for *Ct*FNR at pH 7.0, the FAD_{red} cofactor exists in the form of $FADH^-$.

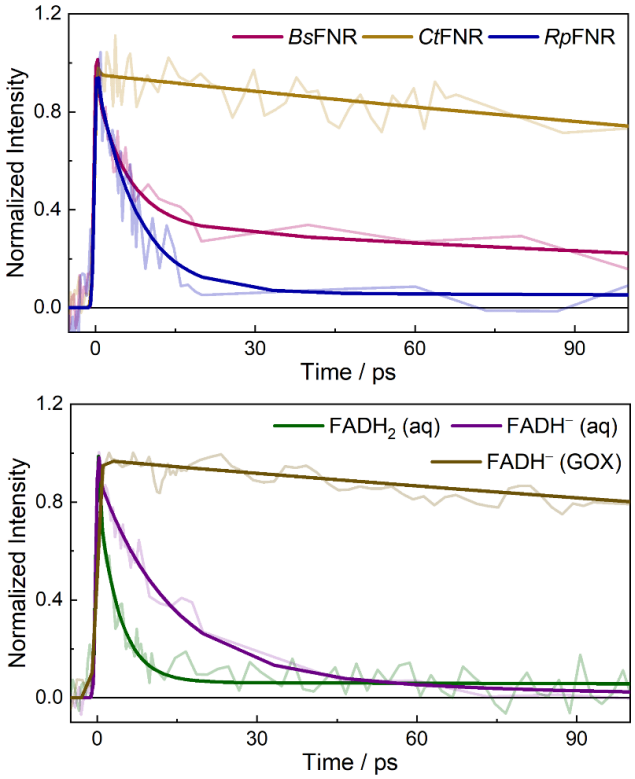

Figure 5.3 Fluorescence decays of FAD_{red} in *Bs*FNR, *Ct*FNR and *Rp*FNR monitored at 587, 532 and 589 nm (*top*), as well as $FADH^-$ and $FADH_2$ in aqueous solution, and $FADH^-$ in GOX, monitored at 569, 593 and 530 nm, respectively (*bottom*). The intensities are normalized, and exponential fits are shown as smooth curves.

On the other hand, the fluorescence of FAD_{red} in *Bs*FNR and *Rp*FNR shows much faster decays, which can be reasonably fitted with two components. For *Bs*FNR, the time constants are determined at 6 and 300 ps, and those for *Rp*FNR are 8 and 700 ps. The DAS of the 6-ps phase of *Bs*FNR and the 8-ps phase of *Rp*FNR highly resemble that of free $FADH_2$, displaying emission maxima at ~620 nm. The 700-ps phase of *Rp*FNR is very small, and the maximum of the corresponding DAS at ~525 nm is close to what would be expected for oxidized flavins. Therefore, we attribute this long-lived phase to a trace amount of FAD_{ox} (either in non-bound or protein-bound form) and the 8-ps phase to *Rp*FNR-bound $FADH_2$, which is the dominant form of FAD_{red} in *Rp*FNR at pH 7.0.

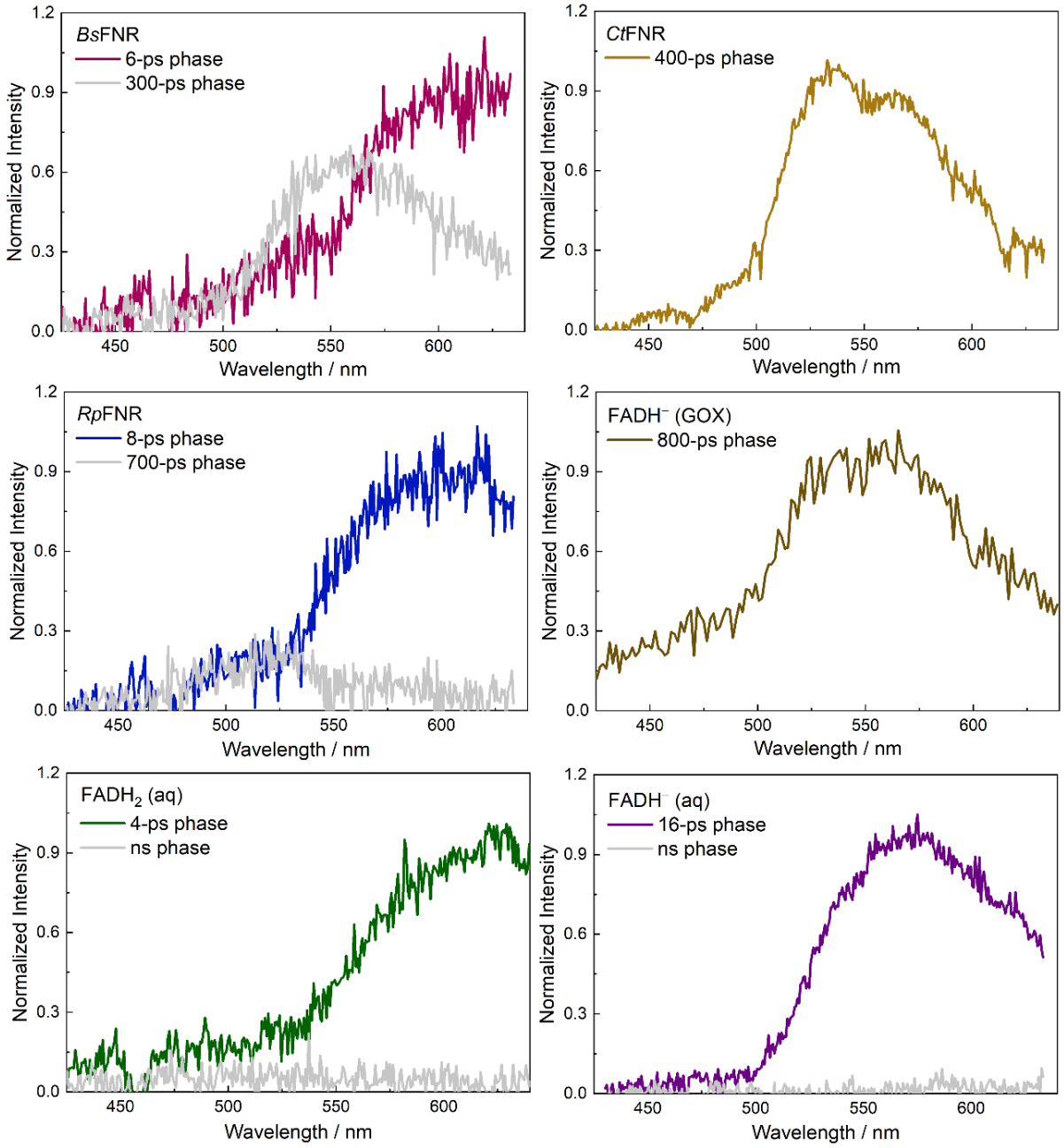

Figure 5.4 DAS from the global analysis of the fluorescence decays of FAD_{red} in *Bs*FNR, *Ct*FNR and *Rp*FNR, as well as $FADH_2$ and $FADH^-$ in aqueous solution (at pH 4.0 and pH 10.0, respectively), and $FADH^-$ in GOX.[57] Intensities are normalized on the maxima of the dominant phases.

The 400-ps phase of *Bs*FNR, however, has a comparable amplitude to the 6-ps phase, and its DAS exhibits an emission maximum at ~550 nm, similar to those of FAD_{red} in *Ct*FNR and $FADH^-$ in GOX. The lifetime of 300 ps of this phase is also close to that of 400 ps in *Ct*FNR. This result suggests that at pH 7.0, FAD_{red} in *Bs*FNR most likely comprises two protonation states: the majority $FADH_2$ contributes to the 6-ps phase in the fluorescence decay while a fraction of $FADH^-$ accounts for the remaining 300-ps phase.

As in *Ct*FNR and *Rp*FNR, the FAD_{red} cofactors are predominantly present in the anionic and neutral forms, respectively, we can approximately estimate that in TrxR-type FNRs, at the excitation wavelength (390 nm) of our time-resolved measurements, the extinction coefficient of $FADH^-$ is ~1.5 times higher than that of $FADH_2$ (Figure 5.2). For *Bs*FNR, based on this value and the relative amplitudes of the DAS in the time-resolved fluorescence measurement (Figure 5.4), we can estimate a ratio of $FADH_2$:$FADH^-$ of 7:3 at pH 7.0.

5.2.3 Transient absorption measurements

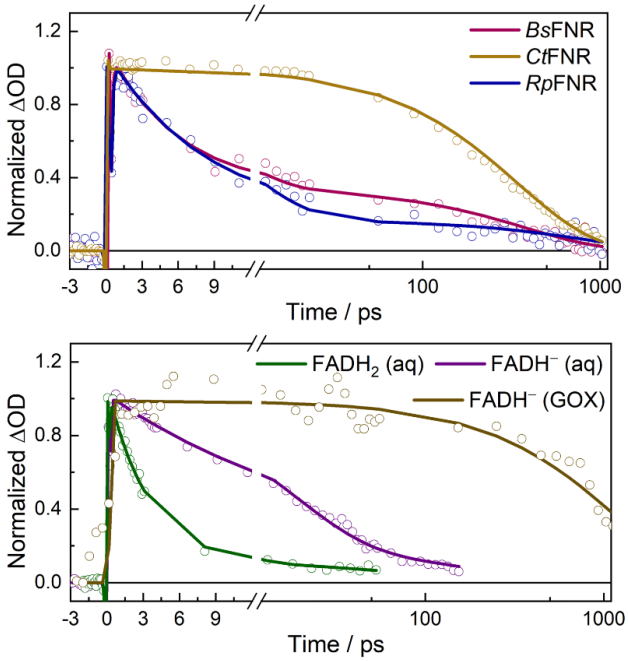

Figure 5.5 Kinetic traces at 520 nm from the transient absorption measurements of FAD_{red} in *Bs*FNR, *Ct*FNR and *Rp*FNR, as well as $FADH_2$ and $FADH^-$ in aqueous solution (at pH 4.0 and pH 10.0, respectively), and $FADH^-$ in GOX. Intensities are normalized on the maxima.

The extremely fast excited-state decays as measured by the emission of FAD_{red} in *Bs*FNR and *Rp*FNR (6 and 8 ps, respectively) are unparalleled compared with those of other protein-bound fully reduced flavins reported in the literature, which usually decay in at least hundreds of picoseconds.[16–18,157] To investigate whether their excited states indeed decay directly back to the ground state (via a CI) as appears the case for other systems, and not via other radiationless decay pathways such as photoinduced ET reactions, we further performed transient absorption measurements. The kinetic traces at 520 nm from the measurements are shown in Figure 5.5 and the DAS from the global analysis of the data are given in Figure 5.6. The found time constants of the dominant components in all the cases, including *Bs*FNR and *Rp*FNR, correspond well with those found in time-resolved fluorescence (Figure 5.4), indicating that the excited states deactivate back to the ground states, without the formation of

longer-lived intermediate product states (for the nanosecond phases, see below). Altogether, the observed transient spectra comprise contributions from the ground-state bleaching (~400–550 nm), stimulated emission (maximized at ~550 nm for $FADH^-$ and at ~620 nm for $FADH_2$, cf. Figure 5.4) superimposed on broad excited-state absorption, presumably across the whole investigated spectra range.

The transient absorption spectra of $FADH_2$ and $FADH^-$ in aqueous solution (corresponding to the DAS of the 4-ps and 18 ps phases, respectively) agree with previous reports.[14,18,158] The broad and featureless spectra of the minor nanosecond phases (which appear to be associated with non-emissive states, cf. Figure 5.4) have been previously assigned to $FADH^{\bullet}$/hydrated electron and $FADH_2^{\bullet+}$/hydrated electron pairs as a result of biphotonic ionization of FAD_{red}.[14,158]

The DAS of FAD_{red} in *Ct*FNR displays two major bands centered at ~530 and ~415 nm, similar to those resulting from excited $FADH^-$ in GOX and aqueous solution. The two major bands in the DAS of the 5-ps phase of *Bs*FNR and the 9-ps phase of *Rp*FNR, are centered at ~500 and 410 nm. These maxima, as well as the overall spectral features, are almost identical to those of the DAS of the 4-ps phase of $FADH_2$ in solution. The DAS of the 200-ps phase of *Bs*FNR, however, is smaller in amplitude than that of the 5-ps phase and resembles a $FADH^-$ transient spectrum as in *Ct*FNR, indicating that two forms of FAD_{red} with different protonation states coexist in the sample. These findings further support our assignments of the protonation states for FAD_{red} in the three FNR systems based on the results of time-resolved fluorescence. Overall, although the transient spectra of protein-bound $FADH^-$ are found to be similar to the transient spectrum in solution, they also become broader and exhibit more vibrational structures, unlike the transient spectra of protein-bound $FADH_2$ in *Bs*FNR and *Rp*FNR, which appear less influenced by the protein environments.

It is also worth noting that the transient absorption results of *Bs*FNR and *Rp*FNR also include a small very broad, featureless nanosecond long-lived phase that extends to the red edge (absent for *Ct*FNR), similar to the nanosecond phases in the measurement of $FADH_2$ in solution. This suggests that also some biphotonic ionization reactions occur, leading to the formation of the $FADH_2^{\bullet+}$/hydrated electron pair. Therefore, we can further speculate that in the fully reduced state, the active sites of *Rp*FNR and *Bs*FNR should contain enough water molecules to allow the detached electron to be solvated.

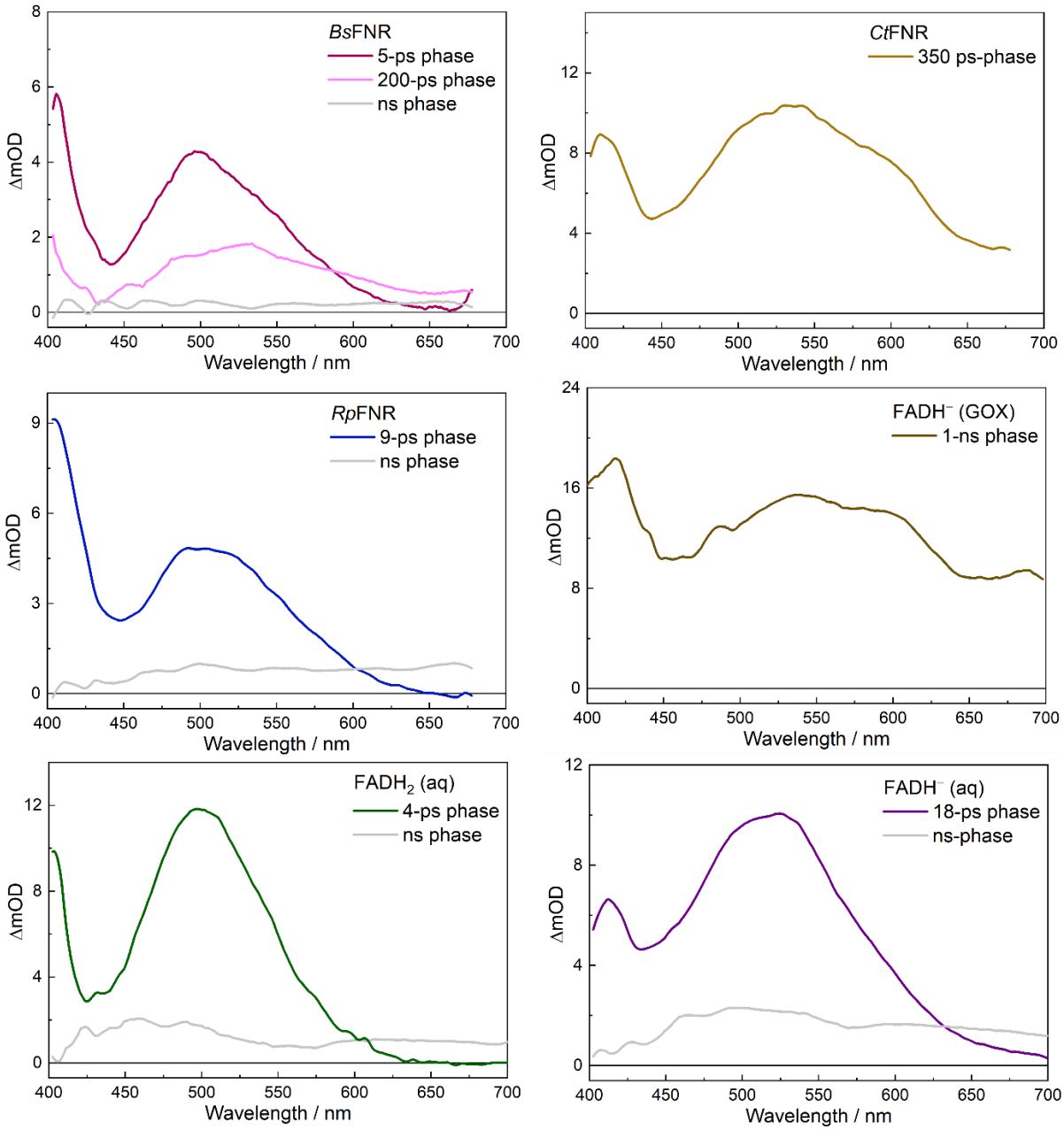

Figure 5.6 DAS from the global analysis of the transient absorption data of FAD_{red} in *Bs*FNR, *Ct*FNR and *Rp*FNR, as well as $FADH^-$ and $FADH_2$ in aqueous solution, and $FADH^-$ in GOX.

5.3 Constraints from the active sites

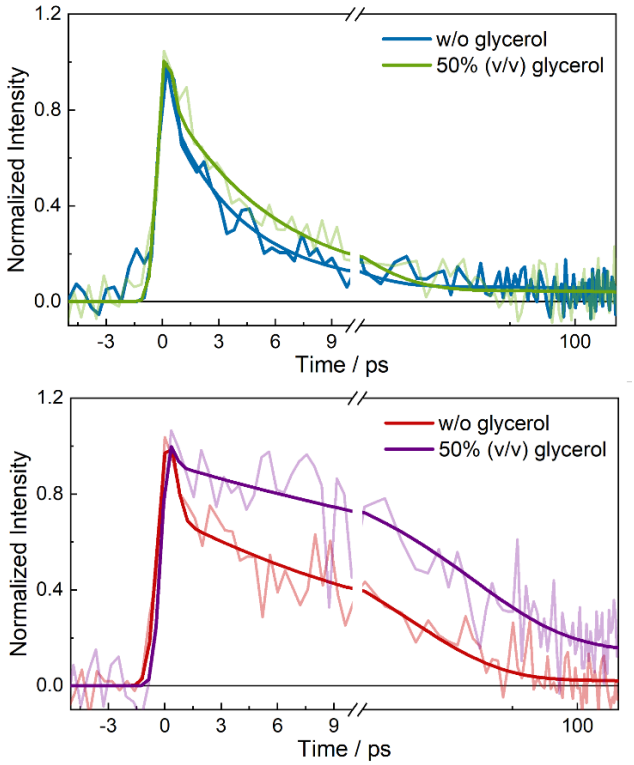

Figure 5.7 Fluorescence decays of $FADH_2$ (*top*, monitored at 593 nm) and $FADH^-$ (*bottom*, monitored at 569 nm) in aqueous solution in the absence or in the presence of 50% (v/v) glycerol. The time axes are in linear-logarithmic scale for clarity. The faster phases close to the IRF (~1 ps) correspond to small relaxation processes.

To evaluate the effects of a denser environment on excited-state dynamics of fully reduced flavins, we performed time-resolved fluorescence measurements on solutions of $FADH^-$ and $FADH_2$ containing 50% glycerol (v/v), where the viscosity of the solution increases by a factor of ~9. It is well-known that the fluorescence properties of fully reduced flavin can be affected by the viscosity of the solvent;[6] a qualitatively interpreted time-resolved fluorescence experiment has been conducted for $FMNH^-$ in a glycerol/water mixture,[16] and the corresponding experiments on $FADH^-$ and $FADH_2$ are lacking.

As shown in Figure 5.7, in the presence of 50% glycerol (v/v), the 16 ps decay phase component in the fluorescence decay of $FADH^-$ turns into 31 ps, slowing down by a factor of ~2; the amplitude of the long-lived phase also increases, indicating that there may be an even slower decay component appearing. The fluorescence of $FADH_2$ in the glycerol/water mixture decays in 6 ps, slowing down by a factor of ~1.5 compared with the fluorescence lifetime of 4 ps in glycerol-free solution, and there is no noticeable change in the long-lived phase.

Correlating these observations with results of fluorescence decays of FAD_{red} in the three FNRs, we can assert that in *Bs*FNR and *Rp*FNR (where the fluorescence of $FADH_2$ decays in 6 and 8 ps, respectively), the constraints from the protein active sites that are exerted on the $FADH_2$ cofactors are similar to the effects of 50% (v/v) glycerol. By contrast, in *Ct*FNR the fluorescence of $FADH^-$ decays in 400 ps, > 10 times slower than that in the glycerol/water mixture (31 ps), indicating that the active site of fully reduced *Ct*FNR is likely to be much more rigid. As the fluorescence decay of $FADH^-$ in GOX is even slower (800 ps), this implies that the active site of fully reduced *Ct*FNR still imposes fewer constraints on the cofactor than that of GOX.

We used MD simulations to further examine the active-site configurations of fully reduced FNRs from a theoretical perspective. 200-ns simulations for each protein were carried out with the cofactor in the form of $FADH_2$ for *Bs*FNR and *Rp*FNR, and $FADH^-$ for *Ct*FNR. As we used the experimental crystal structures that correspond to the oxidized form as the initial structures for these simulations, we performed the analysis on the last 100 ns of the simulations, to allow the geometries of the proteins to be fully relaxed.

We focus on three residues that closely interact with the oxidized cofactors in the crystal structures and characterize the active site of TrxR-type FNRs (Figure 5.1), namely, Tyr50, His324 and Thr326 in *Bs*FNR, Tyr49, Tyr328 and Thr330 in *Rp*FNR, Tyr57, Phe337 and Ser339 in *Ct*FNR. Figure 5.9 shows the distances between the flavin ring and these residues. During the MD simulations, the stacking conformation of the two aromatic residues and the flavin rings were relatively well-preserved, with average distances of ~3.4–3.6 Å, comparing well with those in the crystal structures, although slightly larger fluctuations were observed in the cases of *Bs*FNR and *Ct*FNR (Figure 5.9, *top* and *bottom* panels).

Thr326, Thr330 and Ser339 are found at similar positions and presumably form hydrogen bonds with the FAD_{ox} cofactors in the crystal structures of *Bs*FNR, *Rp*FNR and *Ct*FNR, respectively; yet, in the MD simulations with FAD_{red} in the active sites, they exhibit contrasting structural dynamics. Ser339 remains close to the $FADH^-$ cofactor in *Ct*FNR and the hydrogen-bonding interactions between them are maintained (Figure 5.10, *bottom* panel). By contrast, in the simulations of *Rp*FNR, Thr330 moves away (cf. Figure 5.1), and adopts configurations that are ~6 Å away from the flavin on average, where the C-terminal extension change its conformation, opening up the active site and exposing the cofactor more to the solvent (Figure 5.10, *middle* panel).

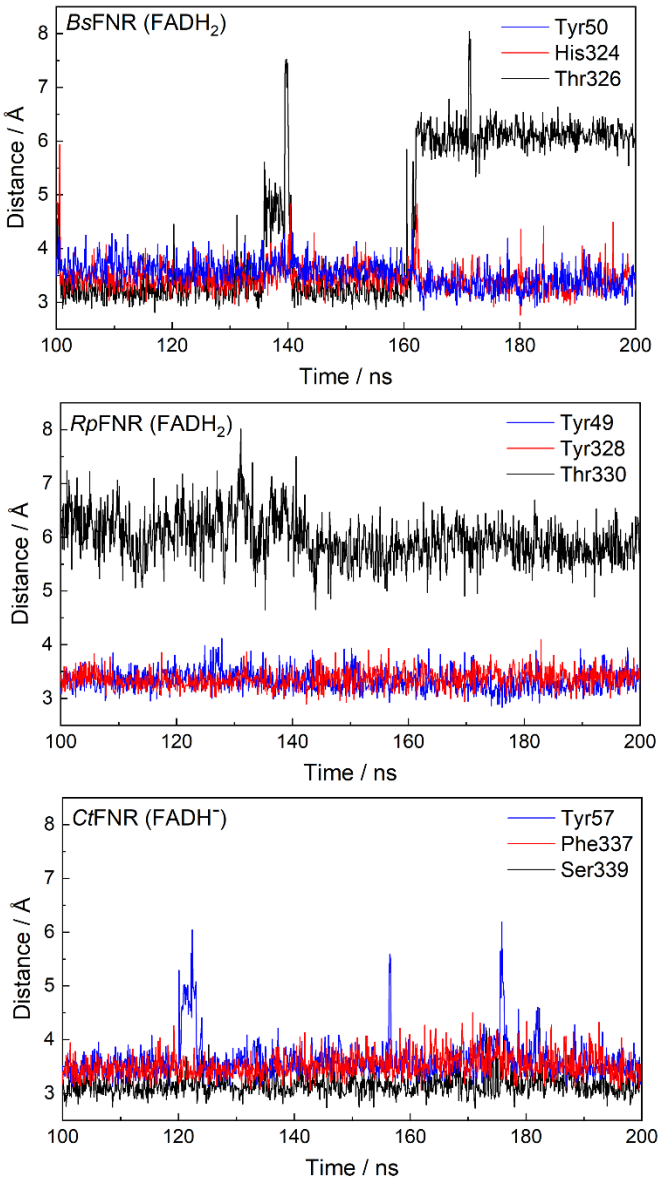

Figure 5.9 The distances between important active-site residues and the flavin rings during the MD simulations of fully reduced *Bs*FNR (*top*), *Rp*FNR (*middle*), and *Ct*FNR (*bottom*) respectively. For threonine and serine, distances between the N5 atom of the flavin ring and the O atom of the hydroxyl groups of the residues are given, while for histidine, tyrosine and phenylalanine minimum ring-to-ring distance are used.

In the simulations of *Bs*FNR, we mainly sampled two representative active-site configurations (Figure 5.10, *top* panel; note that the C-terminal extension in *Bs*FNR is much shorter than those in *Ct*FNR and *Rp*FNR). In one configuration Thr326 remains interacting with the N5 atom of the flavin ring and the whole C-terminal extension stays close to the cofactor, similar to that in *Ct*FNR; in the alternative configuration, however, Thr326 moves away, and the C-terminal extension switches its orientation and opens up the active site (Figure 5.9, *top* panel), comparable to the conformation observed in *Rp*FNR.

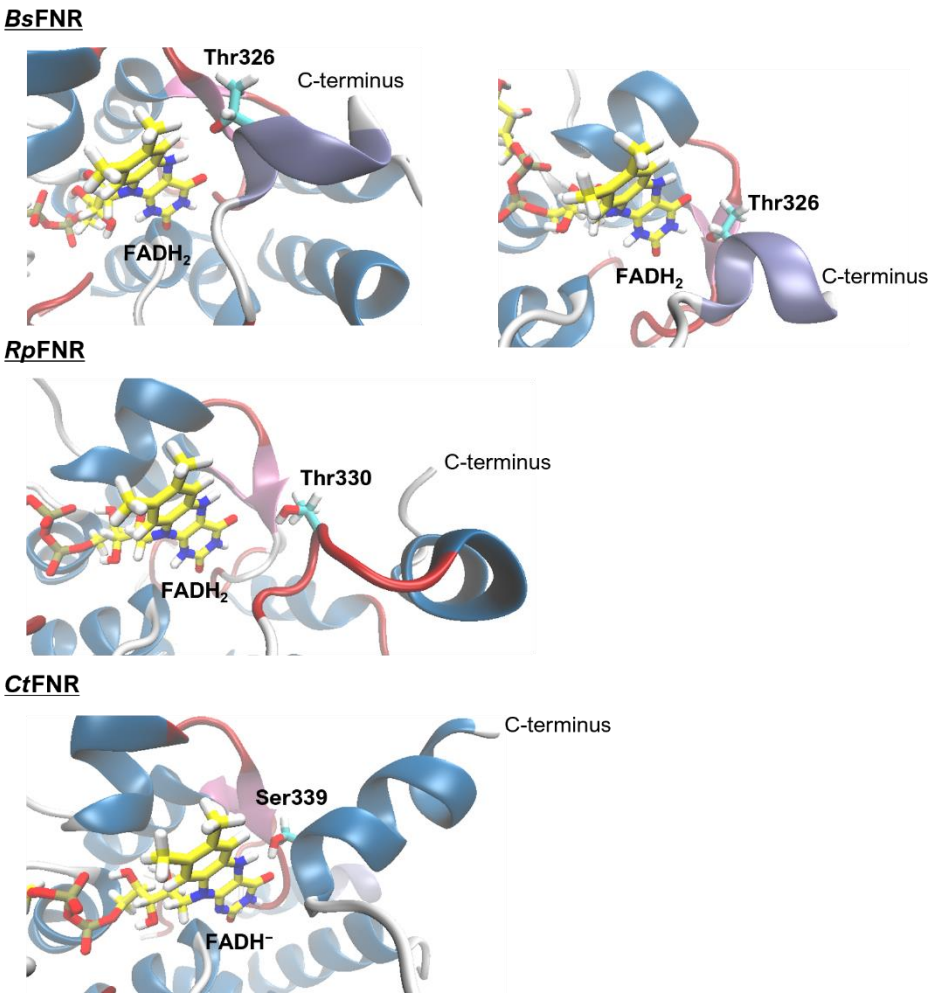

Figure 5.10 Selected snapshots from the MD simulations of fully reduced *Bs*FNR (*top*), *Rp*FNR (*middle*) and *Ct*FNR (*bottom*).

The results of these simulations are generally consistent with our experimental findings. The extremely fast excited-state decays of $FADH_2$ in *Bs*FNR and *Rp*FNR (with transient absorption spectra similar to that of $FADH_2$ in solution) can be rationalized by a lack of constraints from the C-terminal extension and a highly solvent-exposed active site. In *Ct*FNR the closer interactions between the C-terminal extension and $FADH^-$ provide a rigid environment that hinders the radiationless decay pathway of the excited state. Nevertheless, it should be noted that such analysis based on ground-state geometries is rather qualitative, as two protonation states are involved, and we did not evaluate the exact nature of the involved potential energy surfaces and the position of the CI (which are very likely to be very different for $FADH^-$ and $FADH_2$).

Furthermore, in *Bs*FNR, in those conformations where FAD_{red} closely interacts with the threonine residue, a pK_a shift of FAD_{red} may be expected, which correlates with our

observations that at pH 7.0, FAD_{red} in *Bs*FNR presents as a mixture of two protonation states, whereas in *Rp*FNR and *Ct*FNR predominantly FAD_{red} exists as single species (in neutral and anionic forms, respectively).

5.4 Concluding remarks

Based on time-resolved spectral characterization of the excited-state of FAD_{red} in three TrxR-type FNRs, *Bs*FNR, *Ct*FNR and *Rp*FNR, we elucidate the protonation states of FAD_{red} in these proteins: at neutral pH (pH 7.0), FAD_{red} in *Ct*FNR exists in the anionic form $FADH^-$, and that in *Rp*FNR exists in the neutral form $FADH_2$. For *Bs*FNR, we argue that both forms coexist at this pH condition with $FADH_2$ being the majority.

Furthermore, our results also provide useful insight into the active-site configurations of these FNRs in the fully reduced state. Strong constraints from the local environment are expected for $FADH^-$ in *Ct*FNR given its relatively long-lived excited state. On the other hand, the active sites of *Bs*FNR (for the $FADH_2$ containing fraction) and *Rp*FNR are expected to be more flexible and possibly highly solvent exposed. These assessments are further corroborated by MD simulations, which reveal contrasting behaviors of the C-terminal extensions in the three FNRs. However, it should be noted that the current conclusions are drawn from the single simulations of 200 ns, and we plan on a more comprehensive conformational study in future.

The difference in the protonation state of the fully reduced cofactor, as well as the active-site configurations of the enzymes in the fully reduced state, may account for the differences in the reactivity between FAD_{red} and $NADP^+$ in the three FNRs. It is also possible that these two factors are actually interdependent and other factors may also be involved such as the motions of the $NADP^+$-binding domain and its interactions with the FAD-binding domain.[60] In this respect, we note that a previous study on variants of *Ct*FNR with the C-terminal extension truncated has demonstrated that the deletion of C-terminal residues significantly alters neither the absorption spectrum of FAD_{red} ($FADH^-$ here) nor its reaction kinetics with $NADP^+$,[160] yet such experiments are lacking for systems here identified as bearing $FADH_2$. Future time-resolved spectroscopic experiments on these systems may further help understand the structure–function correlations in TrxR-type FNR.

It appears that the time-resolved spectral characterization of protein-bound fully reduced flavins reported in the literature thus far has been limited to the anionic forms (or more strictly, with the anionic forms as the major fraction), including those in lactate oxidase, D- and L-amino acid oxidase, flavodoxin,[17] DNA photolyase[16], GOX, the flavodehydrogenase

component from flavocytochrome b_2[18] and ThyX.[157] Here we provide a report on the excited-state properties of protein-bound $FADH_2$. It appears that, intrinsically, $FADH_2$ has a shorter excited-state lifetime, as well as a much more red-shifted emission spectrum compared with that of $FADH^-$. Such features may provide an alternative approach (to e.g., NMR) for determining the protonation state of fully reduced flavins in proteins, although further verification in other systems that can stabilize the neutral forms of fully reduced flavins (an interesting system would be TrxR[161]) is also warranted.

Finally, it is also worth noting that the lowest transition band ($S_0 \rightarrow S_1$ transition) in the steady-state absorption spectra of $FADH_2$ in *Bs*FNR and *Rp*FNR is significantly red-shifted (~50 nm compared with that in solution and ~20 nm compared with that in spinach FNR). Such red-shift does not manifest in the excited state as the transient absorption spectra ($S_1 \rightarrow S_n$ transition, ignoring the small contributions from the GSB and SE) and time-resolved fluorescence emission spectra ($S_1 \rightarrow S_0$ transition) of $FADH_2$ in *Bs*FNR and *Rp*FNR highly resemble those of free $FADH_2$ in solution (Figure 5.4 and 5.6). This seems to suggest that the ground-state potential energy surface of $FADH_2$ in *Bs*FNR and *Rp*FNR are likely to be deformed compared with that of free $FADH_2$, but the excited-states potential energy surfaces are relatively similar. One may speculate that near the Frank-Condon (FC) region of S_0 minimum, the geometries of free and *Bs*FNR-, *Rp*FNR-bound $FADH_2$ may be very different but those near the FC region of S_1 minimum are alike.

It has been put forward that a planar fully reduced flavin can have red-shifted absorption bands compared with a bent one, presumably due to better delocalized π electrons over a more extended conjugated system.[6,61] Yet, this argument is at odds with FAD_{ox} in FAP, which has a bent structure, i.e., a disrupted π conjugated system, but a significantly red-shifted absorption spectrum.[29] Additionally, a recent theoretical study on the spectral properties of flavin species in CRY has given a contradicting argument that a planar structure of $FADH_2$ actually leads to a blue-shift of the spectrum.[162] In our MD simulations of *Bs*FNR and *Rp*FNR where the flavins were described by classical force fields, $FADH_2$ adopts bent conformations after the structures were fully relaxed with an average dihedral angle of ~20° (Figure. 5.10). At this point the origin of the spectral red-shift remains unclear and further calculations at higher levels of theory are required to address this issue.

Chapter 6. Photo-Switching Behavior of a Flavoenzyme–Inhibitor Complex

6.1 Steady-state properties of the FADox:MTA complex in MSOX

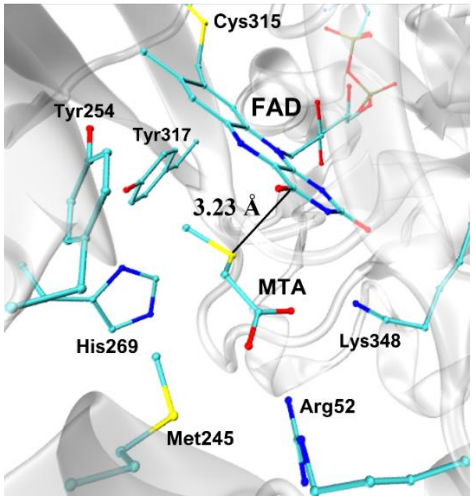

Figure 6.1 Active site in the crystal structures of MSOX from *Bacillus sp.* in complex with MTA (PDB entry: 1EL9). The distance between the S atom of methylthioacetate (MTA) and the C4 atom of the flavin ring is shown.

The ability to form CT complexes with different kinds of ligands in proteins is one of the characteristic properties of flavins,[163,164] which may have a functional role, such as regulating the midpoint potentials of flavoproteins,[165] or stabilizing small ligand molecules in the active site to enhance the overall rate of catalysis.[163] Many flavoproteins also involve reaction intermediates with CT characteristics during their catalytic cycles.[104,166,167] In this regard, investigating the photophysical properties of flavin CT complexes can be informative in understanding how substrates or inhibitors interact with flavins by CT complexation.[164,168] Moreover, although functionally irrelevant, flavin CT complexes usually exhibit significantly red-extended absorption bands that cover the whole visible range and, in some cases, can reach the near-infrared range (> 700 nm).[113,165] This may contribute to biotechnological applications that require excitation by long-wavelength excitation.[169,170] Examining the excited-state dynamics as well as photoproducts upon excitation of flavin CT complexes would allow us to explore this possibility at a molecular level. In this broader perspective, MSOX is an interesting

system as it can form CT complexes with a variety of ligands,[113] which display some unusual features in the absorption spectra that may be associated with new kinds of photophysical properties.

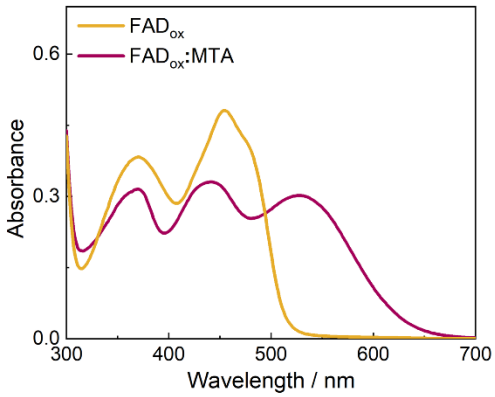

Figure 6.2 Steady-state absorption spectra of FAD_{ox} and the FAD_{ox}:MTA complex in MSOX. The complex spectrum is corrected by removing the contribution from FAD_{ox} (~15%) in the sample (see also Figure. 6.3).

MSOX is a bacterial flavoenzyme containing a FAD cofactor that is covalently bound to the protein.[171] Physiologically it catalyzes the oxidative demethylation of sarcosine (*N*-methylglycine) by molecular oxygen and water to yield glycine, hydrogen peroxide and formaldehyde, a process that does not involve light absorption.[113,172] Among the various ligands that can bind to MSOX via CT complexation, methylthioacetate (MTA) is a sarcosine analog that acts as a competitive inhibitor as it forms a redox-inactive dead-end complex with the enzyme (Figure 6.1).[113,173] The binding of MTA significantly perturbs the absorption spectrum of FAD_{ox}, leading to a new intense absorption band that is centered at 532 nm and extends to ~700 nm (Figure 6.2), presumably due to noncovalent interactions between the S atom of MTA and the aromatic isoalloxazine ring,[174,175] where the charge is delocalized from the ligand to the electron-deficient FAD_{ox}.[176]

As shown in Figure 6.3, adding MTA to the MSOX sample diminishes the overall intensity of the fluorescence emission and excitation spectra, but does not change the spectral shape. Moreover, we did not observe any emission when exciting the sample at 540 nm where the FAD_{ox}:MTA complex absorbs but the uncomplexed FAD_{ox} does not. Altogether, we ascribe the fluorescence detected in the MTA-containing MSOX sample to a small portion of uncomplexed FAD_{ox}.

The relative intensities of the fluorescence emission and excitation spectra before and after adding MTA correspond well with each other, which also allows us to estimate that under

our experimental conditions, the amount of uncomplexed FAD_{ox} in the MTA-containing sample is ~15%. Our time-resolved measurements for the FAD_{ox}:MTA complex were conducted with 520-nm and 560-nm pumps, which avoids exciting the oxidized flavin fraction, allowing us to investigate the photochemical process of the FAD_{ox}:MTA complex exclusively.

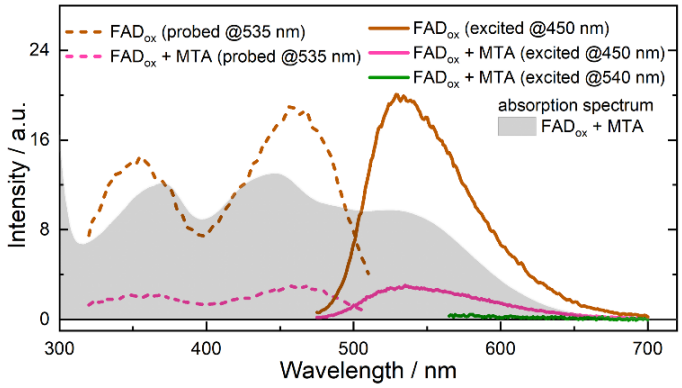

Figure 6.3 Steady-state fluorescence excitation (dashed line) and emission (solid line) spectra of the MSOX sample before and after adding 50 mM MTA (corrected for dilution). The steady-state absorption spectrum of the as-prepared MTA containing sample is shaped in grey.

6.2 Photoinduced processes of uncomplexed FADox in MSOX

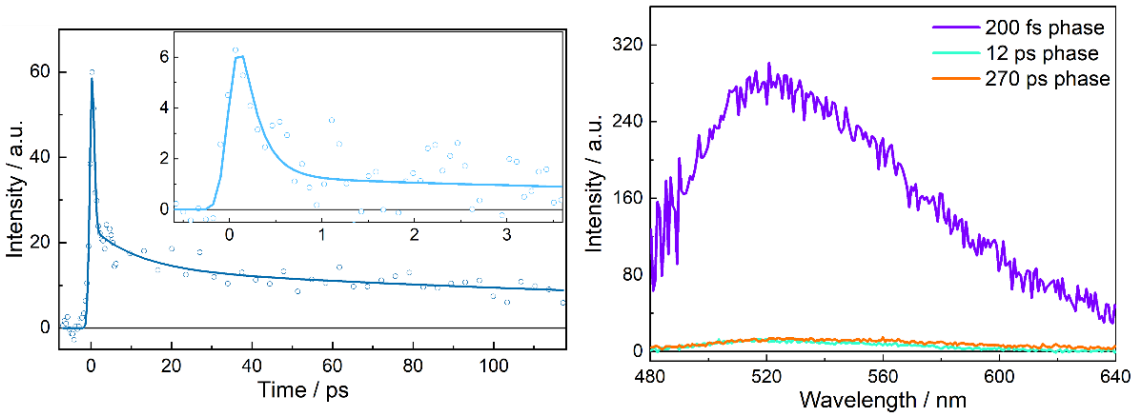

Figure 6.4 Fluorescence decays of uncomplexed FAD_{ox} in MSOX monitored at 520 nm with CS_2 or suprasil (inset) as Kerr medium (*left*), and the corresponding DAS from the global analysis (*right*).

We first investigated the excited-state dynamics and photoproduct formation of uncomplexed FAD_{ox} in MSOX using ultrafast spectroscopy. As shown in Figure 6.4, upon excitation, the fluorescence of the FAD_{ox} cofactor in MSOX predominantly decays in 200 fs (91%), indicating ultrafast fluorescence quenching by photoinduced ET from nearby residues, the self-quenching phenomenon typically observed in "non-photoactive" flavoproteins. In the active site of MSOX, several tyrosine residues are located in the vicinity of the flavin (Figure 6.5). Tyr317 is the closest (minimum ring-to-ring distance to the flavin ring: 3.38 Å) and the

most likely candidate as the initial electron donor. Minor phases with longer lifetimes can be due to the conformational heterogeneities of the protein active site and the presence of a small fraction of free flavin.

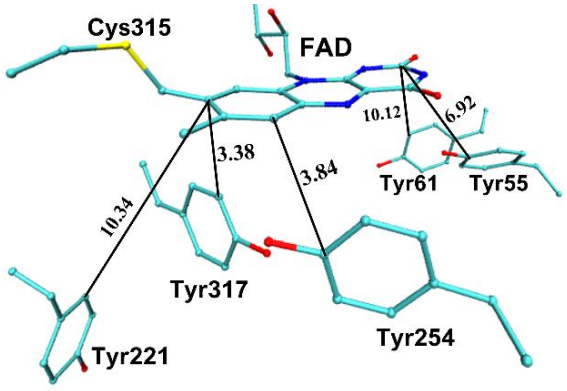

Figure 6.5 Active site in the crystal structure of MSOX from *Bacillus sp.* (PDB entry: 2GB0), featuring tyrosine residues in the close vicinity of FAD_{ox} that may act as electron donors to quench the excited FAD_{ox}. Distances are given in Å.

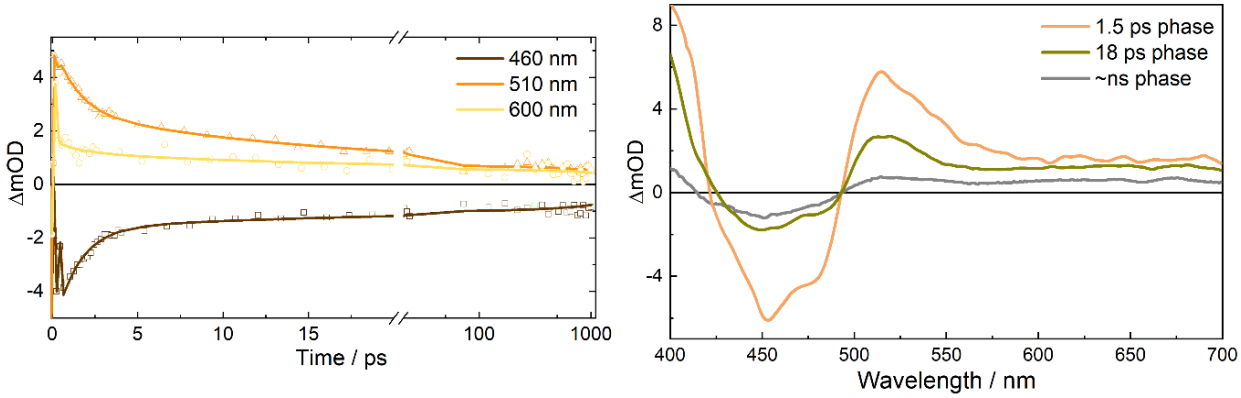

Figure 6.6 Isotropic transient absorption kinetics of uncomplexed FAD_{ox} in MSOX at selected wavelengths (*left*), and the corresponding EAS from the global analysis (*right*).

Transient absorption experiments focusing on processes occurring on a time scale > 200 fs further highlighted spectral features of the product states (Figure 6.6) that are very similar to those of $FAD^{\bullet-}$/$TyrOH^{\bullet+}$ radical pair that have been reported in other flavoprotein systems (cf. Figure 3.9).[56,98] The spectra decay in a multiphasic manner indicating heterogeneity in the radical pair states. As there are multiple tyrosines at different distances from the flavin, it is possible that stabilizing further ET reactions among the tyrosines occur, in competition with charge recombination (cf. ref. 12), leading to long-range charge separation. This may explain why in MSOX, FAD_{ox} can be easily photo-reduced to $FAD^{\bullet-}$ in the presence of external hole scavengers such as EDTA.[57,113]

6.3 Ultrafast photoinduced dissociation of the FADox:MTA complex in MSOX

The excited-state properties of the FAD_{ox}:MTA complex were then investigated using transient absorption spectroscopy, with green-light excitation pulses (maxima at 520 nm or 560 nm) to avoid exciting the small fraction of uncomplexed FAD_{ox} (see Section 6.1), where we observed very distinct photochemical processes from those of uncomplexed FAD_{ox} in MSOX.

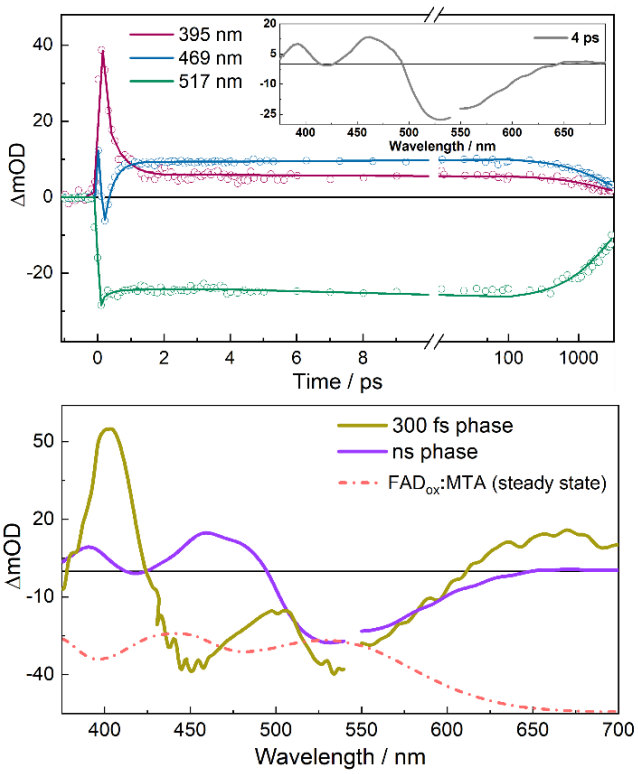

Figure 6.7 Transient absorption kinetics (*top*) of the FAD_{ox}:MTA complex at selected wavelengths upon excitation at 560 nm where the inset shows the transient spectrum recorded at 4 ps after the excitation, and the corresponding EAS (*bottom*) obtained from the global analysis where the spectra at < 550 nm and > 550 nm were obtained under 560-nm and 520-nm excitation, respectively, and the steady-state absorption spectrum of the FAD_{ox}:MTA complex is also shown for reference.

As shown in Figure 6.7, on the picosecond timescale, we observed profound ground-state bleaching (GSB) signals at ~520 nm, as well as marked positive bands at ~400 and ~470 nm suggesting the formation of photoproducts. These induced absorption features are similar to those in the ground state absorption spectrum of FAD_{ox} (Figure 6.2). Global analysis reveals that two distinct kinetic components, with time constants of 300 fs and 2.5 ns at 10 °C, are required to fit the data. The resulting EAS show that the initially populated state is characterized by a pronounced induced absorption band at ~400 nm and GSB in the 430–610 nm range. Remarkably, the spectral features of the subsequent state, which is populated in 300 fs, are almost identical to the FAD_{ox} minus FAD_{ox}:MTA difference spectrum (Fig. 6.8). This indicates

that upon initial population of the excited state in the Franck Condon (FC) region, the FAD_{ox}:MTA CT complex effectively dissociates in 300 fs, leading to the population of uncomplexed FAD_{ox}. Using $[Ru(bpy)_3]Cl_2$ as a reference, we determined the quantum yield (*QY*) of the dissociation to be ~80%. The CT complex reforms on a nanosecond timescale, and there is no other spectral evolution prior to or during this recovery. The photochemical processes of the CT complex are very distinct from those of uncomplexed FAD_{ox} in MSOX described in Section 6.2.

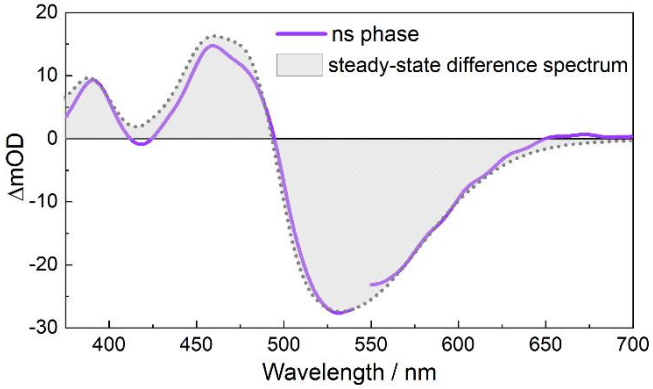

Figure 6.8 Comparison of the ns-phase EAS with the steady-state difference spectrum that corresponds to dissociation of the FAD_{ox}:MTA complex. The spectra are normalized on the minima of the bleaching bands.

6.4 Temperature dependent kinetics of the complex reformation

We then investigated the effect of temperature on the involved processes in the range from 5 to 30 °C. Whereas there is no noticeable temperature dependence on the sub-picosecond phase, consistent with a barrierless excited-state relaxation, the rate of the long-lived phase is markedly temperature dependent (Figure 6.9, *left* panel). As the temperature increases, it exhibits a faster decay, indicating that the reformation of the FAD_{ox}:MTA complex is a thermally activated process. The effect of temperature on the rate of the complex reformation is further analyzed by fitting to the Arrhenius equation:

$$\ln(k) = \ln(A) - \frac{E_a}{R}\left(\frac{1}{T}\right) \qquad (6.1)$$

where k is the rate constant, A is the pre-exponential factor, E_a is the activation energy, R is the gas constant, and T is the absolute temperature. For a single rate-limited thermally activated process, an Arrhenius plot is expected to give a straight line, and E_a can be determined from the slope of the plot. The resulting Arrhenius plot (*right* panel of Figure 6.9) gives an E_a of 28 ± 4 kJ/mol.

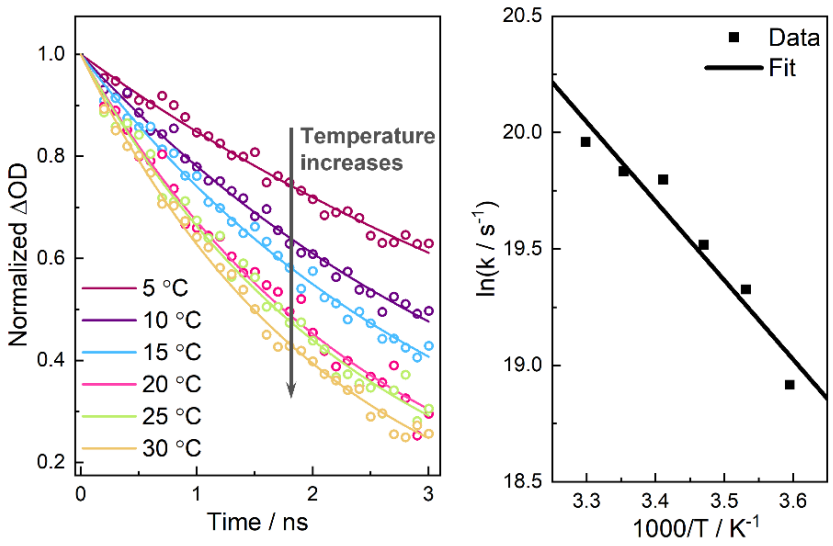

Figure 6.9 Temperature dependence of decay kinetics at 456 nm, where data on the ps–ns timescales were fitted with single-exponential decays to obtain the reaction rates (*left*), and the corresponding Arrhenius plot (*right*).

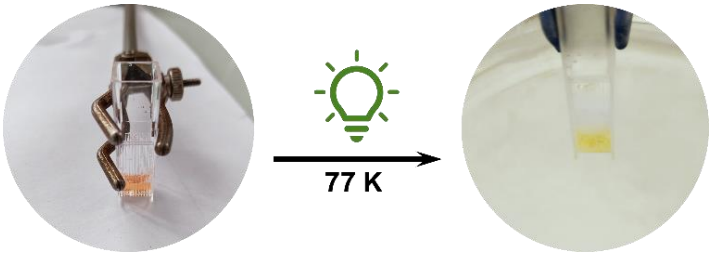

Figure 6.10 Sample prepared in the FAD_{ox}:MTA complexing state before (*left*) and after (*right*) continuous green-light illumination at 77 K.

Moreover, extrapolation of the Arrhenius plot suggests that at 77 K the complex should remain in the dissociated form (> ~100 hours). Indeed, as shown in Figure 6.10, we observed that when a sample containing the pinkish FAD_{ox}:MTA complex immersed in liquid N_2, was illuminated with a CW green laser at 532 nm, it quasi-permanently switched color to yellow (uncomplexed FAD_{ox}). When the sample was later placed at room temperature, its color gradually turned back to pinkish during the warming process.

6.5 Photo-isomerization of MTA in the active site

CT complex formation occurs on the order of a few milliseconds at 5°C.[173] Yet, at near-physiological temperatures, the recovery of the complex upon photodissociation occurs on the nanosecond timescale. Therefore, it is evident that throughout the photoinduced processes, MTA must remain in the protein. Considering the modest energy barrier (~28 kJ/mol), the most likely explanation for our observations is that, upon excitation, MTA undergoes a conformational change in the active site, and in the resulting intermediate state the strong

noncovalent interactions between the S atom of MTA and the flavin ring are abolished, resulting in the GSB of the CT complex and appearance of a pure FAD_{ox} spectrum.

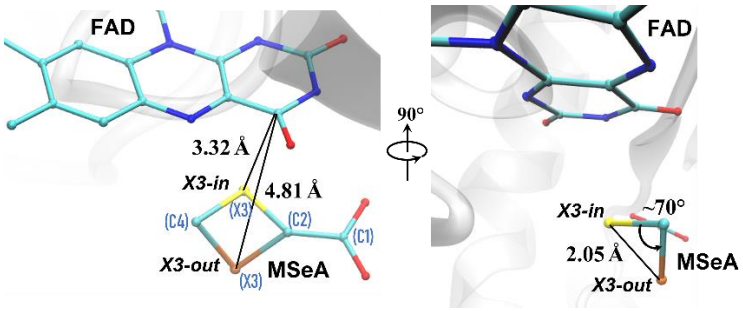

Figure 6.11 Two distinct conformations of MSeA (*X3-in* and *X3-out*) in the active site of MSOX (PDB entry: 1EL8).

In addition to MTA, MSOX can also bind methylselenoacetate (MSeA) and methyltelluroacetate (MTeA) by CT complexation, where the S atom of MTA is replaced by Se and Te, respectively.[113] The corresponding absorption bands are red-shifted compared with that of the FAD_{ox}:MTA complex (Te > Se > S), in agreement with CT interactions between the X atom (X = S, Se, Te) of the inhibitors and the flavin ring, as X is a group VIa element and the polarizability increases as the atomic number increases.[113] Interestingly, in the crystal structures, MSeA and MTeA both bind to MSOX in two discrete conformations (Figure 6.11 shows those of MSeA while those of MTeA are similar).[113] In one conformation, the coplanar atoms C1–C2–X3–C4 lie nearly parallel to the flavin ring and superimpose well on the MTA structure (cf. Figure 6.1), where the X3 atom is located very close to the flavin (3.32 Å to flavin C4 atom; *X3-in* conformer). In the alternative conformation, the C2–X3–C4 plane is rotated ~70°, with the X3 atom moving away from the flavin (4.81 Å to flavin C4 atom; *X3-out* conformer), with the remaining inhibitor atoms essentially staying at the same positions. Given the structural similarity between MTA, MSeA and MTeA, we propose that MTA can also adopt the two discrete conformations (*X3-in* and *X3-out*) in MSOX. It predominantly adopts the *X3-in* conformation in the steady state; absorbing a photon causes MTA to switch from the *X3-in* to the *X3-out* conformation, via a crossing region on the potential energy surfaces of the excited state and the *X3-out* ground state. It then converts back to the *X3-in* conformation by a thermally activated transition. The proposed reaction pathways are depicted in Figure 6.12, along with the involved energetics and time constants. In this scheme, the reaction coordinate thus involves isomerization of the MTA ligand.

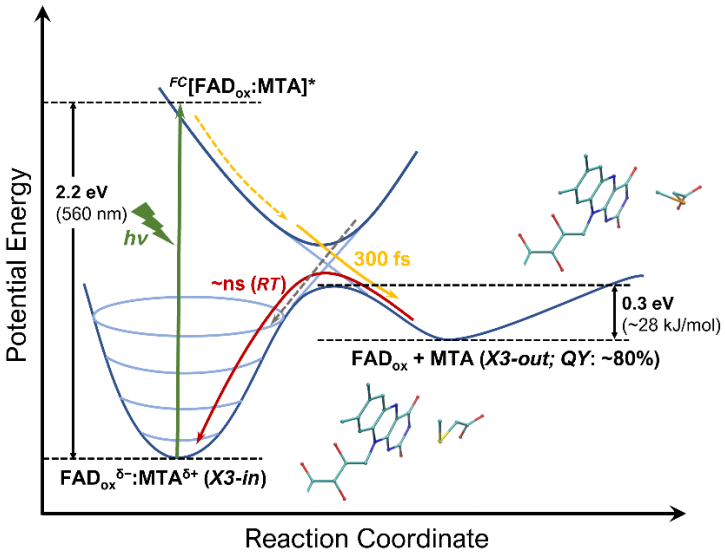

Figure 6.12 Proposed reaction pathways following the excitation of the FAD_{ox}:MTA complex in MSOX. *RT*: room temperature.

We expect that similar photo-switching reactions may also take place in the FAD_{ox}:MSeA and FAD_{ox}:MTeA complexes. Whereas MTA can efficiently flip back to the *X3-in* conformation on a nanosecond timescale near room temperature, after photo-switching the larger and heavier Se and Te atoms may induce more steric effects to trap MSeA and MTeA in the *X3-out* conformation (corresponding to larger activation energies for back flipping). On the other hand, the FAD_{ox}:MSeA and FAD_{ox}:MTeA complexes exhibit broader and more intense absorption bands,[113] suggesting that photo-switching can be triggered more easily. In the crystal structures of the MSOX–MSeA and MSOX–MTeA complexes, the presence of two discrete conformations of the inhibitors may be due to photoisomerization to the *X3-out* conformation induced by ambient light during the crystallographic study, which was performed at 100 K (whereas the lifetime of the *X3-out* conformation of MTA at 100 K is estimated to be only ~14 seconds from extrapolating the Arrhenius plot of Figure 6.9). Another possibility is that the photo-switching phenomenon can also be induced by X-ray absorption, similar to what has been reported in the photo-switchable protein bacteriorhodopsin.[177] In the crystal structures, the relative occupancies of the *X3-out* conformation are 0.35 and 0.50 for MSeA and MTeA, respectively,[113] the order of which is consistent with our assessment that the activation energy of the back-switching to the *X3-in* conformation should increase as the size of the X3 atom increases.

6.6 Concluding remarks

In summary, we have presented for the first time a full spectral investigation of excited-state and photoproduct properties of a flavin CT complex, the FAD_{ox}:MTA complex in MSOX. We show that upon green-light excitation, the FAD_{ox}:MTA complex dissociates in a barrierless way in 300 fs following the relaxation of the excited state, and recombines on nanosecond timescales near physiological temperatures. We assign these processes to MTA switching between two isomers that involve the movement of the S atom. Our results also provide direct evidence demonstrating that upon excitation of the FAD_{ox}:MTA complex, the charge displaces from flavin to the ligand, the opposite direction to the charge transfer in the ground state of the complex. This assessment is distinct from many other cases where exciting a CT band is believed to lead to complete charge separation,[168,178,179] in the same direction as the ground-state charge delocalization. Furthermore, an interesting parallel can be made with ultrafast photooxidation of protein-bound $FAD^{\bullet-}$ described in **Chapter 4**, where FAD_{ox} is transiently formed through ET presumably to a close-by cationic residue. Thus, although mostly occurring as the resting form in flavoproteins, under certain circumstances FAD_{ox} can also be a short-lived reaction intermediate. We anticipate that our findings will open a new avenue for the exploration of flavin photochemistry with ultimately possible practical implications as photo-switches and optogenetic tools.

Chapter 7. Conclusions and Perspectives

Flavins are among the most versatile redox cofactors in nature and can participate in photochemical reactions. In this thesis, combining ultrafast spectroscopies and multiple computational approaches several fundamental processes in the photochemistry of flavoproteins have been investigated in depth.

We first revisited the well-documented photoreduction of oxidized flavins in variants of a Ferredoxin $NADP^+$ Reductase (FNR) model system, *Bs*FNR, in which, unlike most of the preceding studies, the involved electron donors can be unambiguously identified from a structural perspective. The photoinduced $FAD^{\bullet-}/TyrOH^{\bullet+}$ and $FAD^{\bullet-}/TrpH^{\bullet+}$ radical pairs in WT and Y50W *Bs*FNR were found to form in ~200 fs, an order of magnitude faster than the decay by charge recombination (a few picoseconds), allowing us to straightforwardly characterize of the reaction intermediates in the charge-separated state. Based on MD simulations and QM/MM calculations, the experimental findings were further explored to obtain detailed insights into the spectral properties of interacting radical intermediates in a protein environment. This approach is likely to enhance understanding of the nature of photoproducts of other oxidized flavoproteins.

The photophysical properties of anionic semi-reduced flavin radicals were largely unknown despite their importance in numerous biochemical reactions. We conducted a systematic study on the photoproducts of anionic flavin radicals in several flavoprotein oxidases where they can be stabilized. We established that their excitation, in either of two distinct absorption bands in the visible/near ultraviolet range, invariably results in oxidation of the anionic flavin radicals on a time scale less than ~100 fs. The thus generated oxidized flavin photoproducts decay back to the anionic radical form in 10–20 ps. We propose that this process may constitute an excited-state deactivation pathway for protein-bound anionic flavin radicals in general. The identity of potential electron acceptors and the energetics involved were investigated by multiple computational approaches. The positively charged active-site residues histidine and arginine, which are thought to play an important role in stabilizing catalytic reaction intermediates, were demonstrated to be the mostly likely electron acceptor.

In the study of the excited-state properties of fully reduced flavins in three TrxR-type FNRs, we recorded unprecedentedly fast excited-state decays of protein-bound fully reduced flavins in *Bs*FNR and *Rp*FNR (in 6 and 8 ps, respectively), whereas that in *Ct*FNR decays in 400 ps. The molecular origins of these observations were demonstrated to be the differences in the protonation states of the fully reduced cofactors, as well as different degrees of constraints from the protein active sites, in the investigated systems. Together with the results of MD simulations, our findings also provide insight into the active-site configurations of these FNRs in the fully reduced state with useful catalytic implications.

Furthermore, we presented the first full-spectral investigation on the photochemical processes that follow the excitation of a flavin–inhibitor charge transfer complex, the FAD_{ox}:MTA complex in monomeric sarcosine oxidase. We show that upon excitation, the complex dissociates barrierlessly in ~300 fs following the relaxation of the excited state; the complex recombines on nanosecond timescales, with strikingly temperature-dependent kinetics. We assign the whole process to a photoinduced conformational changes (photo-isomerization) of the inhibitor in the protein active site followed by a thermally activated back transformation.

Altogether, we have conducted studies on protein-bound flavin species of four redox states or chemical forms. The findings described in this thesis, which include the discovery of two hitherto undocumented photochemical processes in flavoproteins, expand the repertoire of photochemistry involving flavin cofactors. This work may open new avenues for the exploration of flavin photochemistry with ultimately possible practical implications as novel photocatalysts and optogenetic tools. As a further perspective, the photophysical properties of neutral semi-reduced flavin radicals may be worth further investigation considering their red-light-absorbing nature for potential biotechnological applications. In certain cryptochromes photoreceptors this state can be accumulated under blue-light illumination, and stabilized with a lifetime as long as minutes, which is responsible for sensing red light.[13,180] So far such studies have been limited to those in DNA photolyase (functionally relevant)[22] and flavodoxin,[20,21] where excitation of the neutral flavin radicals in these proteins has been reported or suggested to extract an electron from nearby aromatic residues (so far only tryptophan has been spectroscopically identified)[10,19] and be photoreduced to the fully reduced forms, and glucose oxidase, where no photoproducts are observed.[20] Whether tyrosine can also participate as an electron donor, as is the case for oxidized flavins, and whether there are other excited-state

decay pathways in addition to the photoreduction of neutral flavin radicals, awaits more detailed elucidations.

References

(1) Miura, R. Versatility and Specificity in Flavoenzymes: Control Mechanisms of Flavin Reactivity. *Chem. Rec.* **2001**, *1* (3), 183–194.

(2) Walsh, C. T.; Wencewicz, T. A. Flavoenzymes: Versatile Catalysts in Biosynthetic Pathways. *Nat. Prod. Rep.* **2012**, *30* (1), 175–200.

(3) Buckel, W.; Thauer, R. K. Flavin-Based Electron Bifurcation, A New Mechanism of Biological Energy Coupling. *Chem. Rev.* **2018**, *118* (7), 3862–3886.

(4) Duan, H. D.; Khan, S. A.; Miller, A. F. Photogeneration and Reactivity of Flavin Anionic Semiquinone in a Bifurcating Electron Transfer Flavoprotein. *Biochim. Biophys. Acta - Bioenerg.* **2021**, *1862* (7), 148415.

(5) Massey, V.; Palmer, G. On the Existence of Spectrally Distinct Classes of Flavoprotein Semiquinones. A New Method for the Quantitative Production of Flavoprotein Semiquinones. *Biochemistry* **1966**, *5* (10), 3181–3189.

(6) Ghisla, S.; Massey, V.; Lhoste, J.-M.; MayhewJ, S. G. Fluorescence and Optical Characteristics of Reduced Flavines and Flavoproteins. *Biochemistry* **1974**, *13* (3), 589–597.

(7) Su, D.; Pabel Kabir, M.; Orozco-Gonzalez, Y.; Gozem, S.; Gadda, G.; Su, D.; Kabir, M. P.; Orozco-Gonzalez, Y.; Gozem, S.; Gadda, G. Fluorescence Properties of Flavin Semiquinone Radicals in Nitronate Monooxygenase. *ChemBioChem* **2019**, *20*, 1646–1652.

(8) Zhong, D.; Zewail, A. H. Femtosecond Dynamics of Flavoproteins: Charge Separation and Recombination in Riboflavine (Vitamin B2)-Binding Protein and in Glucose Oxidase Enzyme. *Proc. Natl. Acad. Sci. U. S. A.* **2001**, *98* (21), 11867–11872.

(9) Nunthaboot, N.; Tanaka, F.; Kokpol, S.; Chosrowjan, H.; Taniguchi, S.; Mataga, N. Simultaneous Analysis of Ultrafast Fluorescence Decays of FMN Binding Protein and Its Mutated Proteins by Molecular Dynamic Simulation and Electron Transfer Theory. *J. Phys. Chem. B* **2008**, *112* (41), 13121–13127.

(10) Brazard, J.; Usman, A.; Lacombat, F.; Ley, C.; Martin, M. M.; Plaza, P.; Mony, L.; Heijde, M.; Zabulon, G.; Bowler, C. Spectro-Temporal Characterization of the Photoactivation Mechanism of Two New Oxidized Cryptochrome/Photolyase Photoreceptors. *J. Am. Chem. Soc.* **2010**, *132* (13), 4935–4945.

(11) Martin, R.; Lacombat, F.; Espagne, A.; Dozova, N.; Plaza, P.; Yamamoto, J.; Müller, P.; Brettel, K.; de la Lande, A. Ultrafast Flavin Photoreduction in an Oxidized Animal (6-4) Photolyase through an Unconventional Tryptophan Tetrad. *Phys. Chem. Chem. Phys.* **2017**, *19* (36), 24493–24504.

(12) Nag, L.; Lukacs, A.; Vos, M. H. Short-Lived Radical Intermediates in the Photochemistry of Glucose Oxidase. *ChemPhysChem* **2019**, *20* (14), 1793–1798.

(13) Lacombat, F.; Espagne, A.; Dozova, N.; Plaza, P.; Müller, P.; Brettel, K.; Franz-Badur, S.; Essen, L. O. Ultrafast Oxidation of a Tyrosine by Proton-Coupled Electron Transfer Promotes Light Activation of an Animal-like Cryptochrome. *J. Am. Chem. Soc.* **2019**, *141* (34), 13394–13409.

(14) Brazard, J.; Usman, A.; Lacombat, F.; Ley, C.; Martin, M. M.; Plaza, P. New Insights into the Ultrafast Photophysics of Oxidized and Reduced Fad in Solution. *J. Phys. Chem. A* **2011**, *115* (15), 3251–3262.

(15) Van den Berg, P. A. W.; Feenstra, K. A.; Mark, A. E.; Berendsen, H. J. C.; Visser, A. J. W. G. Dynamic Conformations of Flavin Adenine Dinucleotide: Simulated Molecular Dynamics of the Flavin Cofactor Related to the Time-Resolved Fluorescence Characteristics. *J. Phys. Chem. B* **2002**, *106* (34), 8858–8869.

(16) Kao, Y. T.; Saxena, C.; He, T. F.; Guo, L.; Wang, L.; Sancar, A.; Zhong, D. Ultrafast Dynamics of Flavins in Five Redox States. *J. Am. Chem. Soc.* **2008**, *130* (39), 13132–13139.

(17) Visser, A. J. W. G.; Ghisla, S.; Massey, V.; Müller, F.; Veeger, C. Fluorescence Properties of Reduced Flavins and Flavoproteins. *Eur. J. Biochem.* **1979**, *101* (1), 13–21.

(18) Enescu, M.; Lindqvist, L.; Soep, B. Excited-State Dynamics of Fully Reduced Flavins and Flavoenzymes Studied at Subpicosecond Time Resolution. *Photochem. Photobiol.* **1998**, *68* (2), 150–156.

(19) Aubert, C.; Vos, M. H.; Mathis, P.; Eker, A. P. M.; Brettel, K. Intra-Protein Radical Transfer during Photoactivation of DNA Photolyase. *Nature* **2000**, *405*, 586–590.

(20) Pan, J.; Byrdin, M.; Aubert, C.; Eker, A. P. M.; Brettel, K.; Vos, M. H. Excited-State Properties of Flavin Radicals in Flavoproteins: Femtosecond Spectroscopy of DNA Photolyase, Glucose Oxidase, and Flavodoxin. *J. Phys. Chem. B* **2004**, *108* (28), 10160–10167.

(21) Kundu, M.; He, T. F.; Lu, Y.; Wang, L.; Zhong, D. Short-Range Electron Transfer in Reduced Flavodoxin: Ultrafast Nonequilibrium Dynamics Coupled with Protein Fluctuations. *J. Phys. Chem. Lett.* **2018**, *9* (11), 2782–2790.

(22) Lukacs, A.; Eker, A. P. M.; Byrdin, M.; Brettel, K.; Vos, M. H. Electron Hopping through the 15 Å Triple Tryptophan Molecular Wire in DNA Photolyase Occurs within 30 Ps. *J. Am. Chem. Soc.* **2008**, *130* (44), 14394–14395.

(23) Kao, Y.-T.; Tan, C.; Song, S.-H.; Ztürk, N. O. ¨; Li, J.; Wang, L.; Sancar, A.; Zhong, D. Ultrafast Dynamics and Anionic Active States of the Flavin Cofactor in Cryptochrome and Photolyase. *J. Am. Chem. Soc.* **2008**, *130* (24), 7695–7701.

(24) Ghanem, M.; Fan, F.; Francis, K.; Gadda, G. Spectroscopic and Kinetic Properties of Recombinant Choline Oxidase from Arthrobacter Globiformis. *Biochemistry* **2003**, *42* (51), 15179–15188.

(25) Losi, A.; Gärtner, W. The Evolution of Flavin-Binding Photoreceptors: An Ancient Chromophore Serving Trendy Blue-Light Sensors. *Annu. Rev. Plant Biol.* **2012**, *63*, 49–72.

(26) Christie, J. M.; Gawthorne, J.; Young, G.; Fraser, N. J.; Roe, A. J. LOV to BLUF: Flavoprotein Contributions to the Optogenetic Toolkit. *Mol. Plant* **2012**, *5* (3), 533–

544.

(27) Gil, A. A.; Carrasco-López, C.; Zhu, L.; Zhao, E. M.; Ravindran, P. T.; Wilson, M. Z.; Goglia, A. G.; Avalos, J. L.; Toettcher, J. E. Optogenetic Control of Protein Binding Using Light-Switchable Nanobodies. *Nat. Commun.* **2020**, *11* (1), 1–12.

(28) Sorigué, D.; Légeret, B.; Cuiné, S.; Blangy, S.; Moulin, S.; Billon, E.; Richaud, P.; Brugière, S.; Couté, Y.; Nurizzo, D.; Müller, P.; Brettel, K.; Pignol, D.; Arnoux, P.; Li-Beisson, Y.; Peltier, G.; Beisson, F. An Algal Photoenzyme Converts Fatty Acids to Hydrocarbons. *Science* **2017**, *357* (6354), 903–907.

(29) Sorigué, D.; Hadjidemetriou, K.; Blangy, S.; Gotthard, G.; Bonvalet, A.; Coquelle, N.; Samire, P.; Aleksandrov, A.; Antonucci, L.; Benachir, A.; Boutet, S.; Byrdin, M.; Cammarata, M.; Carbajo, S.; Cuiné, S.; Doak, R. B.; Foucar, L.; Gorel, A.; Grünbein, M.; Hartmann, E.; Hienerwadel, R.; Hilpert, M.; Kloos, M.; Lane, T. J.; Légeret, B.; Legrand, P.; Li-Beisson, Y.; Moulin, S. L. Y.; Nurizzo, D.; Peltier, G.; Schirò, G.; Shoeman, R. L.; Sliwa, M.; Solinas, X.; Zhuang, B.; Barends, T. R. M.; Colletier, J.-P.; Joffre, M.; Royant, A.; Berthomieu, C.; Weik, M.; Domratcheva, T.; Brettel, K.; Vos, M. H.; Schlichting, I.; Arnoux, P.; Müller, P.; Beisson, F. Mechanism and Dynamics of Fatty Acid Photodecarboxylase. *Science* **2021**, *372* (6538), eabd5687.

(30) Hedison, T. M.; Heyes, D. J.; Scrutton, N. S. Making Molecules with Photodecarboxylases: A Great Start or a False Dawn? *Curr. Res. Chem. Biol.* **2022**, *2*, 100017.

(31) Mataga, N.; Chosrowjan, H.; Shibata, Y.; Tanaka, F.; Nishina, Y.; Shiga, K. Dynamics and Mechanisms of Ultrafast Fluorescence Quenching Reactions of Flavin Chromophores in Protein Nanospace. *J. Phys. Chem. B* **2000**, *104* (45), 10667–10677.

(32) Zhong, D.; Zewail, A. H. Femtosecond Dynamics of Flavoproteins: Charge Separation and Recombination in Rioboflavin (Vitamin B2)-Binding Protein and in Glucose Oxidase Enzyme. *Proc. Natl. Acad. Sci. U.S.A.* **2001**, *98*, 11867–11872.

(33) Tanaka, F.; Rujkorakarn, R.; Chosrowjan, H.; Taniguchi, S.; Mataga, N. Analyses of Donor–Acceptor Distance-Dependent Rates of Photo-Induced Electron Transfer in Flavoproteins with Three Kinds of Electron Transfer Theories. *Chem. Phys.* **2008**, *348* (1–3), 237–241.

(34) Laptenok, S. P.; Bouzhir-Sima, L.; Lambry, J. C.; Myllykallio, H.; Liebl, U.; Vos, M. H. Ultrafast Real-Time Visualization of Active Site Flexibility of Flavoenzyme Thymidylate Synthase ThyX. *Proc. Natl. Acad. Sci. U. S. A.* **2013**, *110* (22), 8924–8929.

(35) Bialas, C.; Barnard, D. T.; Auman, D. B.; Mcbride, R. A.; Jarocha, L. E.; Hore, P. J.; Dutton, P. L.; Stanley, R. J.; Moser, C. C. Ultrafast Flavin/Tryptophan Radical Pair Kinetics in a Magnetically Sensitive Artificial Protein. *Phys. Chem. Chem. Phys* **2019**, *21*, 13453.

(36) Yang, H.; Luo, G.; Karnchanaphanurach, P.; Louie, T.-M.; Rech, I.; Cova, S.; Xun, L.; Xie, X. S. Protein Conformational Dynamics Probed by Single-Molecule Electron Transfer. *Science* **2003**, *302* (5643), 262–266.

(37) Zhuang, B.; Nag, L.; Sournia, P.; Croitoru, A.; Ramodiharilafy, R.; Lambry, J.-C.; Myllykallio, H.; Aleksandrov, A.; Liebl, U.; Vos, M. H. Photochemical Processes in Flavo-Enzymes as a Probe for Active Site Dynamics: TrmFO of Thermus

Thermophilus. *Photochem. Photobiol. Sci.* **2021**, *20* (5), 663–670.

(38) Marcus, R. A.; Sutin, N. Electron Transfers in Chemistry and Biology. *Biochim. Biophys. Acta - Rev. Bioenerg.* **1985**, *811* (3), 265–322.

(39) Page, C. C.; Moser, C. C.; Chen, X.; Dutton, P. L. Natural Engineering Principles of Electron Tunnelling in Biological Oxidation–Reduction. *Nature* **1999**, *402* (6757), 47–52.

(40) Baier, J.; Maisch, T.; Maier, M.; Engel, E.; Landthaler, M.; Bäumler, W. Singlet Oxygen Generation by UVA Light Exposure of Endogenous Photosensitizers. *Biophys. J.* **2006**, *91* (4), 1452–1459.

(41) Ernst, S.; Rovida, S.; Mattevi, A.; Fetzner, S.; Drees, S. L. Photoinduced Monooxygenation Involving NAD(P)H-FAD Sequential Single-Electron Transfer. *Nat. Commun.* **2020**, *11* (1), 1–11.

(42) Zhuang, B.; Liebl, U.; Vos, M. H. Flavoprotein Photochemistry: Fundamental Processes and Photocatalytic Perspectives. *J. Phys. Chem. B* **2022**, *126* (17), 3199–3207.

(43) Brettel, K.; Byrdin, M. Reaction Mechanisms of DNA Photolyase. *Curr. Opin. Struct. Biol.* **2010**, *20* (6), 693–701.

(44) Lukacs, A.; Zhao, R. K.; Haigney, A.; Brust, R.; Greetham, G. M.; Towrie, M.; Tonge, P. J.; Meech, S. R. Excited State Structure and Dynamics of the Neutral and Anionic Flavin Radical Revealed by Ultrafast Transient Mid-IR to Visible Spectroscopy. *J. Phys. Chem. B* **2012**, *116* (20), 5810–5818.

(45) Kennis, J. T. M.; Crosson, S.; Gauden, M.; Van Stokkum, I. H. M.; Moffat, K.; Van Grondelle, R. Primary Reactions of the LOV2 Domain of Phototropin, a Plant Blue-Light Photoreceptor. *Biochemistry* **2003**, *42* (12), 3385–3392.

(46) Swartz, T. E.; Corchnoy, S. B.; Christie, J. M.; Lewis, J. W.; Szundi, I.; Briggs, W. R.; Bogomolni, R. A. The Photocycle of a Flavin-Binding Domain of the Blue Light Photoreceptor Phototropin. *J. Biol. Chem.* **2001**, *276* (39), 36493–36500.

(47) Iuliano, J. N.; Collado, J. T.; Gil, A. A.; Ravindran, P. T.; Lukacs, A.; Shin, S.; Woroniecka, H. A.; Adamczyk, K.; Aramini, J. M.; Edupuganti, U. R.; Hall, C. R.; Greetham, G. M.; Sazanovich, I. V.; Clark, I. P.; Daryaee, T.; Toettcher, J. E.; French, J. B.; Gardner, K. H.; Simmerling, C. L.; Meech, S. R.; Tonge, P. J. Unraveling the Mechanism of a LOV Domain Optogenetic Sensor: A Glutamine Lever Induces Unfolding of the Jα Helix. *ACS Chem. Biol.* **2020**, *15* (10), 2752–2765.

(48) Xu, J.; Jarocha, L. E.; Zollitsch, T.; Konowalczyk, M.; Henbest, K. B.; Richert, S.; Golesworthy, M. J.; Schmidt, J.; Déjean, V.; Sowood, D. J. C.; Bassetto, M.; Luo, J.; Walton, J. R.; Fleming, J.; Wei, Y.; Pitcher, T. L.; Moise, G.; Herrmann, M.; Yin, H.; Wu, H.; Bartölke, R.; Käsehagen, S. J.; Horst, S.; Dautaj, G.; Murton, P. D. F.; Gehrckens, A. S.; Chelliah, Y.; Takahashi, J. S.; Koch, K. W.; Weber, S.; Solov'yov, I. A.; Xie, C.; Mackenzie, S. R.; Timmel, C. R.; Mouritsen, H.; Hore, P. J. Magnetic Sensitivity of Cryptochrome 4 from a Migratory Songbird. *Nature* **2021**, *594* (7864), 535–540.

(49) Domratcheva, T. Neutral Histidine and Photoinduced Electron Transfer in DNA Photolyases. *J. Am. Chem. Soc.* **2011**, *133* (45), 18172–18182.

(50) Biegasiewicz, K. F.; Cooper, S. J.; Gao, X.; Oblinsky, D. G.; Kim, J. H.; Garfinkle, S. E.; Joyce, L. A.; Sandoval, B. A.; Scholes, G. D.; Hyster, T. K. Photoexcitation of Flavoenzymes Enables a Stereoselective Radical Cyclization. *Science* **2019**, *364* (6446), 1166–1169.

(51) Huang, X.; Wang, B.; Wang, Y.; Jiang, G.; Feng, J.; Zhao, H. Photoenzymatic Enantioselective Intermolecular Radical Hydroalkylation. *Nature* **2020**, *584* (7819), 69–74.

(52) Cailliez, F.; Müller, P.; Firmino, T.; Pernot, P.; De La Lande, A. Energetics of Photoinduced Charge Migration within the Tryptophan Tetrad of an Animal (6-4) Photolyase. *J. Am. Chem. Soc.* **2016**, *138* (6), 1904–1915.

(53) Cailliez, F.; Müller, P.; Gallois, M.; De La Lande, A. ATP Binding and Aspartate Protonation Enhance Photoinduced Electron Transfer in Plant Cryptochrome. *J. Am. Chem. Soc.* **2014**, *136* (37), 12974–12986.

(54) Zanetti-Polzi, L.; Aschi, M.; Amadei, A.; Daidone, I. Alternative Electron-Transfer Channels Ensure Ultrafast Deactivation of Light-Induced Excited States in Riboflavin Binding Protein. *J. Phys. Chem. Lett.* **2017**, *8* (14), 3321–3327.

(55) Aleksandrov, A. A Molecular Mechanics Model for Flavins. *J. Comp. Chem.* **2019**, *40* (32), 2834–2842.

(56) Zhuang, B.; Seo, D.; Aleksandrov, A.; Vos, M. Characterization of Light-Induced, Short-Lived Interacting Radicals in the Active Site of Flavoprotein Ferredoxin-NADP+ Oxidoreductase. *J. Am. Chem. Soc.* **2021**, *143* (7), 2757–2768.

(57) Zhuang, B.; Ramodiharilafy, R.; Liebl, U.; Aleksandrov, A.; Vos, M. H. Ultrafast Photooxidation of Protein-Bound Anionic Flavin Radicals. *Proc. Natl. Acad. Sci.* **2022**, *119* (8), e2118924119.

(58) Zhuang, B.; Vos, M. H. Photoswitching Behavior of Flavin–Inhibitor Complex in a Nonphotocatalytic Flavoenzyme. *J. Am. Chem. Soc.* **2022**, *144* (26), 11569–11573.

(59) Seo, D.; Naito, H.; Nishimura, E.; Sakurai, T. Replacement of Tyr50 Stacked on the Si-Face of the Isoalloxazine Ring of the Flavin Adenine Dinucleotide Prosthetic Group Modulates Bacillus Subtilis Ferredoxin-NADP+ Oxidoreductase Activity toward NADPH. *Photosynth. Res.* **2015**, *125* (1), 321–328.

(60) Seo, D.; Muraki, N.; Kurisu, G. Kinetic and Structural Insight into a Role of the Re-Face Tyr328 Residue of the Homodimer Type Ferredoxin-NADP+ Oxidoreductase from Rhodopseudomonas Palustris in the Reaction with NADP+/NADPH. *Biochim. Biophys. Acta - Bioenerg.* **2020**, *1861* (3), 148140.

(61) Seo, D.; Kitashima, M.; Sakurai, T.; Inoue, K. Kinetics of NADP+/NADPH Reduction–Oxidation Catalyzed by the Ferredoxin-NAD(P)+ Reductase from the Green Sulfur Bacterium Chlorobaculum Tepidum. *Photosynth. Res. 2016 1301* **2016**, *130* (1), 479–489.

(62) Hense, A.; Herman, E.; Oldemeyer, S.; Kottke, T. Proton Transfer to Flavin Stabilizes the Signaling State of the Blue Light Receptor Plant Cryptochrome. *J. Biol. Chem.* **2015**, *290* (3), 1743–1751.

(63) Müller, P.; Brettel, K. [Ru(Bpy)3]2+ as a Reference in Transient Absorption Spectroscopy: Differential Absorption Coefficients for Formation of the Long-Lived

3MLCT Excited State. *Photochem. Photobiol. Sci.* **2012**, *11* (4), 632–636.

(64) Lacombat, F.; Plaza, P.; Plamont, M. A.; Espagne, A. Photoinduced Chromophore Hydration in the Fluorescent Protein Dreiklang Is Triggered by Ultrafast Excited-State Proton Transfer Coupled to a Low-Frequency Vibration. *J. Phys. Chem. Lett.* **2017**, *8* (7), 1489–1495.

(65) Snellenburg, J. J.; Laptenok, S. P.; Seger, R.; Mullen, K. M.; van Stokkum, I. H. M. Glotaran: A Java-Based Graphical User Interface for the R Package TIMP. *J. Stat. Softw.* **2012**, *49* (3).

(66) Mullen, K. M.; Van Stokkum, I. H. M. The Variable Projection Algorithm in Time-Resolved Spectroscopy, Microscopy and Mass Spectrometry Applications. *Numer. Algorithms 2008 513* **2008**, *51* (3), 319–340.

(67) Ponder, J. W.; Case, D. A. Force Fields for Protein Simulations. *Adv. Protein Chem.* **2003**, *66*, 27–85.

(68) Darden, T.; York, D.; Pedersen, L. Particle Mesh Ewald: An N·log(N) Method for Ewald Sums in Large Systems. *J. Chem. Phys.* **1993**, *98* (12), 10089–10092.

(69) Brooks, B. R.; Bruccoleri, R. E.; Olafson, B. D.; States, D. J.; Swaminathan, S.; Karplus, M. CHARMM: A Program for Macromolecular Energy, Minimization, and Dynamics Calculations. *J. Comput. Chem.* **1983**, *4* (2), 187–217.

(70) Phillips, J. C.; Braun, R.; Wang, W.; Gumbart, J.; Tajkhorshid, E.; Villa, E.; Chipot, C.; Skeel, R. D.; Kalé, L.; Schulten, K. Scalable Molecular Dynamics with NAMD. *J. Comput. Chem.* **2005**, *26* (16), 1781–1802.

(71) Huang, J.; Mackerell, A. D. CHARMM36 All-Atom Additive Protein Force Field: Validation Based on Comparison to NMR Data. *J. Comput. Chem.* **2013**, *34* (25), 2135–2145.

(72) Jorgensen, W. L.; Chandrasekhar, J.; Madura, J. D.; Impey, R. W.; Klein, M. L. Comparison of Simple Potential Functions for Simulating Liquid Water. *J. Chem. Phys.* **1983**, *79* (2), 926–935.

(73) Olsson, M. H. M.; SØndergaard, C. R.; Rostkowski, M.; Jensen, J. H. PROPKA3: Consistent Treatment of Internal and Surface Residues in Empirical p K a Predictions. *J. Chem. Theory Comput.* **2011**, *7* (2), 525–537.

(74) Berendsen, H. J. C.; Postma, J. P. M.; Gunsteren, W. F. van; DiNola, A.; Haak, J. R. Molecular Dynamics with Coupling to an External Bath. *J. Chem. Phys.* **1998**, *81* (8), 3684.

(75) Humphrey, W.; Dalke, A.; Schulten, K. VMD: Visual Molecular Dynamics. *J. Mol. Graph.* **1996**, *14* (1), 33–38.

(76) Fogolari, F.; Brigo, A.; Molinari, H. The Poisson-Boltzmann Equation for Biomolecular Electrostatics: A Tool for Structural Biology. *J. Mol. Recognit.* **2002**, *15* (6), 377–392.

(77) Ishikita, H.; Knapp, E. W. Redox Potential of Quinones in Both Electron Transfer Branches of Photosystem I. *J. Biol. Chem.* **2003**, *278* (52), 52002–52011.

(78) Simonson, T.; Carlsson, J.; Case, D. A. Proton Binding to Proteins: PKa Calculations

with Explicit and Implicit Solvent Models. *J. Am. Chem. Soc.* **2004**, *126* (13), 4167–4180.

(79) Simonson, T. Free Energy Calculations: Approximate Methods for Biological Macromolecules. *Springer Ser. Chem. Phys.* **2007**, *86*, 423–461.

(80) Alexey Aleksandrov; Simonson, T. Molecular Dynamics Simulations of the 30S Ribosomal Subunit Reveal a Preferred Tetracycline Binding Site. *J. Am. Chem. Soc.* **2008**, *130* (4), 1114–1115.

(81) Hohenberg, P.; Kohn, W. Inhomogeneous Electron Gas. *Phys. Rev.* **1964**, *136* (3B), B864.

(82) Kohn, W.; Sham, L. J. Self-Consistent Equations Including Exchange and Correlation Effects. *Phys. Rev.* **1965**, *140* (4A), A1133.

(83) Becke, A. D. A New Mixing of Hartree-Fock and Local Density-Functional Theories. *J. Chem. Phys.* **1993**, *98* (2), 1372–1377.

(84) J. Stephens, P.; J. Devlin, F.; F. Chabalowski, C.; J. Frisch, M. Ab Initio Calculation of Vibrational Absorption and Circular Dichroism Spectra Using Density Functional Force Fields. *J. Phys. Chem.* **2002**, *98* (45), 11623–11627.

(85) Krishnan, R.; Binkley, J. S.; Seeger, R.; Pople, J. A. Self-Consistent Molecular Orbital Methods. XX. A Basis Set for Correlated Wave Functions. *J. Chem. Phys.* **1980**, *72* (1), 650–654.

(86) Francl, M. M.; Pietro, W. J.; Hehre, W. J.; Binkley, J. S.; Gordon, M. S.; DeFrees, D. J.; Pople, J. A. Self-consistent Molecular Orbital Methods. XXIII. A Polarization-type Basis Set for Second-row Elements. *J. Chem. Phys.* **1998**, *77* (7), 3654.

(87) Runge, E.; Gross, E. K. U. Density-Functional Theory for Time-Dependent Systems. *Phys. Rev. Lett.* **1984**, *52* (12), 997.

(88) Neese, F. The ORCA Program System. *Wiley Interdiscip. Rev. Comput. Mol. Sci.* **2012**, *2* (1), 73–78.

(89) Weigend, F.; Ahlrichs, R. Balanced Basis Sets of Split Valence, Triple Zeta Valence and Quadruple Zeta Valence Quality for H to Rn: Design and Assessment of Accuracy. *Phys. Chem. Chem. Phys.* **2005**, *7* (18), 3297–3305.

(90) Lu, T.; Chen, F. Multiwfn: A Multifunctional Wavefunction Analyzer. *J. Comput. Chem.* **2012**, *33* (5), 580–592.

(91) Warshel, A.; Levitt, M. Theoretical Studies of Enzymic Reactions: Dielectric, Electrostatic and Steric Stabilization of the Carbonium Ion in the Reaction of Lysozyme. *J. Mol. Biol.* **1976**, *103* (2), 227–249.

(92) Senn, H. M.; Thiel, W. QM/MM Methods for Biomolecular Systems. *Angew. Chemie Int. Ed.* **2009**, *48* (7), 1198–1229.

(93) Field, M. J. The PDynamo Program for Molecular Simulations Using Hybrid Quantum Chemical and Molecular Mechanical Potentials. *J. Chem. Theory Comput.* **2008**, *4* (7), 1151–1161.

(94) Aubert, C.; Mathis, P.; Eker, A. P. M.; Brettel, K. Intraprotein Electron Transfer between Tyrosine and Tryptophan in DNA Photolyase from Anacystis Nidulans. *Proc.*

Natl. Acad. Sci. U.S.A. **1999**, *96* (10), 5423–5427.

(95) Immeln, D.; Weigel, A.; Kottke, T.; Pérez Lustres, J. L. Primary Events in the Blue Light Sensor Plant Cryptochrome: Intraprotein Electron and Proton Transfer Revealed by Femtosecond Spectroscopy. *J. Am. Chem. Soc.* **2012**, *134* (30), 12536–12546.

(96) Bialas, C.; Jarocha, L. E.; Henbest, K. B.; Zollitsch, T. M.; Kodali, G.; Timmel, C. R.; Mackenzie, S. R.; Dutton, P. L.; Moser, C. C.; Hore, P. J. Engineering an Artificial Flavoprotein Magnetosensor. *J. Am. Chem. Soc.* **2016**, *138* (51), 16584–16587.

(97) Dozova, N.; Lacombat, F.; Bou-Nader, C.; Hamdane, D.; Plaza, P. Ultrafast Photoinduced Flavin Dynamics in the Unusual Active Site of the TRNA Methyltransferase TrmFO. *Phys. Chem. Chem. Phys.* **2019**, *21* (17), 8743–8756.

(98) Nag, L.; Sournia, P.; Myllykallio, H.; Liebl, U.; Vos, M. H. Identification of the TyrOH●+ Radical Cation in the Flavoenzyme TrmFO. *J. Am. Chem. Soc.* **2017**, *139* (33), 11500–11505.

(99) Seo, D.; Kamino, K.; Inoue, K.; Sakurai, H. Purification and Characterization of Ferredoxin-NADP+ Reductase Encoded by Bacillus Subtilis YumC. *Arch. Microbiol.* **2004**, *182* (1), 80–89.

(100) Komori, H.; Seo, D.; Sakurai, T.; Higuchi, Y. Crystal Structure Analysis of Bacillus Subtilis Ferredoxin-NADP+ Oxidoreductase and the Structural Basis for Its Substrate Selectivity. *Protein Sci.* **2010**, *19* (12), 2279–2290.

(101) Gräslund, A.; Sahlin, M.; Sjöberg, B.-M. The Tyrosyl Free Radical in Ribonucleotide Reductase. *Env. Heal. Persp.* **1985**, *64*, 139–149.

(102) Müller, P.; Bouly, J.-P.; Hitomi, K.; Balland, V.; Getzoff, E. D.; Ritz, T.; Brettel, K. ATP Binding Turns Plant Cryptochrome Into an Efficient Natural Photoswitch. *Sci. Rep.* **2014**, *4*, 5175.

(103) Solar, S.; Getoff, N.; Surdhar, P. S.; Armstrong, D. A.; Singh, A. Oxidation of Tryptophan and N-Methylindole by N3●, Br2●-, and (SCN)2●- Radicals in Light- and Heavy-Water Solutions: A Pulse Radiolysis Study. *J. Phys. Chem.* **1991**, *95* (9), 3639–3643.

(104) Seo, D.; Soeta, T.; Sakurai, H.; Sétif, P.; Sakurai, T. Pre-Steady-State Kinetic Studies of Redox Reactions Catalysed by Bacillus Subtilis Ferredoxin-NADP+ Oxidoreductase with NADP+/NADPH and Ferredoxin. *Biochim. Biophys. Acta* **2016**, *1857* (6), 678–687.

(105) Fabian, J. TDDFT-Calculations of Vis/NIR Absorbing Compounds. *Dye. Pigment.* **2010**, *84* (1), 36–53.

(106) He, T. F.; Guo, L.; Guo, X.; Chang, C. W.; Wang, L.; Zhong, D. Femtosecond Dynamics of Short-Range Protein Electron Transfer in Flavodoxin. *Biochemistry* **2013**, *52* (51), 9120–9128.

(107) Berndt, A.; Kottke, T.; Breitkreuz, H.; Dvorsky, R.; Hennig, S.; Alexander, M.; Wolf, E. A Novel Photoreaction Mechanism for the Circadian Blue Light Photoreceptor Drosophila Cryptochrome. *J. Biol. Chem.* **2007**, *282* (17), 13011–13021.

(108) Gauden, M.; Van Stokkum, I. H. M.; Key, J. M.; Lührs, D. C.; Van Grondelle, R.; Hegemann, P.; Kennis, J. T. M. Hydrogen-Bond Switching through a Radical Pair

Mechanism in a Flavin-Binding Photoreceptor. *Proc. Natl. Acad. Sci. U. S. A.* **2006**, *103* (29), 10895–10900.

(109) Gadda, G.; Francis, K. Nitronate Monooxygenase, a Model for Anionic Flavin Semiquinone Intermediates in Oxidative Catalysis. *Arch. Biochem. Biophys.* **2010**, *493* (1), 53–61.

(110) Porters, D. J. T.; Bright, H. J. Mechanism of Oxidation of Nitroethane by Glucose Oxidase. *J. Biol. Chem.* **1977**, *252*, 4361–4370.

(111) Bankar, S. B.; Bule, M. V.; Singhal, R. S.; Ananthanarayan, L. Glucose Oxidase - An Overview. *Biotechnol. Adv.* **2009**, *27* (4), 489–501.

(112) Medina, M.; Vrielink, A.; Cammack, R. ESR and Electron Nuclear Double Resonance Characterization of the Cholesterol Oxidase from Brevibacterium Sterolicum in Its Semiquinone State. *Eur. J. Biochem.* **1994**, *222* (3), 941–947.

(113) Wagner, M. A.; Trickey, P.; Che, Z. W.; Mathews, F. S.; Jorns, M. S. Monomeric Sarcosine Oxidase: 1. Flavin Reactivity and Active Site Binding Determinants. *Biochemistry* **2000**, *39* (30), 8813–8824.

(114) Ghanem, M.; Gadda, G. Effects of Reversing the Protein Positive Charge in the Proximity of the Flavin N(1) Locus of Choline Oxidase. *Biochemistry* **2006**, *45* (10), 3437–3447.

(115) Muh, U.; Massey, V.; Williams, C. H. Lactate Monooxygenase. I. Expression of the Mycobacterial Gene in Escherichia Coli and Site-Directed Mutagenesis of Lysine 266. *J. Biol. Chem.* **1994**, *269* (11), 7982–7988.

(116) Land, E. J.; Swallow, A. J. One-Electron Reactions in Biochemical Systems as Studied by Pulse Radiolysis. II. Riboflavin. *Biochemistry* **1969**, *8* (5), 2117–2125.

(117) Massey, V.; Stankovich, M.; Hemmerich, P. Light-Mediated Reduction of Flavoproteins with Flavins as Catalysts. *Biochemistry* **1978**, *17* (1), 1–8.

(118) Orville, A. M.; Lountos, G. T.; Finnegan, S.; Gadda, G.; Prabhakar, R. Crystallographic, Spectroscopic, and Computational Analysis of a Flavin C4a−Oxygen Adduct in Choline Oxidase. *Biochemistry* **2009**, *48* (4), 720–728.

(119) Hamdane, D.; Guérineau, V.; Un, S.; Golinelli-Pimpaneau, B. A Catalytic Intermediate and Several Flavin Redox States Stabilized by Folate-Dependent TRNA Methyltransferase from Bacillus Subtilis. *Biochemistry* **2011**, *50* (23), 5208–5219.

(120) Sournia, P. La Méthylation Flavine-Dépendante d'acides Nucléiques : Aspects Évolutifs, Métaboliques, Biochimiques et Spectroscopiques, PhD Thesis, Ecole Polytechnique, Palaiseau, France, 2016.

(121) Zimmer, K.; Gödicke, B.; Hoppmeier, M.; Meyer, H.; Schweig, A. Fluorescence Spectroscopic Studies on the Radical Cations of Tetrathiafulvalenes. *Chem. Phys.* **1999**, *248* (2–3), 263–271.

(122) Meisel, D.; Das, P. K.; Hug, G. L.; Bhattacharyya, K.; Fessenden, R. W. Temperature Dependence of the Lifetime of Excited Benzyl and Other Arylmethyl Radicals. *J. Am. Chem. Soc.* **1986**, *108* (16), 4706–4710.

(123) Goswami, S.; Nelson, J. N.; Islamoglu, T.; Wu, Y. L.; Farha, O. K.; Wasielewski, M.

R. Photoexcited Naphthalene Diimide Radical Anion Linking the Nodes of a Metal-Organic Framework: A Heterogeneous Super-Reductant. *Chem. Mater.* **2018**, *30* (8), 2488–2492.

(124) Christensen, J. A.; T. Phelan, B.; Chaudhuri, S.; Acharya, A.; S. Batista, V.; R. Wasielewski, M. Phenothiazine Radical Cation Excited States as Super-Oxidants for Energy-Demanding Reactions. *J. Am. Chem. Soc.* **2018**, *140* (15), 5290–5299.

(125) Parson, W. W. *Modern Optical Spectroscopy: With Exercises and Examples from Biophysics and Biochemistry, Second Edition*; Springer Berlin Heidelberg, 2015.

(126) Hare, P. M.; Price, E. A.; Bartels, D. M. Hydrated Electron Extinction Coefficient Revisited. *J. Phys. Chem. A* **2008**, *112* (30), 6800–6802.

(127) Tsuneda, T.; Song, J. W.; Suzuki, S.; Hirao, K. On Koopmans' Theorem in Density Functional Theory. *J. Chem. Phys.* **2010**, *133* (17), 174101.

(128) Chang-Guo, Z.; Nichols, J. A.; Dixon, D. A. Ionization Potential, Electron Affinity, Electronegativity, Hardness, and Electron Excitation Energy: Molecular Properties from Density Functional Theory Orbital Energies. *J. Phys. Chem. A* **2003**, *107* (20), 4184–4195.

(129) Stowasser, R.; Hoffmann, R. What Do the Kohn-Sham Orbitals and Eigenvalues Mean? *J. Am. Chem. Soc.* **1999**, *121* (14), 3414–3420.

(130) Rao, P. S.; Simio, M.; Hayon, E.; Slmic, M. Pulse Radiolysis Study of Imidazole and Histidine in Water. *J. Phys. Chem.* **1975**, *79* (13), 1260–1263.

(131) Changtong, H.; Seymour, J. L.; Tureček, F. Electron Super-Rich Radicals in the Gas Phase. A Neutralization- Reionization Mass Spectrometric and Ab Initio/RRKM Study of Diaminohydroxymethyl and Triaminomethyl Radicals. *J. Phys. Chem. A* **2007**, *111* (36), 8829–8843.

(132) Parson, W. W. Competition between Tryptophan Fluorescence and Electron Transfer during Unfolding of the Villin Headpiece. *Biochemistry* **2014**, *53* (28), 4503–4509.

(133) Quaye, O.; Cowins, S.; Gadda, G. Contribution of Flavin Covalent Linkage with Histidine 99 to the Reaction Catalyzed by Choline Oxidase. *J. Biol. Chem.* **2009**, *284* (25), 16990–16997.

(134) Williamson, G.; Edmondson, D. E. Effect of PH on Oxidation-Reduction Potentials of 8.Alpha.-N-Imidazole-Substituted Flavins. *Biochemistry* **2002**, *24* (26), 7790–7797.

(135) Mohamed-Raseek, N.; Miller, A.-F. Contrasting Roles for Two Conserved Arginines: Stabilizing Flavin Semiquinone or Quaternary Structure, in Bifurcating Electron Transfer Flavoproteins. *J. Biol. Chem.* **2022**, *298* (4), 101733.

(136) Gadda, G. Oxygen Activation in Flavoprotein Oxidases: The Importance of Being Positive. *Biochemistry* **2012**, *51* (13), 2662–2669.

(137) Wohlfahrt, G.; Witt, S.; Hendle, J.; Schomburg, D.; Kalisz, H. M.; Hecht, H. J. 1.8 and 1.9 Å Resolution Structures of the -Penicillium Amagasakiense and Aspergillus Niger Glucose Oxidases as a Basis for Modelling Substrate Complexes. *Acta Crystallogr. Sect. D Biol. Crystallogr.* **1999**, *55* (5), 969–977.

(138) Roth, J. P.; Klinman, J. P. Catalysis of Electron Transfer during Activation of O 2 by

the Flavoprotein Glucose Oxidase. *Proc. Natl. Acad. Sci. USA* **2003**, *100* (1), 62–67.

(139) Sanners, C.; Macheroux, P.; Ruterjans, H.; Müller, F.; Bacher, A. 15N- and 13C-NMR Investigations of Glucose Oxidase from Aspergillus Niger. *Eur. J. Biochem.* **1991**, *196* (3), 663–672.

(140) Dušan, P.; Frank, D.; Caroline, S.; Kamerlin, L.; Hoffmann, K.; Strodel, B. Shuffling Active Site Substate Populations Affects Catalytic Activity: The Case of Glucose Oxidase. *ACS Catal.* **2017**, *7* (9), 6188−6197.

(141) Faraggi, M.; Tal, Y. The Reaction of the Hydrated Electron with Amino Acids, Peptides, and Proteins in Aqueous Solution. II. Formation of Radicals and Electron Transfer Reactions. *Radiat. Res.* **1975**, *62* (2), 347–356.

(142) Namazian, M.; Coote, M. L. Accurate Calculation of Absolute One-Electron Redox Potentials of Some Para-Quinone Derivatives in Acetonitrile. *J. Phys. Chem. A* **2007**, *111* (30), 7227–7232.

(143) Neugebauer, H.; Bohle, F.; Bursch, M.; Hansen, A.; Grimme, S. Benchmark Study of Electrochemical Redox Potentials Calculated with Semiempirical and DFT Methods. *J. Phys. Chem. A* **2020**, *124* (35), 7166–7176.

(144) Rabenstein, B.; Matthias Ullmann, G.; Knapp, E.-W. Energetics of Electron-Transfer and Protonation Reactions of the Quinones in the Photosynthetic Reaction Center of Rhodopseudomonas Viridis. *Biochemistry* **1998**, *37* (8), 2488–2495.

(145) Sen, T.; Ma, Y.; Polyakov, I. V.; Grigorenko, B. L.; Nemukhin, A. V.; Krylov, A. I. Interplay between Locally Excited and Charge Transfer States Governs the Photoswitching Mechanism in the Fluorescent Protein Dreiklang. *J. Phys. Chem. B* **2021**, *125* (3), 757–770.

(146) Ghanem, M.; Gadda, G. On the Catalytic Role of the Conserved Active Site Residue His 466 of Choline Oxidase. *Biochemistry* **2005**, *44* (3), 893–904.

(147) Hassan-Abdallah, A.; Zhao, G.; Chen, Z.; Mathews, F. S.; Jorns, M. S. Arginine 49 Is a Bifunctional Residue Important in Catalysis and Biosynthesis of Monomeric Sarcosine Oxidase: A Context-Sensitive Model for the Electrostatic Impact of Arginine to Lysine Mutations. *Biochemistry* **2008**, *47* (9), 2913–2922.

(148) Aliverti, A.; Pandini, V.; Pennati, A.; de Rosa, M.; Zanetti, G. Structural and Functional Diversity of Ferredoxin-NADP+ Reductases. *Arch. Biochem. Biophys.* **2008**, *474* (2), 283–291.

(149) Muraki, N.; Seo, D.; Shiba, T.; Sakurai, T.; Kurisu, G. Asymmetric Dimeric Structure of Ferredoxin-NAD(P)+ Oxidoreductase from the Green Sulfur Bacterium Chlorobaculum Tepidum: Implications for Binding Ferredoxin and NADP+. *J. Mol. Biol.* **2010**, *401* (3), 403–414.

(150) Seo, D.; Sakurai, H. Purification and Characterization of Ferredoxin-NAD(P)(+) Reductase from the Green Sulfur Bacterium Chlorobium Tepidum. *Biochim. Biophys. Acta* **2002**, *1597* (1), 123–132.

(151) Senda, M.; Kishigami, S.; Kimura, S.; Fukuda, M.; Ishida, T.; Senda, T. Molecular Mechanism of the Redox-Dependent Interaction between NADH-Dependent Ferredoxin Reductase and Rieske-Type [2Fe-2S] Ferredoxin. *J. Mol. Biol.* **2007**, *373* (2), 382–400.

(152) Senda, T.; Senda, M.; Kimura, S.; Ishida, T. Redox Control of Protein Conformation in Flavoproteins. *Antioxid. Redox Signal.* **2009**, *11* (7), 1741–1766.

(153) Tejero, J.; Peregrina, J. R.; Martínez-Júlvez, M.; Gutiérrez, A.; Gómez-Moreno, C.; Scrutton, N. S.; Medina, M. Catalytic Mechanism of Hydride Transfer between NADP+/H and Ferredoxin-NADP+ Reductase from Anabaena PCC 7119. *Arch. Biochem. Biophys.* **2007**, *459* (1), 79–90.

(154) Bruns, C. M.; Karplus, A. P. Refined Crystal Structure of Spinach Ferredoxin Reductase at 1.7 Å Resolution: Oxidized, Reduced and 2′-Phospho-5′-AMP Bound States. *J. Mol. Biol.* **1995**, *247* (1), 125–145.

(155) Lennon, B. W.; Williams, C. H.; Ludwig, M. L. Crystal Structure of Reduced Thioredoxin Reductase from Escherichia Coli: Structural Flexibility in the Isoalloxazine Ring of the Flavin Adenine Dinucleotide Cofactor. *Protein Sci.* **1999**, *8* (11), 2366–2379.

(156) Corrado, M. E.; Aliverti, A.; Zanetti, G.; Mayhew, S. G. Analysis of the Oxidation-Reduction Potentials of Recombinant Ferredoxin-NADP+ Reductase from Spinach Chloroplasts. *Eur. J. Biochem.* **1996**, *239* (3), 662–667.

(157) Dozova, N.; Lacombat, F.; Lombard, M.; Hamdane, D.; Plaza, P. Ultrafast Dynamics of Fully Reduced Flavin in Catalytic Structures of Thymidylate Synthase ThyX. *Phys. Chem. Chem. Phys.* **2021**, *23* (39), 22692–22702.

(158) Brazard, J. Photoactivation Femtoseconde de Deux Nouvelles Protéines de La Famille Des Cryptochrome/Photolyase, Issues de l'algue Verte Ostreococcus Tauri. Photocycle Ultrarapide et État Signalant de La Photophobie Du Protozoaire Blepharisma Japonicum, PhD Thesis, Université Pierre-et-Marie-Curie, Paris, France, 2009.

(159) Jimenez, R.; Fleming, G. R.; Kumar, P. V.; Maroncelli, M. Femtosecond Solvation Dynamics of Water. *Nat. 1994 3696480* **1994**, *369* (6480), 471–473.

(160) Seo, D.; Asano, T. C-Terminal Residues of Ferredoxin-NAD(P)+ Reductase from Chlorobaculum Tepidum Are Responsible for Reaction Dynamics in the Hydride Transfer and Redox Equilibria with NADP+/NADPH. *Photosynth. Res. 2017 1363* **2017**, *136* (3), 275–290.

(161) Prongay, A. J.; Williams, C. H. Oxidation-Reduction Properties of Escherichia Coli Thioredoxin Reductase Altered at Each Active Site Cysteine Residue. *J. Biol. Chem.* **1992**, *267* (35), 25181–25188.

(162) Schwinn, K.; Ferré, N.; Huix-Rotllant, M. UV-Visible Absorption Spectrum of FAD and Its Reduced Forms Embedded in a Cryptochrome Protein. *Phys. Chem. Chem. Phys* **2020**, *22*, 12447.

(163) Massey, V.; Ghisla, S. Role of Charge-Transfer Interactions in Flavoprotein Catalysis. *Ann. N. Y. Acad. Sci.* **1974**, *227* (1), 446–465.

(164) Hopkins, N.; Stanley, R. J. Measurement of the Electronic Properties of the Flavoprotein Old Yellow Enzyme (OYE) and the OYE:P-Cl Phenol Charge-Transfer Complex Using Stark Spectroscopy. *Biochemistry* **2003**, *42* (4), 991–999.

(165) Stewart, R. C.; Massey, V. Potentiometric Studies of Native and Flavin-Substituted Old Yellow Enzyme. *J. Biol. Chem.* **1985**, *260* (25), 13639–13647.

(166) Nishina, Y.; Shiga, K.; Miura, R.; Tojo, H.; Ohta, M.; Miyake, Y.; Yamano, T.; Watari, H. On the Structures of Flavoprotein D-Amino Acid Oxidase Purple Intermediates. A Resonance Raman Study. *J. Biochem.* **1983**, *94* (6), 1979–1990.

(167) Sevrioukova, I.; Shaffer, C.; Ballou, D. P.; Peterson, J. A. Equilibrium and Transient State Spectrophotometric Studies of the Mechanism of Reduction of the Flavoprotein Domain of P450BM-3. *Biochemistry* **1996**, *35* (22), 7058–7068.

(168) Taniguchi, S.; Chosrowjan, H.; Tamaoki, H.; Nishina, Y.; Nueangaudom, A.; Tanaka, F. Ultrafast Photoinduced Electron Transfer in O-Aminobenzoate – d-Amino Acid Oxidase Complex. *J. Photochem. Photobiol. A Chem.* **2021**, *420*, 113448.

(169) Alford, S. C.; Wu, J.; Zhao, Y.; Campbell, R. E.; Knöpfel, T. Optogenetic Reporters. *Biol. Cell* **2013**, *105* (1), 14–29.

(170) Tang, K.; Beyer, H. M.; Zurbriggen, M. D.; Gärtner, W. The Red Edge: Bilin-Binding Photoreceptors as Optogenetic Tools and Fluorescence Reporters. *Chem. Rev.* **2021**, *121* (24), 14906–14956.

(171) Trickey, P.; Wagner, M. A.; Jorns, M. S.; Mathews, F. S. Monomeric Sarcosine Oxidase: Structure of a Covalently Flavinylated Amine Oxidizing Enzyme. *Structure* **1999**, *7* (3), 331–345.

(172) Wagner, M. A.; Jorns, M. S. Monomeric Sarcosine Oxidase: 2. Kinetic Studies with Sarcosine, Alternate Substrates, and a Substrate Analogue. *Biochemistry* **2000**, *39* (30), 8825–8829.

(173) Zhao, G.; Jorns, M. S. Spectral and Kinetic Characterization of the Michaelis Charge Transfer Complex in Monomeric Sarcosine Oxidase. *Biochemistry* **2006**, *45* (19), 5985–5992.

(174) Motherwell, W. B.; Moreno, R. B.; Pavlakos, I.; Osephine, J.; Arendorf, R. T.; Arif, T.; Tizzard, G. J.; Coles, S. J.; Aliev, A. E. Noncovalent Interactions of π Systems with Sulfur: The Atomic Chameleon of Molecular Recognition. *Angew. Chemie* **2018**, *130* (5), 1207–1212.

(175) Hwang, J.; Li, P.; Smith, M. D.; Warden, C. E.; Sirianni, D. A.; Vik, E. C.; Maier, J. M.; Yehl, C. J.; Sherrill, C. D.; Shimizu, K. D. Tipping the Balance between S-π and O-π Interactions. *J. Am. Chem. Soc.* **2018**, *140* (41), 13301–13307.

(176) Zheng, Y.; Wagner, M. A.; Jorns, M. S.; Carey, P. R. Selective Enhancement of Ligand and Flavin Raman Modes in Charge-Transfer Complexes of Sarcosine Oxidase. *J. Raman Spectrosc.* **2001**, *32* (2), 79–92.

(177) Borshchevskiy, V. I.; Round, E. S.; Popov, A. N.; Büldt, G.; Gordeliy, V. I. X-Ray-Radiation-Induced Changes in Bacteriorhodopsin Structure. *J. Mol. Biol.* **2011**, *409* (5), 813–825.

(178) Tkachenko, N. V.; Lemmetyinen, H.; Sonoda, J.; Ohkubo, K.; Sato, T.; Imahori, H.; Fukuzumi, S. Ultrafast Photodynamics of Exciplex Formation and Photoinduced Electron Transfer in Porphyrin-Fullerene Dyads Linked at Close Proximity. *J. Phys. Chem. A* **2003**, *107* (42), 8834–8844.

(179) Mori, T.; Inoue, Y. Charge-Transfer Excitation: Unconventional yet Practical Means for Controlling Stereoselectivity in Asymmetric Photoreactions. *Chem. Soc. Rev.* **2013**, *42* (20), 8122–8133.

(180) Oldemeyer, S.; Franz, S.; Wenzel, S.; Essen, L. O.; Mittag, M.; Kottke, T. Essential Role of an Unusually Long-Lived Tyrosyl Radical in the Response to Red Light of the Animal-like Cryptochrome Acry. *J. Biol. Chem.* **2016**, *291* (27), 14062–14071.

List of Publications

1. Zhuang, B.; Seo, D.; Aleksandrov, A.; Vos, M. Characterization of Light-Induced, Short-Lived Interacting Radicals in the Active Site of Flavoprotein Ferredoxin-NADP+ Oxidoreductase. *J. Am. Chem. Soc.* **2021**, *143* (7), 2757–2768

2. Sorigué, D.; Hadjidemetriou, K.; Blangy, S.; Gotthard, G.; Bonvalet, A.; Coquelle, N.; Samire, P.; Aleksandrov, A.; Antonucci, L.; Benachir, A.; Boutet, S.; Byrdin, M.; Cammarata, M.; Carbajo, S.; Cuiné, S.; Doak, R. B.; Foucar, L.; Gorel, A.; Grünbein, M.; Hartmann, E.; Hienerwadel, R.; Hilpert, M.; Kloos, M.; Lane, T. J.; Légeret, B.; Legrand, P.; Li-Beisson, Y.; Moulin, S. L. Y.; Nurizzo, D.; Peltier, G.; Schirò, G.; Shoeman, R. L.; Sliwa, M.; Solinas, X.; Zhuang, B.; Barends, T. R. M.; Colletier, J.-P.; Joffre, M.; Royant, A.; Berthomieu, C.; Weik, M.; Domratcheva, T.; Brettel, K.; Vos, M. H.; Schlichting, I.; Arnoux, P.; Müller, P.; Beisson, F. Mechanism and Dynamics of Fatty Acid Photodecarboxylase. *Science* **2021**, *372* (6538), eabd5687

3. Zhuang, B.; Nag, L.; Sournia, P.; Croitoru, A.; Ramodiharilafy, R.; Lambry, J.-C.; Myllykallio, H.; Aleksandrov, A.; Liebl, U.; Vos, M. H. Photochemical processes in flavo-enzymes as a probe for active site dynamics: TrmFO of *Thermus thermophilus*. *Photochem. Photobiol. Sci.* **2021**, *20*, 663–670

4. Zhuang, B.; Ramodiharilafy, R.; Liebl, U.; Aleksandrov, A.; Vos, M. H. Ultrafast Photooxidation of Protein-Bound Anionic Flavin Radicals. *Proc. Natl. Acad. Sci. U. S. A.* **2022**, *119* (8), e2118924119

5. Zhuang, B.; Liebl, U.; Vos, M. H. Flavoprotein Photochemistry: Fundamental Processes and Photocatalytic Perspectives. *J. Phys. Chem. B* **2022**, *126* (17), 3199–3207

6. Zhuang, B.; Vos, M. H. Photoswitching Behavior of Flavin–Inhibitor Complex in a Nonphotocatalytic Flavoenzyme. *J. Am. Chem. Soc*. **2022**, *144* (26), 11569–11573

ECOLE DOCTORALE

Titre : Processus Fondamentaux de la Photochimie des Flavoprotéines

Mots clés : flavoprotéines, photochimie, spectroscopie optique résolue en temps, simulation numérique

Résumé : Dans cette thèse, par l'application de spectroscopie ultrarapide combinée avec des simulations moléculaires et d'approches de chimie quantique, plusieurs processus photochimiques fondamentaux dans les flavoprotéines est étudiée. D'abord, la photoréduction des flavines oxydées a été revisitée dans la ferrédoxine-$NADP^+$ oxydoréductase (FNR), dont la configuration permet la formation ultrarapide de paires de radicaux intermédiaires. L'influence de l'environnement sur les propriétés spectrales des radicaux anioniques de flavine et cationiques de tyrosine ou tryptophane a été évaluée en détail. Ensuite, il est démontré que la photooxydation des radicaux anioniques de flavine, qui agissent comme des intermédiaires de réaction dans de nombreuses réactions biochimiques, se produit efficacement en ~100 fs dans les flavoprotéines oxydases. Ce processus, qui est effectivement l'inverse de la photoréduction bien connue de la flavine oxydée, pourrait constituer une voie de désactivation universelle. Les propriétés de l'état excité des flavines complétement réduites ont été étudiées dans plusieurs systèmes FNR où elles sont impliquées comme intermédiaires fonctionnels, et en solution. Des informations précieuses concernant leurs structures électroniques et la flexibilité des flavines ont été obtenues, avec des implications catalytiques importantes. Enfin, un phénomène de photo-dissociation sans précédent a été révélé pour un complexe de transfert de charge non covalent de la flavine et d'un inhibiteur dans la flavoenzyme sarcosine oxydase monomérique. Ce processus se produit dans quelques centaines de femtosecondes et peut être attribué à une isomérisation photoinduite de l'inhibiteur. A terme ces travaux peuvent mener à des implications pratiques comme des nouveaux photocatalyseurs et des outils optogénétiques.

Title : Fundamental Processes in Flavoprotein Photochemistry

Keywords : flavoproteins, photochemistry, time-resolved optical spectroscopy, computer simulation

Abstract : In this thesis, applying ultrafast spectroscopy combined with molecular simulations and quantum chemistry approaches, several fundamental photochemical processes in flavoproteins are investigated. First the photoreduction of oxidized flavins was revisited in ferredoxin-$NADP^+$ oxidoreductase (FNR), which configuration allows ultrafast formation of intermediate radical pairs. The influence of the environment on the spectral properties of both the anionic flavin and the cationic tyrosine or tryptophan radicals was assessed in detail. Further it is demonstrated that photooxidation of anionic flavin radicals, which act as reaction intermediates in many biochemical reactions, efficiently occurs within ~100 fs in flavoprotein oxidases. This process, effectively the reverse of the well-known photoreduction of oxidized flavin may constitute a universal decay pathway. The excited-state properties of fully reduced flavins were studied in several FNR systems where they are involved as functional intermediates, and in solution. Valuable information concerning their electronic structures and the flavin flexibility was obtained, with important catalytic implications. Finally, an unprecedented photo-dissociation phenomenon was revealed for a non-covalent charge transfer complex of flavin and an inhibitor in the flavoenzyme monomeric sarcosine oxidase. This process occurs in a few hundred femtoseconds and can be attributed to a photoinduced isomerization of the inhibitor. These studies may ultimately lead to practical implications as novel photocatalysts and optogenetic tools.